

Cellular and Synaptic Mechanisms that Underlie Eupnea and Sigh Rhythms
for Breathing Behavior in Mice

Daniel Scott Borrus

Branford, Connecticut

Bachelor of Science, College of William & Mary, 2017

A Dissertation presented to the Graduate Faculty
of The College of William & Mary in Candidacy for the Degree of
Doctor of Philosophy

Department of Applied Science

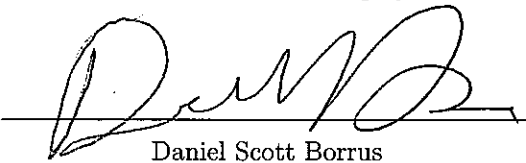
College of William & Mary
January 2022

©2022
Daniel Scott Borrus
All rights reserved.

APPROVAL PAGE

This Dissertation is submitted in partial fulfillment of
the requirements for the degree of

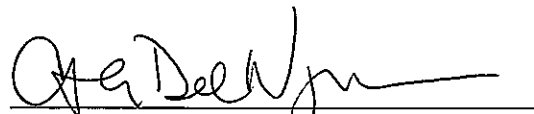
Doctor of Philosophy



A handwritten signature in black ink, appearing to read "Dan Scott Borrus".

Daniel Scott Borrus

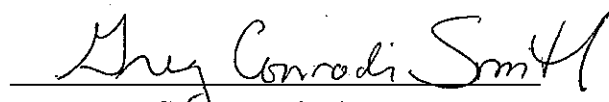
Approved by the Committee, November, 2021



A handwritten signature in black ink, appearing to read "Christopher A. Del Negro".

Committee Co-Chair

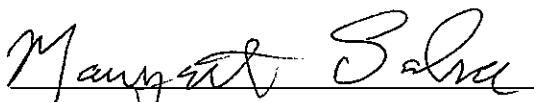
Christopher A. Del Negro, Professor, Applied Science
College of William & Mary



A handwritten signature in black ink, appearing to read "Gregory D. Conradi Smith".

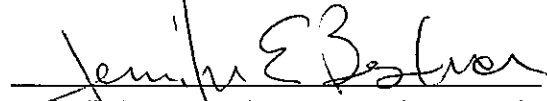
Committee Co-Chair

Gregory D. Conradi Smith, Professor, Applied Science
College of William & Mary



A handwritten signature in black ink, appearing to read "Margaret S. Saha".

Margaret S. Saha, Chancellor Professor, Biology
College of William & Mary



A handwritten signature in black ink, appearing to read "Jennifer E. Bestman".

Jennifer E. Bestman, Assistant Professor, Biology
College of William & Mary

ABSTRACT

Breathing is a lifelong activity that involves the coordination of several rhythmic behaviors. This dissertation investigates the neural origins of two of these breathing rhythms: eupnea and sighing. Eupnea, or regular unlaborated breathing, occurs on the order of seconds and serves to drive the exchange of oxygen and carbon dioxide between the circulatory system and the environment. Sighs, deep breaths that are typically 2-5 times the volume of a eupneic breath, occur on the order of minutes and are critical in maintaining pulmonary function. Understanding how these rhythms are generated on a cellular and synaptic level is an essential step in preventing numerous pathologies, such as sudden infant death syndrome, and respiratory depression and failure as a consequence of opioids in a clinical setting or as drugs of abuse. First, we uncover the cellular and synaptic mechanisms that couple these two rhythms using electrophysiology and an *in vitro* breathing model from neonatal mice. Next, using mathematical modeling techniques, we explore how interconnectivity of the neural circuitry may drive the eupnea rhythm. Finally, we layout and test a novel framework for how intracellular calcium oscillations drive the sigh rhythm using a combination of electrophysiology and an *in vitro* breathing model combined with mathematical modeling. Unraveling the mechanisms that generate the eupnea and sigh rhythms reveals deeper insights into rhythms throughout the brain.

TABLE OF CONTENTS

Acknowledgments	iv
Dedication	v
Chapter	
1 Introduction	1
1.1 Rhythmic breathing: eupneic and sigh breaths	3
1.2 Rhythmic neural bursts: inspiratory and sigh events	5
1.3 Cellular composition of the preBötzinger complex	8
1.4 The pacemaker hypothesis for inspiratory rhythmogenesis	9
1.5 The recurrent excitation hypothesis for inspiratory rhythmogenesis	14
1.6 History of sigh rhythmogenesis	18
2 Role of synaptic inhibition in the coupling of the respiratory rhythms that underlie eupnea and sigh behaviors	23
2.1 Introduction	23
2.2 Results	26
2.2.1 Sigh breaths follow eupneic breaths with variable time intervals .	26
2.2.2 Sigh bursts follow inspiratory bursts with variable time intervals .	28
2.2.3 Inhibitory synapses do not link sigh bursts to the inspiratory rhythm	30
2.2.4 Inhibitory synapses do not influence post-sigh apnea	32
2.2.5 Chloride-mediated synaptic transmission is inhibitory in the neonatal mouse preBtC	33
2.3 Discussion	37
2.4 Appendix: Materials and Methods	43

3	The preinspiratory phase of eupnea rhythmogenesis requires more than recurrent excitation	51
3.1	Introduction	51
3.2	Activity models of episodic bursting	54
3.2.1	Dynamics of synaptic depression	56
3.2.2	Inspiratory dynamics with two variables (one fast and one slow) .	58
3.2.3	Inspiratory dynamics with three variables (one fast and two slow)	61
3.2.4	Takeaways from the activity-based model for inspiratory rhythmo- genesis	63
3.3	Studying recurrent excitation in a network of coupled oscillators	65
3.3.1	The network-based model can be configured for type-1 and type-2 excitability	70
3.3.2	The network-based model oscillates with various topologies	72
3.3.3	Different topologies lead to differences in rhythm pattern	78
3.3.4	Different topologies lead to differences in rhythm breakdown . . .	81
3.4	Percolation is sensitive to network topology	84
3.5	Discussion	89
3.6	Appendix: Modeling noise in the activity models	91
4	The preBtzinger complex generates sigh rhythm via intracellular calcium oscilla- tions in mice	94
4.1	Introduction	94
4.2	Results	98
4.2.1	I_h does not contribute to sigh rhythmogenesis	98
4.2.2	The sigh rhythm is more voltage-independent than the inspiratory rhythm	100
4.2.3	Glia-mediated purinergic signaling is not necessary for sigh rhythm generation	102

4.2.4	The sigh and inspiratory rhythms arise from the same population of neurons	105
4.2.5	Intracellular Ca^{2+} oscillations can lead to sigh bursts	106
4.2.6	Disrupting SERCA activity impacts sigh frequency	110
4.2.7	Blocking IP3R diminishes sigh rhythm frequency	116
4.3	Discussion	118
4.3.1	A Ca^{2+} based oscillator for sighs suggests excitatory synapses cou- ple the inspiratory and sigh rhythms	118
4.3.2	Alternative biochemical sources for sigh rhythmogenesis	120
4.3.3	Alternative paths for glia-driven sigh events	120
4.4	Appendix: Materials and Methods	121
4.5	Appendix: Modeling of sigh rhythm and the coupling to eupnea	124
5	Conclusion and Discussion	134
	References	141
	Vita	160

ACKNOWLEDGMENTS

This work would not have been possible but for the network of colleagues and friends at The College of William & Mary, and in the Department of Applied Science in particular. Both my advisors, Christopher A. Del Negro and Gregory D. Conradi Smith, provided me with endless support and motivation throughout my graduate (and undergraduate) studies. My labmates, Prajukta Kallurkar and Cameron Grover, taught me endlessly, especially in electrophysiology. Everyone in the Computational Biology Lab, with a special shout out to Ronald Smith, who was my first teacher in computer science and kicked off a lifelong love of the field. And finally my friends, Sean Chadwick and Cameron Backes, whose burning love for knowledge and discovery sparked countless late-night debates on every conceivable topic, and who inspired me to pursue a Ph.D.

You have all made me the scientist that I am today. Thank you.

Dedicated to my mother, Joanne, and my brother, Marshall.

“The most important thing is to try and inspire people
so that they can be great in whatever they want to do.”

- Kobe Bryant

Chapter 1

Introduction

The brain is a rhythm machine (Buzsaki, 2006). Brain rhythms influence nearly every behavior; they are involved in motor activities such as breathing (Del Negro et al., 2018), chewing (Westberg and Kolta, 2011), and locomotion (Grillner and El Manira, 2020; Kiehn, 2016), to cognitive tasks such as attention (Fiebelkorn et al., 2018; Helfrich et al., 2018) and memory (Latchoumane et al., 2017).

Breathing presents an interesting rhythmic system to study for several reasons. First, breathing is a vital behavior that must be maintained from the moment we are born to the moment of our death. The circuits involved in breathing cannot lapse for a few minutes without severe physiological consequences. There are a dozen or more pathologies that arise from issues related to breathing circuits that demand our attention, from sudden infant death syndrome (Garcia et al., 2013; Kinney et al., 2009) to respiratory depression and failure as a result of an opioid overdose (Palkovic et al., 2020; Pattinson, 2008; Rudd et al., 2016; Scholl et al., 2019). Understanding the cellular and synaptic mechanisms that drive breathing is a critical first step towards solving these problems.

The other reason breathing presents an important system to study from the standpoint of neuroscience is that the neural circuits do not generate a single breathing rhythm, but rather several rhythms that must interact and work in concert. The two breathing rhythms that are the subject of this dissertation are responsible for inspiratory breaths and sigh breaths. The breathing centers of our brainstem must generate these two rhythms simultaneously, and coordinate their relative timing. Understanding how our brain simultaneously generates these two distinct rhythms may help us unravel how other brain rhythms are generated and interact with one another.

This dissertation summarizes my work on the cellular and synaptic mechanisms that drive these two breathing behaviors, eupnea and sighing. I employed a mixture of *in vivo* and *in vitro* electrophysiology, as well as mathematical modeling of the neurons and networks underlying these behaviors. Chapter 1 provides the reader with a background of respiratory neurobiology sufficient to explore my research and findings. Chapter 2 recounts my investigation of the synaptic mechanisms that couple eupnea and sighs. Chapter 3 discusses my results concerning the network mechanisms that underlie the eupnea rhythm. Chapter 4 lays out my findings concerning sigh rhythmogenesis. Chapter 5 concludes with a unifying model for how the brain generates these two breathing rhythms.

Contributions

The results in Chapter 2 are the work of this author, with project development and writing guidance from C. A. Del Negro and G. D. Conradi Smith. C. Grover lent support for experimental work. The results are published in Borrus et al. (2020).

The modeling results in Chapter 3 are the work of this author with support from G. D.

Conradi Smith. C. A. Del Negro contributed to project development.

The work in Chapter 4 is done by this author with contributions from G.D. Conradi Smith to model design and project development. C.A. Del Negro helped conceptualize and develop the project. C. Grover and P. Kallurkar contributed experimental data. A manuscript is currently being prepared for submission.

1.1 Rhythmic breathing: eupneic and sigh breaths

The term eupnea describes regular, unlabored breathing. Eupnea occurs during periods of rest, in which an animal is not stressed or exerting itself physically. We are very familiar with these breathes; they drive gas exchange between our bodies and our environment, moving CO₂ out of and O₂ into the body. In our lab, we use plethysmography to record eupnea in an awake and alert mouse (Figure 1.1). The mouse is placed in a recording chamber, and a pressure transducer records pressure differences in the recording chamber from a reference chamber. The changes in pressure capture the mouse's breathing.

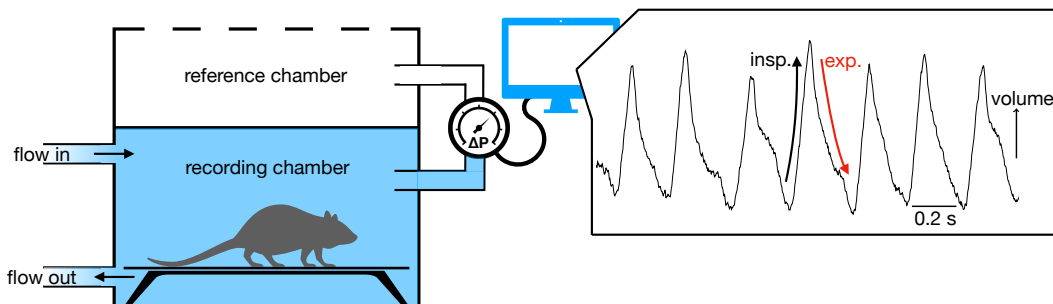


Figure 1.1: Schematic of a plethysmography chamber and recording in flow-through plethysmography mode. On the left, a representation of the plethysmography chamber with continuously refreshed room air. The gauge labeled ΔP is the pressure transducer, which measures the pressure difference (ΔP) from reference to recording chamber, which is a flow signal (volume / time) across the fixed resistance of the pressure gauge. On the right, flow is integrated to give the volume of gas inhaled (and exhaled) by the mouse, and displayed as the digital output of the mouse's breathing pattern during eupnea. The insp. label, along with the black arrow, highlight an inspiratory breath. The exp. label, and the red arrow, showcase the expiratory phase of a breath.

During regular breathing, a breath can be split into two major components: an inspiratory phase and an expiratory phase. The inspiratory phase of eupnea involves the recruitment of several muscle groups, such as the diaphragm, external intercostals, as well as genioglossus and pharyngeal abductors responsible for opening and clearing the airways. In contrast, expiration is a passive process, driven by the elastic recoil of the lungs and chest walls (or thorax) back to a steady-state volume referred to as functional residual capacity. Therefore, eupnea requires only one unconditional oscillator, which drives inspiration from birth to death. It is this kernel for inspiratory motor behavior that this dissertation explores.

Sigh breaths reinflate collapsed or collapsing alveoli in the lungs, and are essential for maintaining pulmonary function. Alveoli are the small air sacs, 200-500 μm in diameter, located at the ends of the terminal bronchioles of the branching system of airways in the lungs (Berne et al., 2008). The 300 million alveoli in the human lungs are the elementary unit for gas exchange in the respiratory system (Hasleton and Flieder, 2013). Alveoli are filled with gas, but their walls are elastic and lined with fluid. Surface tension would naturally cause these sacs to collapse, in a process known as atelectasis, if not for a surfactant distributed across the inner membrane of the alveoli. Sighs breaths regularly redistribute this surfactant, keeping it evenly spread over the alveoli, thereby preventing or reversing atelectasis. Without sighs, the lungs would lose their gas-exchange surface area, hence the ability to exchange gas with the environment (Cammarota et al., 2011; Cherniack et al., 1981; Koch et al., 2013).

We record sigh breaths using plethysmography, identical to the method for observing the eupnea rhythm earlier. Figure 1.2 highlights that fact that sigh breaths are several times larger than eupneic breaths. While the frequency of eupneic breaths is on the order of seconds, the frequency of the sigh breaths is on the order of minutes. The two rhythms are

not independent of one another; the sigh breath seems to always emerge on or immediately after a eupneic breath. Conversely, after a sigh breath, the next inspiration is delayed for a duration that lasts as long as one eupneic cycle period or more (with some variability, see Figure 1.2). These observations about event timing indicates that the rhythms are coupled, and that the mechanisms that drive them must interact in some way. My first project deals directly with this question of coupling (see Chapter 2).

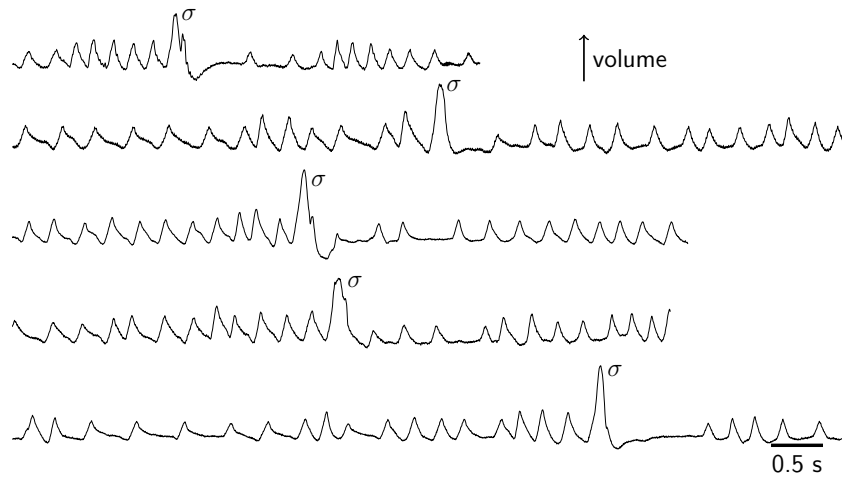


Figure 1.2: Plethysmography recording of eupnea and sigh behavior from an awake mouse. Sigh breaths are highlighted with a σ . Volume of air in the lungs is shown on the y-axis and can be calculated by integrating the flow signal in flow-through plethysmography. Inspiration takes place during positively sloped trajectories; expiration takes place during the negatively sloped trajectories.

1.2 Rhythmic neural bursts: inspiratory and sigh events

Having discussed breathing behavior, we may now approach the region of the brain from where these behaviors originate. Figure 1.3 shows a parasagittal view of a mouse brainstem with key regions identified. It has been known for over 30 years that the preBötzinger complex (preBötC), located in the ventral medulla, is the neural source for the inspiratory rhythm (Del Negro et al., 2018; Smith et al., 1991). Neurons in the preBötC project to

premotor and motor neurons that drive the synchronous recruitment of muscles required for an inspiratory breath, such as the diaphragm, external intercostals, genioglossus, and airway musculature.

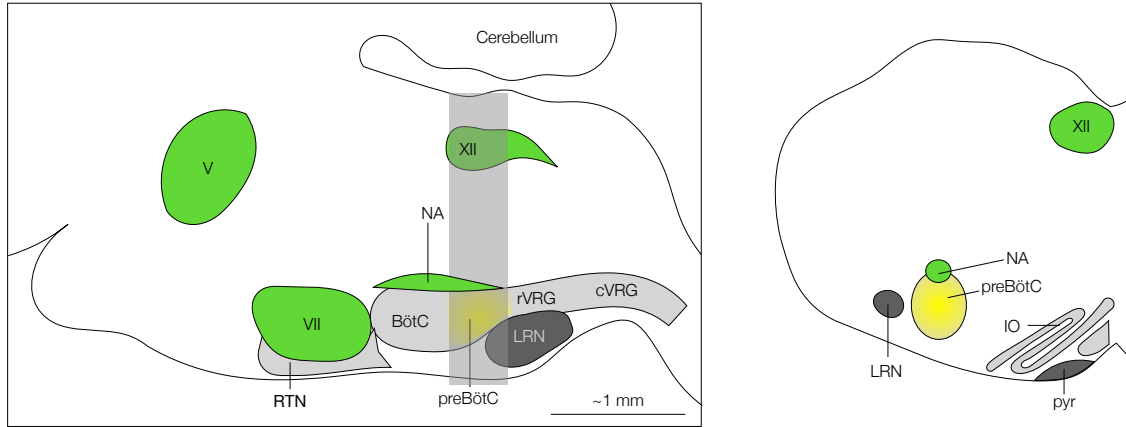


Figure 1.3: Cartoon schematic of a mouse brainstem with key regions identified. Left: Parasagittal view of a mouse brainstem. The preBötzinger complex (preBötC) is highlighted yellow. Cranial motor nuclei such as the hypoglossal motor nucleus (XII), trigeminal motor nucleus (V), facial motor nucleus (VII), and the nucleus ambiguus (NA) are shown in green. Additional regions involved in breathing circuits, the retrotrapezoidal nucleus (RTN), the Bötzinger Complex (BötC), the rostral and caudal ventral respiratory group (rVRG and cVRG) are shown in light grey. The lateral reticular nucleus (LRN) is highlighted in dark grey. A transparent vertical grey band visualizes the tissue captured in the slice preparation, shown in transverse on the right. Right: Transverse slice of a mouse brainstem. The inferior olive (IO) and pyramidal tract (pyr) are visualized here as well. Adapted from Del Negro et al. (2018).

To study the neural origin of the breathing rhythms, we take a 500 micron slice of tissue from the brainstem to isolate the preBötC. In Figure 1.3, the transparent gray rectangle highlights the dissected region. This slice preparation captures the preBötC and maintains the microcircuitry that generates the inspiratory rhythm. An electrode is placed directly on the preBötC and records the local field potential of the network; this technique is called a field recording. Figure 1.4 shows this technique in a cartoon schematic, as well as actual electrical activity obtained from a preBötC field recording. One can see rhythmic bursts of electrical activity, which are the neural precursors to inspiratory breaths. These burst events continue to emerge, in a rhythmic fashion, despite the extremely reduced biological

preparation.

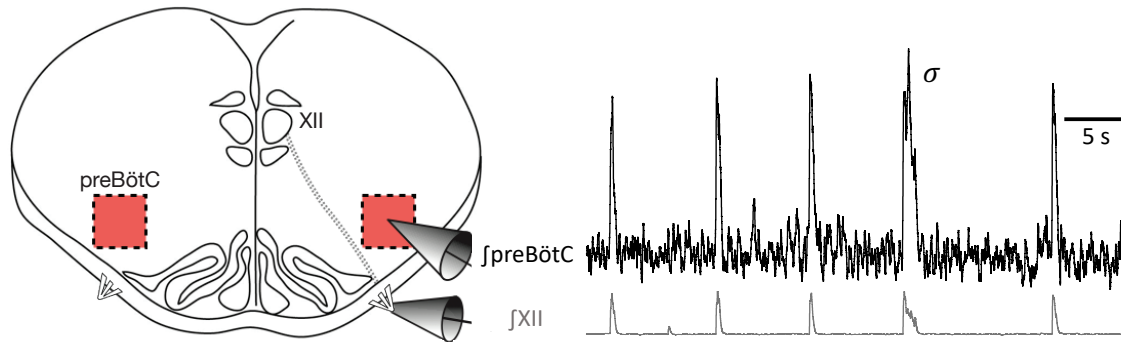


Figure 1.4: Left: Transverse view of a mouse brainstem. The region containing the preBötzing complex (preBötC) is highlighted red. The hypoglossal motor nucleus (XII), as well as the axonal projections that make up the hypoglossal nerve, is also shown. Two electrodes are recording electrical activity from the preBötC and the XII rootlets, respectively. Right: Integrated electrical activity from the two electrodes. The top trace shows a preBötC field recording. The bottom trace shows electrical output from the XII nucleus, recorded from the nerve rootlets left over from the dissection. This activity corresponds to motor output that would drive inspiratory activity in an intact animal.

The slice preparation also contains the hypoglossal motor nucleus (XII), which innervates the tongue musculature in order to keep the airway unobstructed during inspiration. A subpopulation of output-related neurons in the preBötC synapse directly onto motor neurons in the hypoglossal motor nucleus and drive motor output via the hypoglossal nerve (Smith et al., 1991). The hypoglossal nerve rootlets emerge from the side of the tissue, and provide another way to record preBötC activity, this time through the filter of a motor nucleus. Figure 1.4 shows these two signals recorded simultaneously. We refer to this technique as a root recording, because we are recording from the motor nerve rootlet. The ability to record both relayed motor output from the XII nerve, and the preBötC activity directly with a field electrode, is a unique feature of this reduced slice preparation.

Remarkably, the inspiratory rhythm is not the only behavior that manifests itself in reduced form in this *in vitro* preparation. From the field recording in Figure 1.4, we can see a burst marked with a σ that has an area several fold larger than the inspiratory events.

This large-area burst is the neural origin of a sigh breath. Both the inspiratory and sigh rhythms originate in the preBötC (Lieske et al., 2000; Ruangkittisakul et al., 2008). Similar to the behavior *in vivo*, sighs emerge on the order of minutes while the inspiratory bursts occur on the order of seconds.

The temporal relationship between inspiration and sighs observed in the *in vivo* plethysmography data remains consistent even in the much reduced *in vitro* slice preparation. The representative electrophysiology trace (Figure 1.4) makes it clear that the sigh burst appears immediately following an inspiratory burst. The inspiratory burst subsequent to the sigh event is delayed. This observation indicates that the mechanisms that couple these two rhythms remain intact in the reduced slice preparation, and are localized to these microcircuits. Chapter 2 presents my work on the synaptic and cellular mechanisms responsible for the coupling of inspiratory and sigh rhythms.

1.3 Cellular composition of the preBötzinger complex

The cellular composition of the preBötC has been an area of intense interest since it was discovered in 1990. Respiratory neurobiologists wanted to know what cellular markers could be used to 1) define the borders of the preBötC and 2) specifically perturb the important cells to investigate the mechanisms that underlie inspiration. Today, it is well established that the preBötC interneurons responsible for the inspiratory rhythm are derived from progenitor neurons that expressed embryonic transcription factor developing brain homeobox protein 1 (Dbx1) (Bouvier et al., 2010; Gray et al., 2010).

It has been shown *in vitro* that ablating 60-100 Dbx1-derived neurons in the preBötC is enough to irreversibly destroy the inspiratory rhythm (Wang et al., 2014). Furthermore,

it was shown *in vivo* that exciting, or silencing, Dbx1-derived preBötC neurons using optogenetics increases, or stops, breathing in mice, respectively (Vann et al., 2016, 2018).

We know where the inspiratory rhythm is generated and we know which neurons are responsible for the rhythm. The next question is: how do these neurons generate the inspiratory rhythm?

1.4 The pacemaker hypothesis for inspiratory rhythogenesis

A common concept in the field of motor control is the central pattern generator (CPG). A CPG is defined as a group of neurons that generate a rhythmic output in the absence of sensory feedback. Notable examples of CPGs in the mammalian brain are those that drive behaviors such as chewing, walking, whisking, and breathing (Guertin, 2009; Steuer and Guertin, 2018). Understanding the cellular and network mechanisms that drive a CPG has been an active area in neuroscience for over 60 years (Grillner and El Manira, 2020; Mulloney, 2010).

Neuroscientists today know several canonical, well studied mechanisms that drive CPGs throughout the brain. One of these well known CPG engines is the pacemaker neuron, i.e., a neuron that is intrinsically rhythmic (external input is not required). A pacemaker neuron, without input from presynaptic neighbors, will periodically fire bursts of action potentials followed by a periods of quiescence (Figure 1.5). In a pacemaker-driven CPG, these neurons engender a network of neurons to fire in concert (Grillner and El Manira, 2020).

If pacemaker neurons drive network rhythms, then the rhythmogenic nature of the

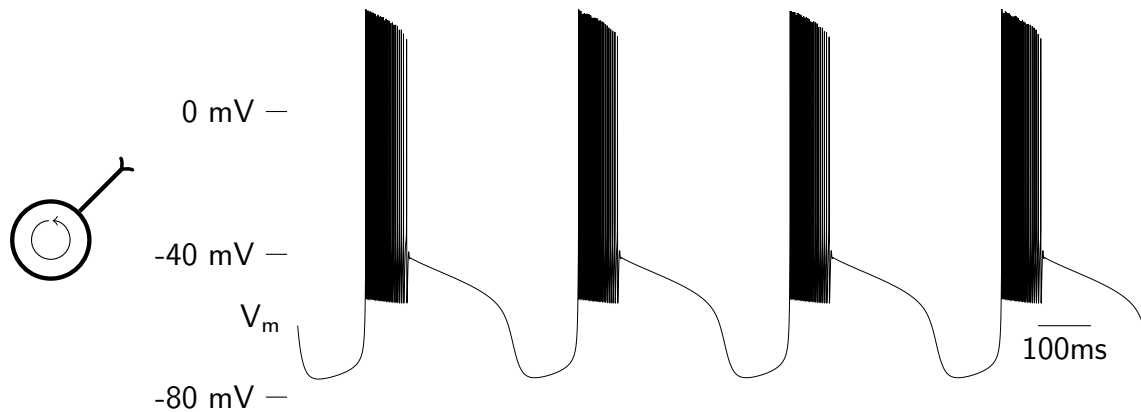


Figure 1.5: Simulation of a neuron with subthreshold currents that drive an intrinsic rhythm¹. Note that the neuron does not receive input, but can still generate a regular burst of action potentials. Model and parameters adapted from Rush and Rinzel (1994).

network lies within the biophysics of these neurons. There are several internal mechanisms that can lead to intrinsic bursting in a neuron. Most of them involve one or several sub-threshold voltage-dependent currents. These currents are “slow”, that is, they operate on a time scale an order of magnitude slower than the fast currents that generate the action potential.

An example of a sub-threshold current involved in pacemaker behavior is the persistent sodium current (I_{NaP}). I_{NaP} is a depolarization-activated depolarizing current (Crill, 1996). The current is regenerative, meaning it would eventually, through positive feedback, completely activate itself. However, the current is also slowly inactivating under depolarized conditions. When the membrane is depolarized, the current begins to inactivate on the “slow” time course of a second. The current can be de-inactivated after a sufficient duration of hyperpolarization, on the order of a second. Importantly, the dynamics of I_{NaP} are orders of magnitude slower than the Na^+ currents that mediate the action potential.

Figure 1.6 shows a simulation of a neuron with intrinsic rhythmicity facilitated by the

¹A reader with a biophysics background might interested to know this particular model rhythm is driven solely by a slowly de-inactivating low-threshold Ca^{2+} current.

slow de-inactivation of I_{NaP} . If the baseline membrane potential of the cell is slightly greater than -57 mV, the activation threshold for I_{NaP} , the current will activate and provide an inward current. Depolarization further activates I_{NaP} , and if the membrane potential depolarizes past the threshold for fast Na^+ channels, then the neuron will fire action potentials. However, at this depolarized state, I_{NaP} begins to inactivate; the loss of the inward current pulls the membrane back to subthreshold potentials, and the neuron goes quiet again. After a second or two in this more hyperpolarized state, I_{NaP} de-inactivates and the process repeats.

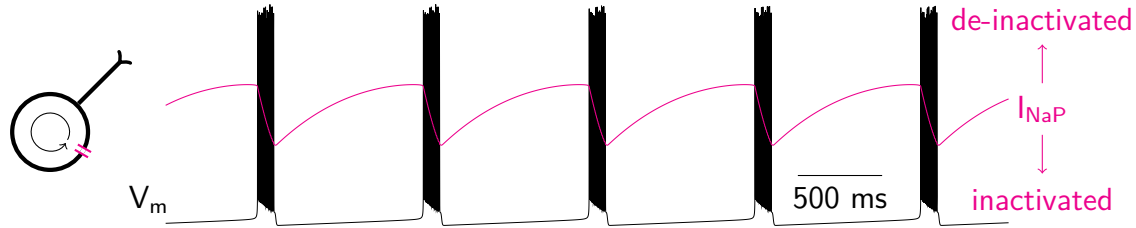


Figure 1.6: Mathematical simulation of a neuron with intrinsic rhythmicity facilitated by the slow de-inactivation of I_{NaP} . The membrane potential of the neuron is shown in black; each thick clump of vertical lines is a period of bursting. The inactivation state of I_{NaP} is shown in magenta. Higher values of this inactivation term imply that the current is de-inactivated. When the membrane depolarizes (during burst events), I_{NaP} inactivates on the time course of a hundred milliseconds. Model adapted from Butera et al. (1999).

The mechanism first proposed for the core of the inspiratory CPG in the preBötC was an I_{NaP} -mediated intrinsic pacemaker. I_{NaP} was shown to exist in preBötC interneurons and at baseline membrane potential (set by the leak current) these neurons rhythmically burst without external input (Del Negro et al., 2002a; Johnson et al., 1994; Smith et al., 1991). However, it still had not yet been shown that these rhythmic neurons were drove the inspiratory rhythm. In 2002, it was shown that the inspiratory rhythm continued even after pharmacologically blocking I_{NaP} with the sodium-channel blocker riluzole (Del Negro, 2005; Del Negro et al., 2002b). Only at high concentrations of riluzole ($\geq 20 \mu\text{M}$) could the rhythm be silenced. Though this was likely due to a disruption in network-wide synaptic

signaling, as at those concentrations riluzole interferes with fast voltage-gated sodium channels on presynaptic terminals, as well as with *N*-methyl-D-aspartate (NMDA) receptors on the postsynaptic neuron (Doble, 1996). Additional pharmacological studies with alternative Na^+ channel antagonists yielded similar results and concluded that I_{NaP} is not necessary for inspiratory rhythmogenesis (Pace et al., 2007). These findings cast doubt on the pacemaker hypothesis for inspiratory rhythmogenesis, and led the field to consider alternative mechanisms that might underlie the inspiratory CPG.

Synaptic inhibition is another mechanism that is often involved in network rhythmicity. The negative feedback intrinsically generated by inhibitory signals in a system leads to oscillations in properly configured CPG networks provided the time scale of the feedback is sufficiently slower than the excitation. Another well-understood inhibition-dependent CPG mechanism is the half-center oscillator (Stuart and Hultborn, 2008). Here, at least two neurons are connected via reciprocal inhibition (Figure 1.7). When neuron A fires, it silences neuron B. As neuron A relaxes, neuron B is released from its inhibition, sending inhibitory signals back to neuron A. As neuron B starts to relax, neuron A recovers from its inhibition and begins to fire, inhibiting neuron B. This process can repeat, and drive a network of downstream neurons in a network-wide rhythm. Both of these mechanisms for rhythm generation, initially proposed to underlie respiratory rhythm (Clark and von Euler, 1972; Feldman, 1986; von Euler, 1983), were dismissed in the preBötC however, as it was shown early on that when synaptic inhibition is pharmacologically blocked in the preBötC, it can still generate the inspiratory rhythm (Feldman and Smith, 1989; Gray, 1999; Janczewski et al., 2013).

Once these hypotheses for rhythm generation had been tested and ruled unlikely, the

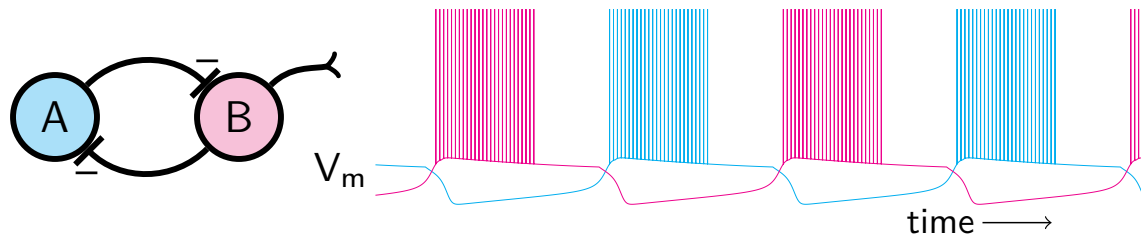


Figure 1.7: Cartoon model of a half center oscillator. Neurons A and B inhibit each other when in the up-state (firing action potentials). Model is a modified and coupled Fitzhugh-Nagumo system (FitzHugh, 1961) adapted from Conradi Smith (2019). Action potentials are added for clarity and are not part of the model.

field turned to a new theory for rhythm generation: the recurrent excitation hypothesis.

1.5 The recurrent excitation hypothesis for inspiratory rhythmogenesis

The preBötC is a heterogeneous assembly of neuron types. Inside the borders of the preBötC are excitatory (Funk et al., 1993; Wallen-Mackenzie et al., 2006) and inhibitory (Kuwana et al., 2006; Winter et al., 2009) neurons. These groups can be subdivided further based on the presence of specific intrinsic membrane currents and peptide receptors (Gray, 1999; Guyenet and Wang, 2001; Guyenet et al., 2002; Stornetta et al., 2003a,b). Among glutamatergic (excitatory) neurons, two neuron types have been identified and extensively characterized. We refer to these neural types as type-1 and type-2 neurons². Both neuron types have similar morphology, and typically express the transcription factor Dbx1 during embryonic development (see Section 1.3 for more on genetic markers). However, the two neuron classes can be distinguished by their electrophysiological properties and by their contribution to the inspiratory rhythm (Gray, 1999; Picardo et al., 2013; Rekling et al., 1996).

Type-1 neurons typically start to spike a few seconds before the upcoming inspiratory burst, and their spiking frequency increases as the inter-event interval progresses. Approximately 400 milliseconds prior to the network-wide burst (Picardo et al., 2013; Rekling et al., 1996), type-1 neurons exhibit a ramp of depolarization, and then fire in sync with the inspiratory burst. The type-1 neuron undergoes a post-burst hyperpolarization lasting approximately one second. In intracellular recordings, type-1 neurons exhibit I_A , a depolarization-activated outward K^+ current most strongly appearing in the dendrites (Hayes et al., 2008;

²These classifications apply only to interneurons in the preBötC and should not be confused with the nomenclature used to describe different classes of cell excitability (Hodgkin, 1948; Prescott et al., 2008).

Phillips et al., 2018; Picardo et al., 2013; Rekling et al., 1996). As a result, after a type-1 neuron has been hyperpolarized below -65 mV for a few hundred milliseconds, they display a delayed excitatory response to depolarizing stimulus. Lastly, type-1 neurons do not express the hyperpolarization-activated mixed cationic current I_h .

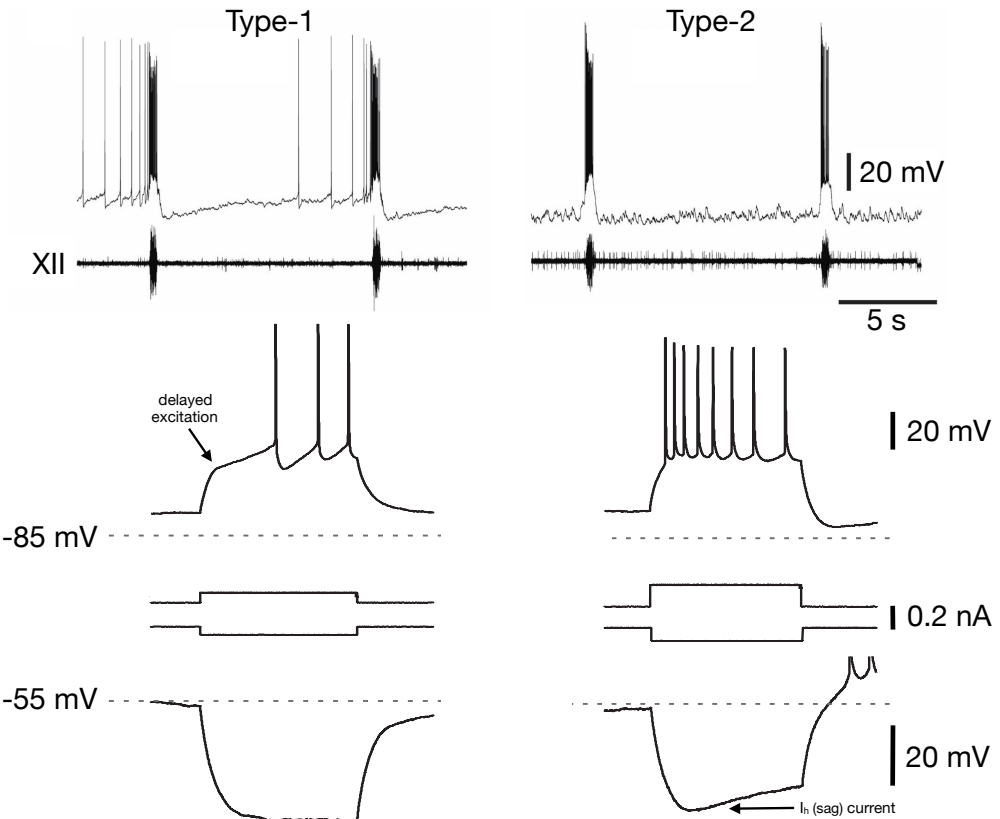


Figure 1.8: Electrophysiological properties of type-1 and type-2 preBötC interneurons. The trace on the upper left show the membrane potential of a type-1 neuron during preBötC respiratory activity. On the right is the membrane potential for a type-2 neuron during respiratory activity. Below these are electrophysiological responses of type-1 (left) and type-2 (right) neurons to depolarizing and hyperpolarizing current injections. Type-1 neurons exhibit delayed excitation during the onset of depolarizing current. Type-2 neurons display a characteristic sag current (mediated by I_h) after hyperpolarization. Top two traces are adapted from Rekling et al. (1996). Bottom traces, including the electrophysiological experiments, are adapted from Picardo et al. (2013).

In contrast, the type-2 neurons do not increase their spiking frequency as the next inspiratory burst approaches. Typically, type-2 neurons are quiescent throughout the interburst interval. Their depolarization ramp before the inspiratory burst is shorter too (typically 150 ms or less). Similarly, their hyperpolarization following the inspiratory burst lasts only a

few hundred milliseconds. With regard to subthreshold currents, type-2 neurons do exhibit I_h , a hyperpolarization-activated mixed-cation current, but not I_A .

The hypothesis for recurrent excitation postulates that activity percolates through the network through increasing activity of type-1 neurons. In a network of excitatory neurons, if the strength of the synapses is strong enough and constituent neurons are sufficiently mutually interconnected (Rekling et al., 2000), activity among the neurons will continue to grow, until the entire network is firing at some maximum rate. The rapid (400 ms) ramp of depolarization seen in the type-1 neurons corresponds to the last-stages of this positive-feedback loop. The burst is terminated by several possible factors. One component is the rundown of the synapses due to synaptic depression (Guerrier et al., 2015; Kottick and Del Negro, 2015). Another contribution to burst termination is activity-dependent outward currents such as Ca^{2+} -activated K^+ currents, as well as electrogenic pumps such as the Na^+-K^+ transporter (Del Negro et al., 2009; Krey et al., 2010). As these termination mechanisms diminish, type-1 neurons start to communicate and activity in the network begins to percolate, and the process repeats. This network oscillation is an emergent property of the connected system. The oscillation would not appear in an individual cell, because a neuron cannot typically excite itself synaptically, but when interconnected via recurrent synapses the rhythmic behavior of the network can emerge.

In this framework, type-2 neurons are hypothesized to act as filters for the premotor output. They don't facilitate the network oscillation, but they help bolster the signal and are responsible for sending the signal outside of the preBötC.

The idea that recurrent excitation is the necessary mechanism for rhythmicity is a system-level question that is notoriously difficult to prove. After all, disrupting the neurons

ability to communicate with each other will destroy any network oscillation, regardless if the source rhythmogenic mechanism is pacemaker activity or emergent network properties. Years after the discovery of type-1 and type-2 neurons, a more complete understanding of the recurrent excitation hypothesis has developed, known as the burstlet hypothesis.

In 2013a, a group studying inspiratory rhythmogenesis in reduced slice preparations noticed that under low-excitability conditions, undersized bursts would emerge from the preBötC. These small bursts, dubbed “burstlets”, were several times smaller than a regular inspiratory network burst. Importantly, these burstlets failed to evoke a motor output in the XII rootlet (Figure 1.9) (Kam et al., 2013a). As network excitability is reduced, by lowering the extracellular K^+ concentration, the inspiratory rhythm frequency decreases and concomitantly a larger fraction of events are classified as burstlets.

This discovery, in conjunction with later work done by my colleague Prajita Kallurkar (Kallurkar et al., 2020), laid the framework for the burstlet theory for rhythmogenesis. In essence, activity percolates in the preBötC through type-1 Dbx1-derived interneurons. If excitability is high enough, recurrent excitation amongst these neurons recruits voltage-dependent inward currents, such as I_{CAN} . These currents bolster activity in the interneurons, and facilitate the transmission of the activity to pattern-forming circuits such as type-2, or premotor neurons, which send the burst signal out of the preBötC. A burstlet occurs when activity amongst the neurons is too low to trigger the pattern-forming currents.

The burstlet hypothesis is the current working model for inspiratory rhythmogenesis in the respiratory field. However, there are still a few questions about this framework. For example, the 2-3 second interval before the burst event, known as the preinspiratory phase, is still mechanistically unclear. My question is: what cellular or synaptic mechanisms facilitate

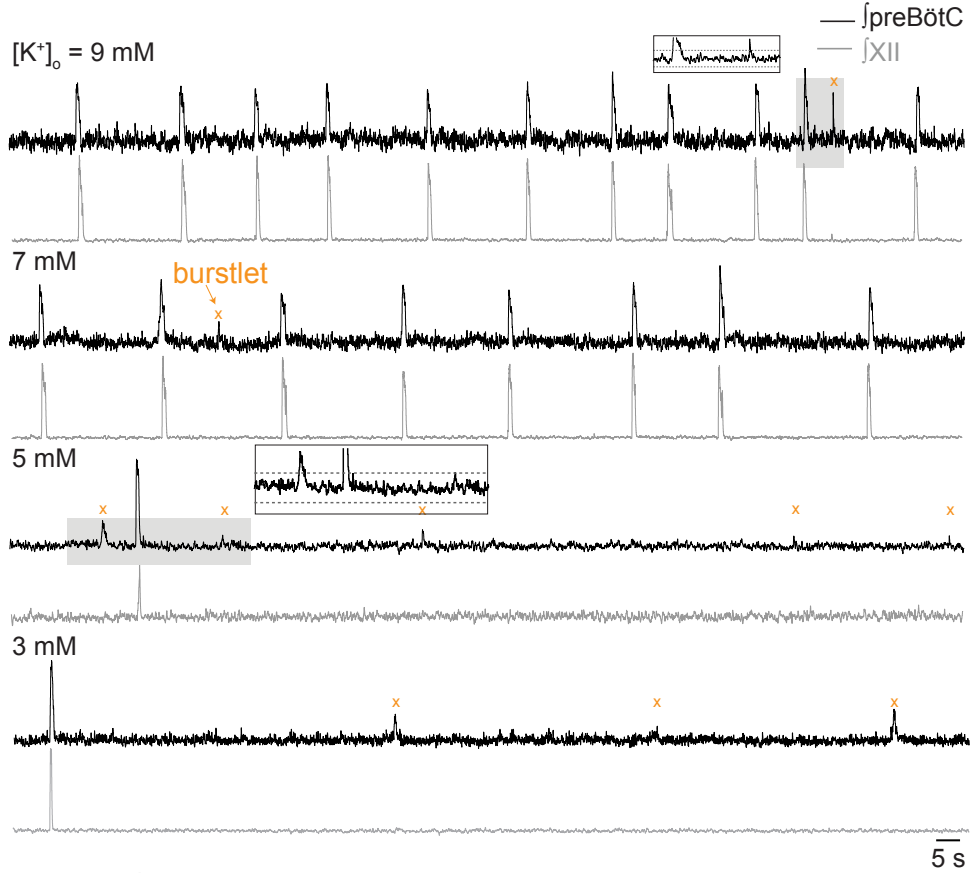


Figure 1.9: Field and nerve recordings from the preBötC at various values of extracellular K^+ ($[\text{K}^+]_o$). Lower $[\text{K}^+]_o$ indicates decreased network excitability. An event is considered a burstlet when the amplitude exceeds two standard deviations above the mean of the baseline noise in the recording, and the event does not have an associated burst in XII. Burstlets are highlighted with an orange x. The ratio of burstlets to bursts increases as excitability decreases. This figure is adapted from Kallurkar et al. (2020).

such a prolonged build up of network activity? Recent attempts at answering this question have been made by Ashhad and Feldman (2020) and Slepukhin et al. (2020). Chapter 3 reviews my work in this area.

1.6 History of sigh rhythmogenesis

The origin of the sigh rhythm has been an area of active research since 2000, when it was discovered that the rhythm originated in the preBötC, alongside the inspiratory rhythm (Li and Yackle, 2017; Lieske et al., 2000; Ramirez, 2014). Besides discovering that the sigh

rhythm appeared to emanate from the preBötC, akin to the well established inspiratory rhythm, Lieske et al. (2000) showed that the inspiratory and sigh bursts could be decoupled by blocking synaptic inhibition. This was the first bit of insight into the mechanisms that couple inspiratory breaths and sighs. However, as discussed in Chapter 2, this finding turned out to be wrong.

Six years later, the same group showed that synaptic communication, specifically mediated by NMDA receptors and some classes of metabotropic glutamate receptors (mGluRs), was involved in generating the sigh rhythm (Lieske and Ramirez, 2006a,b). The same studies were the first to implicate Ca^{2+} as having a role in sigh generation. In this case, they showed antagonizing P/Q-type Ca^{2+} channels decreased or eliminated sighs. Conversely, they also showed that antagonizing N-type Ca^{2+} channels actually increased sigh frequency. Each of these subtypes (P/Q/N) are high-voltage-gated Ca^{2+} channels, and are primarily involved in transmitter release at synaptic terminals (Luebke et al., 1993; Nimmrich and Gross, 2012). Therefore, this connection between Ca^{2+} dynamics and the sigh rhythm is still largely related to their main argument, that synaptic communication between preBötC interneurons is involved in generating sighs.

In 2008, the same group reported two major findings regarding sigh rhythmogenesis (Tryba et al., 2008). First, they claimed to have identified a population of sigh-only neurons. Sigh-only neurons would be a subgroup of preBötC neurons that are active expressly during network-wide sigh events. This discovery suggested that these sigh-only neurons were likely at the core of the sigh rhythm, and may be driving sighs throughout the preBötC. The group reported that only a small subset of preBötC neurons, around 5%, were sigh-only neurons. When the group attempted to synaptically isolate these sigh-only neurons, to determine if

they would continue to generate a sigh rhythm endogenously, they found none of the sigh-only neurons tested intrinsically rhythmically active with a cycle period equivalent to the sigh rhythm. This is consistent with the above mentioned findings that the sigh rhythm is dependent on synaptic communication (Lieske and Ramirez, 2006a,b).

The second major insight from Tryba et al. (2008), which also corroborated work from Lieske and Ramirez (2006a,b), was that blocking Ca^{2+} channels, this time with the nonselective Ca^{2+} -channel antagonist cadmium, disrupted sigh rhythm generation. Because the effect of cadmium is not localized to Ca^{2+} -channels on synaptic terminals, this result implicated a potential role for somatic (not just synaptic terminal) intracellular Ca^{2+} in sigh rhythmogenesis.

Two important contributions towards understanding the sigh rhythm were made by another group. Ruangkittisakul et al. (2008) found that slice preparations that captured the preBötC as well as more of the rostral boundaries of the medulla were more likely to produce sighs than those slices that cut the rostral boundary at or even within the rostral margin of the preBötC. The upshot of Ruangkittisakul et al. (2008) was to propose that slices that retain a bit more tissue rostral to the preBötC retained cut axons from a rostral circuit that regulated (facilitated) sigh rhythmogenesis. This was a prescient insight that Li et al. (2016, 2020) picked up on and explained.

The second valuable finding from this work, which directly contradicts the conclusions made in Tryba et al. (2008), was the observation that all inspiratory preBötC neurons were active during inspiratory and sigh bursts. The team concluded, from Ca^{2+} imaging studies, that the inspiratory and sigh rhythms arise from the same population of neurons, i.e., there are no sigh-only neurons. This question of whether it is one or two populations of neurons

driving inspiration and sighs will be revisited in Chapter 4. There, we show that putative ‘sigh-only’ neurons are an artifact of reduced slice preparations where the inspiratory rhythm is so small in amplitude as to be unrecognizable under typical conditions *in vitro*.

The largest step towards a complete model for sigh rhythm generation was made in 2015 by Toporikova et al.. They expanded on the idea of Ca^{2+} dependence, and suggested the sigh rhythm was the result of an intracellular Ca^{2+} oscillation. In their model, Ca^{2+} movement between the cytosol and ER on the time course of minutes drives sigh events. They use both pharmacology and a mathematical model to build and support their model for sigh rhythmogenesis.

However, in recent years it has become clear there are some gaps in this model. First, their model consists of two separate “populations” of cells, one that drives the inspiratory system and another that drives sighs. However, data from Ruangkittisakul et al. (2008), as well my own data (discussed in Chapter 4), contradicts the notion that the sigh rhythm is generated by a separate population of neurons. Another problem is that sighs in their model depend on the hyperpolarization-activated mixed-cation current, I_h . Whereas Chapter 4 will show that sighs continue to emerge after I_h is blocked *in vitro*. Though it is a minor detail from the perspective of sigh rhythmogenesis, their model posits that the inspiratory rhythm is driven by the slow dynamics of I_{NaP} , which has been roundly disproved (recall Section 1.4). Finally, the mechanism that couples the inspiratory and sigh rhythms in their model depends on synaptic inhibition. Although synaptic inhibition has been shown to link the two rhythms in embryonic tissue (Chapuis et al., 2014; Lieske et al., 2000), their interpretation was premature because we recently showed that GABA and glycine synapses in the preBötC are effectively excitatory at embryonic and early post-natal stages of development. In fact,

we discovered that it is synaptic excitation that links the rhythms after birth (Borrus et al., 2020), which would also apply to functionally excitatory GABA and glycine synapses pre- and peri-natally.

Chapter 4 develops a complete model for inspiratory and sigh rhythmogenesis that corrects for these deficiencies.

Chapter 2

Role of synaptic inhibition in the coupling of the respiratory rhythms that underlie eupnea and sigh behaviors

2.1 Introduction

Under physiological conditions breathing behavior consists of two interleaving rhythms and motor patterns: eupnea and sighing. Eupnea is the normal unl labored breathing that underlies rhythmic lung ventilation and drives alveolar gas exchange. Eupnea occurs at approximately 1–4 Hz in rodents (0.2–0.3 Hz in humans); each breath ventilates a small fraction of lung capacity. Sighs are also inspiratory breaths, but the volume of inhaled air during a sigh is two to five times that of a normal breath, and sigh frequency is an order

of magnitude lower than the eupnea rhythm rhythm (Li and Yackle, 2017). Sighs reinflate collapsed (or collapsing) alveoli and are essential for optimal pulmonary function. Typically, sighs appear to ride atop ongoing eupneic breaths (Cherniack et al., 1981; Orem and Trotter, 1993), which suggests that periodically, but at a much lower frequency, the eupnea cycle triggers the sigh. After a sigh, the next eupneic breath is delayed for a duration roughly equivalent to one additional eupneic cycle (Cherniack et al., 1981; Orem and Trotter, 1993). This delay, which we refer to as the post-sigh apnea, suggests that sighs prolong the time to the next eupneic breath. Eupnea and sigh breathing rhythms thus appear to be coupled, most likely via neural microcircuits of the brainstem that generate and control breathing movements.

In mammals, eupnea and sigh rhythms emanate from the preBötzinger complex (preBötC) of the lower brainstem (Del Negro et al., 2018; Smith et al., 1991). Both rhythms are maintained in reduced slice preparations that isolate the preBötC as well as inspiratory premotor and motor neurons, and thus encapsulate a minimal breathing-related model system (Chapuis et al., 2014; Lieske et al., 2000; Ruangkittisakul et al., 2008). Because eupnea refers to behavior in living animals, inspiratory is the appropriate nomenclature for eupnea-related activity in slice preparations. Inspiratory rhythm depends on network properties, in which recurrent excitation among glutamatergic interneurons is rhythmogenic (Ashhad and Feldman, 2020; Del Negro et al., 2002b; Feldman and Kam, 2015; Funk et al., 1993; Rekling et al., 2000; Wallen-Mackenzie et al., 2006). The rhythmogenic mechanism of sighs is unknown, but maintenance of the sigh rhythm depends on neuropeptides released by parafacial respiratory interneurons (Li et al., 2016) as well as excitatory ionotropic and metabotropic receptor-mediated synaptic transmission (Lieske and Ramirez, 2006a,b).

Inspiratory bursts appear to trigger sigh-related bursts, and in turn, sigh-related bursts delay the next inspiratory burst by almost an entire cycle (Lieske et al., 2000; Tryba et al., 2008). These observations *in vitro* mirror the *in vivo* coupling behavior described above, which suggest that the mechanisms coupling inspiratory and sigh rhythms are contained within the preBötC and can be examined at the cellular and synaptic level *in vitro*.

What mechanisms couple these two rhythms? The only existing data suggest that glycinergic synaptic inhibition links the sigh-related burst to its preceding inspiratory burst, thus giving rise to the biphasic shape in which the inspiratory burst appears to trigger the sigh (Lieske et al., 2000). A recent mathematical model (Toporikova et al., 2015) posits two discrete systems for generating eupnea and sigh oscillations. The model inspiratory system acts on the sigh system via synaptic inhibition such that sigh bursts emerge via an escape-like process triggered by disinhibition at the tail end of inspiratory bursts. The model also suggests that the sigh system projects to the inspiratory system via fast excitatory synapses, and the strength of its excitation leads to a transient state of refractoriness, i.e., the post-sigh apnea, in the coupled system. However, the post-sigh apnea might also be attributable to synaptic inhibition from the sigh system onto the inspiratory rhythm generator.

Here, we challenge two longstanding ideas regarding the sigh rhythm: that when a sigh occurs, it emerges immediately following the associated eupneic breath, and that synaptic inhibition is responsible for this temporal relationship. First, we describe previously undocumented variability in the timing of a sigh breath relative to the previous eupneic event. We show, both *in vivo* and *in vitro*, that a sigh event can occur simultaneously, and even precede, the inspiratory event. Next, we block glycinergic transmission and show that disinhibiting the preBötC *in vitro* does not uncouple the eupnea- and sigh-related rhythms, but

in fact appears to couple them more strongly. We obtain similar results when simultaneously blocking GABAergic and glycinergic transmission.

We extend our investigation of synaptic inhibition in coupling the two breathing rhythms by analyzing the post-sigh apnea *in vitro* before and after blockade of ionotropic inhibition. We show the duration of the post-sigh apnea does not depend on glycinergic or GABAergic transmission and we infer that the post-sigh apnea reflects a refractory state attributable to postsynaptic membrane properties evoked by the sigh burst. Lastly, we measure the chloride reversal potential (E_{Cl}) in putatively rhythmogenic preBötC neurons and meta-analyze the development of E_{Cl} in mice and rats, in order to verify that glycine and GABA_A synapses are inhibitory postnatally, and not functionally excitatory as they are during embryonic development (Delpy et al., 2008; Ren and Greer, 2006). We propose that the eupnea and sigh rhythms are coupled predominantly by excitatory (rather than inhibitory) synaptic mechanisms.

2.2 Results

2.2.1 Sigh breaths follow eupneic breaths with variable time intervals

We recorded breathing in unanesthetized adult mice, analyzing 229 sigh breaths across 7 animals. We measured the time interval between a sigh and its associated (generally preceding) eupneic breath, which we refer to as the eupnea-sigh interval. Figure 2 shows the distribution of the eupnea-sigh intervals with three representative traces corresponding to eupnea-sigh intervals that fall within three characteristic parts of the distribution. In 174 of

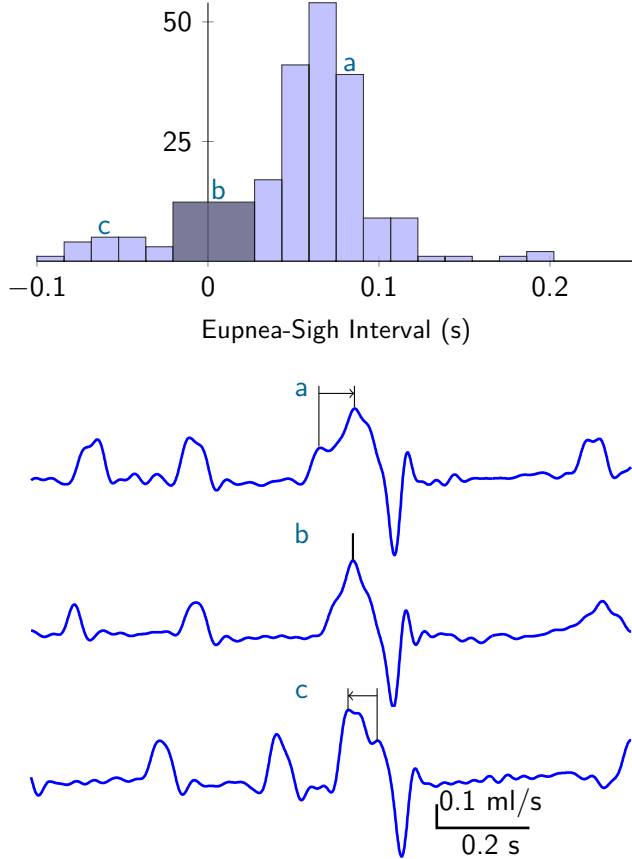


Figure 2.1: Variable timing of sigh breaths *in vivo*. Top: histogram of the eupnea-sigh time intervals. Bin size is 0.016 seconds. Intervals near zero were pooled into one bin of size 0.048 seconds because distinct eupnea- and sigh-related peaks in the signal could not be distinguished. Bottom: sample sweeps from plethysmography recordings from one mouse. Lowercase letters a, b, and c illustrate eupnea-sigh intervals that appear in corresponding bins plotted in the histogram above.

the 229 sighs (76%), the sigh emerged after the eupneic breath, leading to a positive eupnea-sigh interval (Figure 2.1, trace a). This represents the canonical sigh pattern, whereby the inspired volume of the sigh builds off, and exceeds, the tidal volume marking the peak of a eupneic breath. Surprisingly however, the remaining 55 sighs (24%) did not follow the canonical pattern. In 37 cases (16%), the sigh appeared unaccompanied by a eupneic breath. We infer that the eupneic and sigh event occurred simultaneously, or close enough together so as to be indistinguishable, thus leading to an observed event interval of 0 seconds (Figure 2.1, trace b). In 18 cases (8%), the sigh breath was followed by a eupneic breath whose peak

corresponds to tidal volume, then followed by a post-sigh apnea. This type of sigh pattern led to a negative eupnea-sigh interval (Figure 2.1, trace c). The presence of null and negative eupnea-sigh intervals (Figure 2.1, traces b and c, respectively) suggest that eupneic breaths are not obligatory for triggering a sigh.

2.2.2 Sigh bursts follow inspiratory bursts with variable time intervals

We next investigated the coupling relationship between eupnea and sigh rhythms using slice preparations that retain the preBötC and spontaneously generate inspiratory and sigh-related activity measurable in the preBötC and XII nerve rootlets. We measured 343 sigh bursts in 13 slice preparations (26 ± 7 sigh bursts per slice) via a field recording electrode. We measured the time interval between a sigh burst and its associated inspiratory burst, which we refer to as the inspiratory-sigh interval (Figure 2.2A). To account for the intrinsic slice-to-slice variation in inspiratory frequency, we normalized inspiratory-sigh interval (T_σ) by the average of the six preceding inspiratory cycle periods (\bar{T}). Figure 2.2A shows the distribution of inspiratory-sigh intervals (top), as well as representative field recordings of sigh bursts with different inspiratory-sigh intervals that map to specific parts of the distribution (Figure 2.2A shows the correspondence via lowercase letters a–e).

Inspiratory and sigh events recorded from XII motor output closely resemble the integrated preBötC field recording when considering inspiratory-sigh timing. We analyze the integrated field recording exclusively because it reflects activity of the core rhythmogenic microcircuits in the preBötC.

Inspiratory bursts tend to precede sigh bursts, as the distribution of inspiratory-sigh

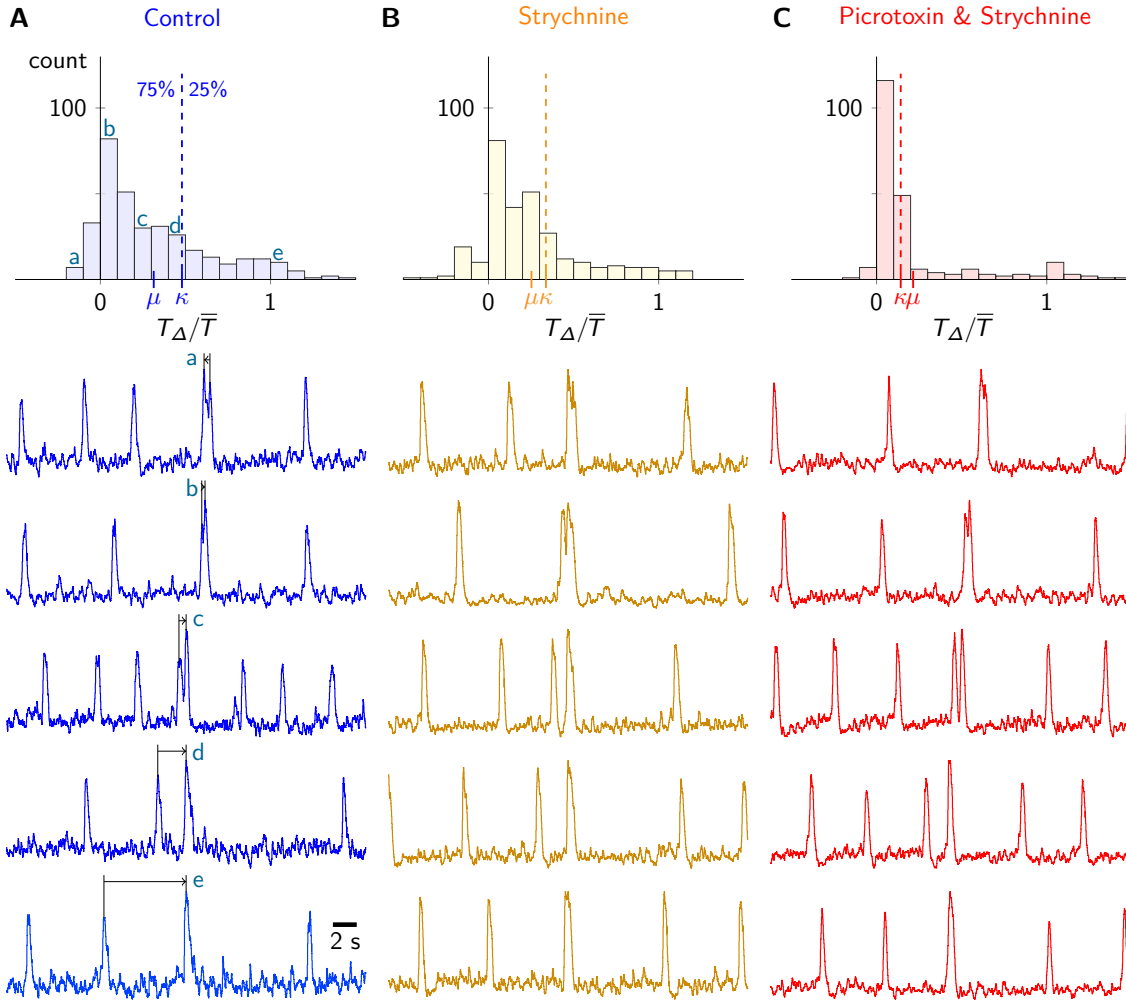


Figure 2.2: Variable timing of sigh bursts in vitro. A: histogram of normalized inspiratory-sigh intervals (T_σ/\bar{T}) for all sigh bursts in all 13 rhythmically active slices under control conditions. The width of each bar is $0.1 T_\Delta/\bar{T}$. μ marks the mean of the distribution and κ denotes the 75th percentile line. Below are representative preBötC field recording traces depicting a variety of inspiratory-sigh intervals. Traces come from different slices. Lowercase letters a, b, c, d, and e connect representative traces with their position on the inspiratory-sigh interval histogram above. B-C: identical inspiratory-sigh interval analysis in the presence of 5 μM strychnine (B) as well as both 5 μM strychnine and 5 μM picrotoxin (C).

intervals is weighted towards positive values of T_Δ/T_σ close to 0 (Figure 2.2A, e.g., trace b).

However, inspiratory-sigh intervals varied considerably. For example, only 133 sighs (39%) appeared within the first fifth of the inspiratory cycle. Rather, we observed inspiratory-sigh intervals that ranged across the entire inspiratory cycle (Figure 2.2A, traces b-e). Additionally, we observed 40 sigh bursts (12%) that appeared to be followed by inspiratory bursts

and then post-sigh apneas, thus indicating a negative inspiratory-sigh interval (Figure 2.2A, trace a).

2.2.3 Inhibitory synapses do not link sigh bursts to the inspiratory rhythm

To perturb the temporal coupling between the inspiratory and sigh rhythms we blocked glycinergic synaptic transmission using strychnine. The probability distribution of inspiratory-sigh intervals remained weighted towards the first half of the normalized cycle ($T_\Delta/\bar{T} < 0.5$, Figure 2.2B), suggesting that inspiratory-sigh coupling remained intact. In contrast, previous studies suggested that blocking glycinergic synapses eliminated the temporal relationship between sigh bursts and their preceding inspiratory bursts (Chapuis et al., 2014; Lieske et al., 2000), in which case the probability distribution in Figure 2.2B would be uniformly distributed between 0 and 1. Here, the probability of short inspiratory-sigh intervals ($T_\Delta/\bar{T} < 0.5$) increased such that the mean inspiratory-sigh interval decreased from $T_\Delta/\bar{T} = 0.31 \pm 0.34$ in control (μ in Figure 2.2A) to $T_\Delta/\bar{T} = 0.25 \pm 0.30$ in the presence of strychnine (μ in Figure 2.2B). This trend is reflected in the significant leftward shift of the cumulative distribution function towards, but not below, an inspiratory-sigh interval of 0 from control to strychnine conditions (Figure 2.3, Kolmogorov-Smirnov, test statistic = 0.13, $p = 0.011$, $n = 7$ slices). The left shift of the entire inspiratory-sigh interval distribution is further illustrated by the decrease of the 75th percentile score (indicated by κ in Figures 2.2 and 2.3) from $T_\Delta/\bar{T} = 0.48$ in control to $T_\Delta/\bar{T} = 0.34$ in strychnine.

Similarly, when we simultaneously blocked glycine and GABA_A receptors with a strychnine and picrotoxin cocktail, the sigh burst coupled more tightly with the preceding inspi-

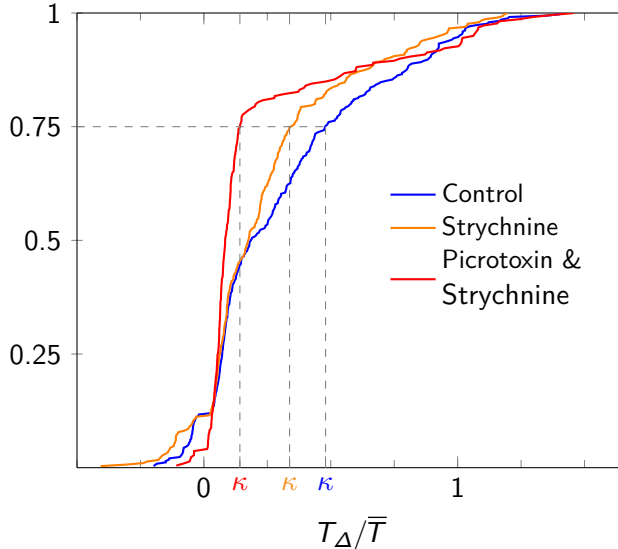


Figure 2.3: Cumulative probability histograms showing the normalized inspiratory-sigh interval (T_Δ/\bar{T}) under control conditions (blue), 5 μM strychnine (orange), as well as 5 μM strychnine and 5 μM picrotoxin (red). κ marks the 75th percentile line for each distribution, distinguished by color. This analysis pools all sighs measured across all 13 slices.

ratory burst than in control conditions, as shown by the accumulation of inspiratory-sigh intervals within the first two bins of the inspiratory-sigh interval histogram (Figure 2.2C). The probability of short inspiratory-sigh intervals ($T_\Delta/\bar{T} < 0.5$) increased from control to the strychnine and picrotoxin cocktail such that the average normalized inspiratory-sigh interval decreased from $T_\Delta/\bar{T} = 0.31 \pm 0.34$ in control (μ in Figure 2.2A) to $T_\Delta/\bar{T} = 0.21 \pm 0.32$ in strychnine and picrotoxin (μ in Figure 2.2C). The significant leftward shift of the cumulative distribution function towards, but not below, an inspiratory-sigh interval of 0 further demonstrates that when both glycine and GABA_A receptors were blocked, sigh bursts occurred earlier with respect to preceding inspiratory bursts than during control (Figure 2.3, Kolmogorov-Smirnov, test statistic = 0.31, $p = 4.0\text{E-}12$, $n = 6$ slices). The 75th percentile score (κ in 2.2 and 2.3) drops from an inspiratory-sigh interval of $T_\Delta/\bar{T} = 0.48$ in control to $T_\Delta/\bar{T} = 0.14$ in strychnine and picrotoxin. Whereas in control and strychnine conditions $\mu \downarrow \kappa$ (the mean of the distribution was within the 0–75th percentile range) in the

combined presence of strychnine and picrotoxin $\kappa \downarrow \mu$, which shows that the vast majority of inspiratory-sigh intervals (in 0–75th percentile range) are shorter than the mean.

Note that the large standard deviation associated with the average inspiratory-sigh intervals (0.31 ± 0.34 in control, 0.25 ± 0.30 in strychnine, and 0.21 ± 0.32 in strychnine and picrotoxin) reflects the inherent inspiratory-sigh interval variability as illustrated in Figure 2.2.

Our analyses (Figures 2.2 and 2.3) show the removal of chloride-mediated synaptic inhibition does not uncouple the sigh from its preceding inspiratory burst, but rather disinhibition strengthened the temporal coupling of inspiratory and sigh bursts.

2.2.4 Inhibitory synapses do not influence post-sigh apnea

We calculated the relative duration of the post-sigh apnea as the duration of the post-sigh interval (T_σ) divided by the average of the six preceding inspiratory cycle times (\bar{T}). We compared the relative duration of the post-sigh apnea (T_σ/\bar{T}) in control and after blocking either glycinergic transmission, or both glycinergic and ionotropic GABAergic transmission (Figure 2.4). The relative duration of the post-sigh apnea measured 1.65 ± 0.20 in control, 1.72 ± 0.25 in strychnine, and 1.5 ± 0.09 in the strychnine-picrotoxin cocktail. These measurements are statistically indistinguishable (one-way ANOVA, $F_{2,11} = 2.12$, $p = 0.14$, $n = 13$ slices).

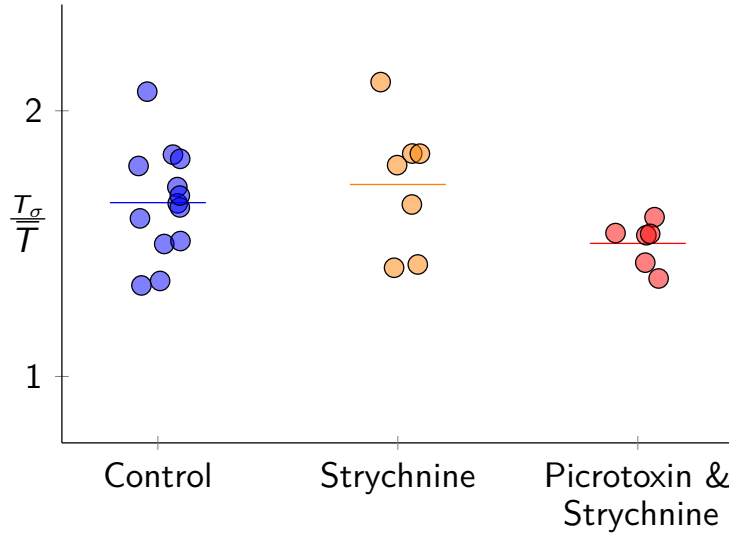


Figure 2.4: Average relative duration of the post-sigh apnea in control (blue), 5 μM strychnine (orange), as well as 5 μM strychnine and 5 μM picrotoxin (red). Each dot represents the average normalized post-sigh apnea for all sighs recorded in one slice. Horizontal bars represent the average of all slices in each condition.

2.2.5 Chloride-mediated synaptic transmission is inhibitory in the neonatal mouse preBötC

We recorded chloride-mediated synaptic potentials in preBötC neurons via gramicidin perforated patches during early postnatal development (P0–3). These experiments employed wild-type mouse slices as well as slices from Dbx1;Ai148 mice that express a fluorescent Ca^{2+} reporter (GCaMP6f) in preBötC neurons derived from Dbx1-expressing progenitors (i.e., Dbx1 neurons), which comprise the core excitatory interneurons of the preBötC (Baertsch et al., 2018; Bouvier et al., 2010; Cui et al., 2016; Gray et al., 2010; Vann et al., 2016, 2018; Wang et al., 2014). Figure 2.5A and B show the neuroanatomical structures from a Dbx1;Ai148 slice that collocate with the preBötC: the principal loop of the inferior olive (IO_{loop}) and the semi-compact division of the nucleus ambiguus (NAsc). Figure 2.5C depicts the perforated patch configuration wherein GCaMP6f expression verifies that the neuron was Dbx1-derived. Figure 2.5C also shows that Alexa 568 remains confined to the pipette

solution during perforated patch recording conditions.

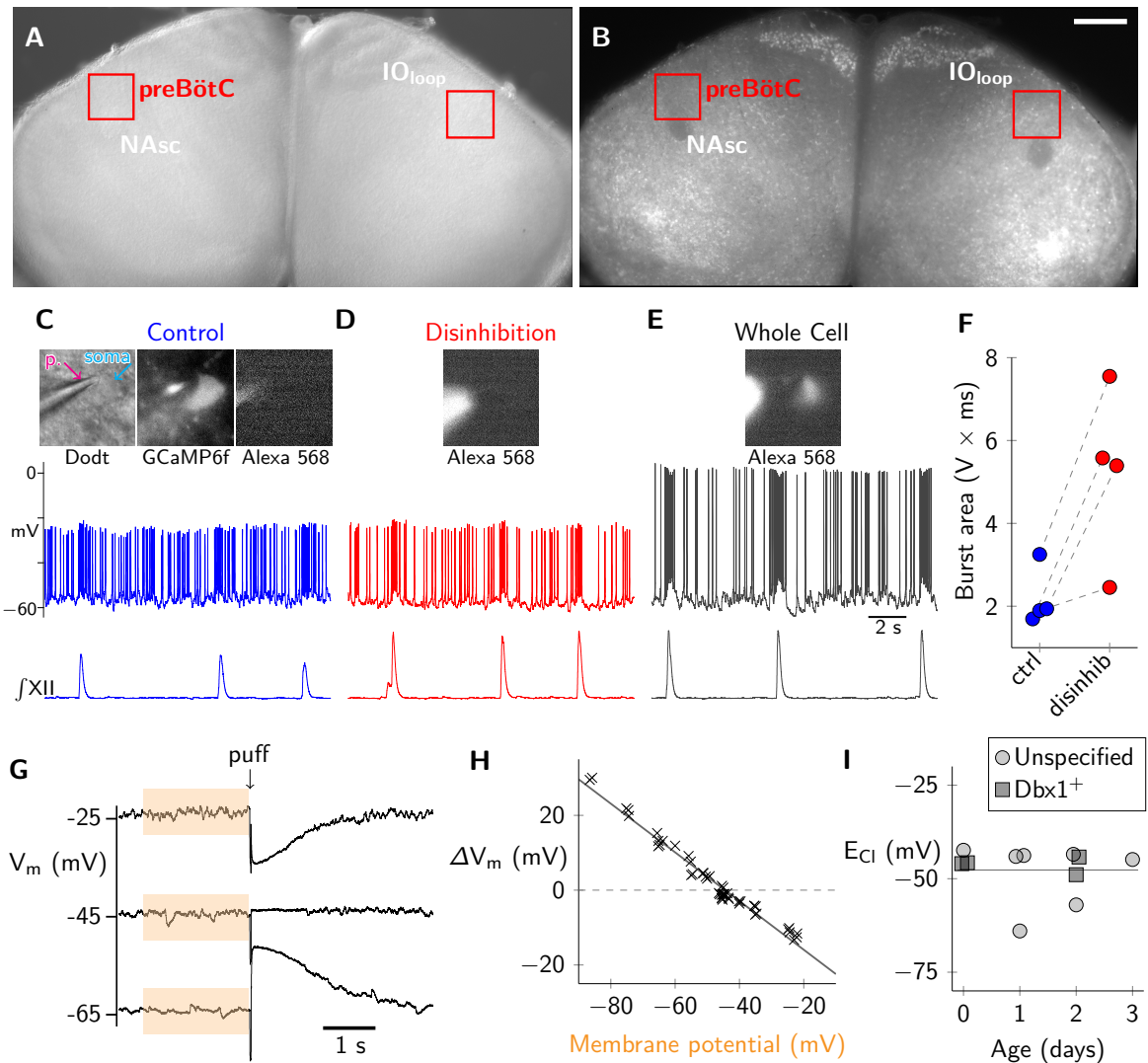


Figure 2.5: (Caption next page.)

We applied strychnine and picrotoxin to the bath simultaneously while recording Dbx1 inspiratory neurons ($n = 4$ neurons in 4 slices). We monitored the integrated area of the membrane potential trajectory during inspiratory bursts while vigilantly monitoring the integrity of the perforated patch throughout the experiment using the absence of Alexa 568 in the soma as evidence of an intact patch (Figure 2.5C and D). After blockade of chloride-mediated synapses, the average integrated area of inspiratory bursts increased from $2.2 \pm$

$0.7 \text{ V} \times \text{ms}$ in control to $5.2 \pm 2.1 \text{ V} \times \text{ms}$ (paired t-test, $t = 3.6$, $p = 0.037$, Figure 2.5F). The significant increase in burst area suggests that chloride-mediated synapses are functionally inhibitory during network bursts. As a final check, we switched from a perforated patch configuration to whole-cell and recorded the dialysis of Alexa 568 into the soma, concomitant with increased action potential amplitude, which confirmed the patch had not been breached during control and disinhibition data acquisition bouts (Figure 2.5D and E).

Next, we measured E_{Cl} in 11 preBötC neurons ($n = 7$ unspecified preBötC neurons from wild-type slices, and $n = 4$ rhythmically active Dbx1 preBötC neurons, all from different slices). In the presence of TTX, pressure-pulse ejections of muscimol and glycine transiently perturbed the membrane potential, which reversed at or below 45 mV (Figure 2.5G-I). E_{Cl} measured $48 \pm 6 \text{ mV}$ (mean \pm SD, $n = 11$ preBötC neurons recorded in $n = 10$ slices). We observed no relationship between E_{Cl} and age (Figure 2.5I), which indicates that E_{Cl} remains constant during postnatal days 0–3.

Figure 2.5: Chloride-mediated synapses are inhibitory in neonatal preBötC neurons. A-B: image of Dbx1;Ai148 slice preparation under Dodt contrast (A) and fluorescence microscopy (B). preBötC (red box) colocalized with the semi-compact division of the nucleus ambiguus (NAsc) and the principle loop of the inferior olive (IO_{loop}). Scale bar for both A and B is $500 \mu\text{m}$. C: Voltage trajectory of a Dbx1 preBötC neuron during formation of a gramicidin perforated patch, firing in sync with XII nerve activity. Dodt image shows the patch pipette on the neuronal soma. The magenta arrow (labeled p.) points to the patch pipette, the cyan arrow (labeled soma) indicates the patched cell body. GCaMP6f image shows the neuron was Dbx1-derived. The lack of fluorescence in the Alexa 568 image verifies the integrity of the perforated patch. D: Membrane voltage trajectory of the same neuron during blockade of chloride-mediated synaptic inhibition via addition of $5 \mu\text{M}$ strychnine and $5 \mu\text{M}$ picrotoxin in the bath. Alexa 568 continues to verify the integrity of the perforated patch. E: The same neuron in a whole-cell patch configuration shows Alexa 568 enters the soma from the patch pipette. The Dbx1 neuron is still rhythmically active and fires in sync with XII motor output. F: Average integrated burst area during either control conditions (ctrl, blue) or during glycine and GABA_A receptor blockade (disinhib, red). G: Determining E_{Cl} . Voltage trajectory before and after puffer application of $150 \mu\text{M}$ glycine and $30 \mu\text{M}$ muscimol in TTX. The average baseline membrane potential before puffer application was calculated from the previous 2 seconds of recording (orange box). The puff-evoked change in membrane voltage ($\Delta \text{ mV}$) was the difference between baseline and the peak response. H: Membrane potential changes in response to glycine and muscimol puffs plotted versus holding potential from a single representative experiment (same cell as G). E_{Cl} (read from the x-axis coordinate where $\Delta \text{ mV} = 0$ on the y-axis) is determined from linear regression (purple line). I: E_{Cl} from 11 neurons (4 Dbx1 neurons from 4 Dbx1;Ai148 mouse slices, 7 wild type neurons) plotted as a function of postnatal age. Line at 48 mV indicates the average E_{Cl} for the sample.

2.3 Discussion

Eupnea and sigh rhythms are coordinated. The conventional understanding is that sigh breaths build off the crest of eupneic breaths, and then eupneic breaths resume after the post-sigh apnea, a pronounced delay that exceeds the gap between eupneic breaths normally. Here we show that the longstanding conceptual framework for the eupnea-sigh relationship is oversimplified. We report previously unrecognized variability in the timing between eupneic and sigh breaths *in vivo*. The temporal coupling between eupnea and sigh rhythms, including its variability, may be attributable to dynamics within the preBötC because these same dynamics are mimicked in slice preparations that isolate the preBötC yet maintain both inspiratory and sigh rhythms.

The variability in the coordination of the inspiratory and sigh rhythms suggests that their coupling is weaker, relatively speaking, than previously appreciated. Sighs and sigh bursts *in vitro* with inspiratory-sigh intervals equal to or less than 0 seconds (where the sigh burst appeared coincident with, or before, the inspiratory burst) further reinforce this notion of flexibility in the relationship between a sigh burst and an associated inspiratory burst by showing that the inspiratory burst is not strictly necessary to trigger a sigh burst. Thus, a sigh can manifest independently, however, more often than not an inspiratory burst does trigger the sigh burst.

Could a sigh (or sigh burst *in vitro*) followed by a breath (or inspiratory burst *in vitro*) reflect a stand-alone sigh accompanied by a spurious artifact on the downslope of the sigh? Unlikely, we argue. In the case of animal movement during plethysmography, mice tend to move in bouts of activity lasting 1–10 s, which perturbs breathing over many consecutive cycles, and they rarely move in isolated 50–100 ms episodes that correspond to the duration

of a putative eupneic breath whose peak follows a sigh (see Figure 2.1A). For preBötC field recordings, noise-driven network activity fluctuations with magnitudes large enough to be confused with inspiratory bursts are rare. Further, *in vivo* and *in vitro*, the observed breaths (bursts) that follow the sigh events match the preceding tidal volume (inspiratory burst amplitude), which argues that they are bona fide eupneic (inspiratory) events rather than recording artifacts. Nevertheless, if we accept the possibility that the trailing event is spurious, then those negative eupnea-sigh (or inspiratory-sigh) intervals would instead be closer to one, because the preceding eupneic or inspiratory event would have occurred one entire cycle away. This abnormally long eupnea-sigh (or inspiratory-sigh) interval would further support our conclusion that sighs follow eupneic or inspiratory events with variable intervals, and that a sigh burst has no obligatory link to the preceding inspiratory burst.

Environmental conditions like hypoxia (Janssen et al., 2000) or stress (Ramirez, 2014) modulate sigh frequency. Bombesin-like peptides delivered by parafacial inputs to the pre-BötC influence sigh frequency (Li et al., 2016). However, it is not clear whether modulation of sigh frequency would influence the eupnea-sigh coupling.

Sighs are 2–5× the tidal volume of eupneic breaths *in vivo*, whereas sigh bursts *in vitro* exceed inspiratory bursts by only 1-2-fold. Despite this disparity in sigh event magnitudes, the temporal relationship between the two rhythms measured *in vivo* or *in vitro* remains the same, as shown in the histograms from Figures 2.1 and 2.2A. Those observations suggest that sigh magnitude does not influence eupnea-sigh (inspiratory-sigh) coupling. It is also remarkable that the sigh frequency remains constant ($0.3\text{--}0.5 \text{ min}^{-1}$) and the eupnea-sigh coupling pattern is conserved from intact adult mice to slices despite the fact that slices isolate the preBötC from all sensory feedback and some pattern-forming microcircuits. The

robustness of the sigh frequency and the eupnea-sigh coupling suggests the sigh timing, and its coupling with eupnea, is largely attributable to microcircuit mechanisms within the preBötC.

We examined the mechanisms of coupling *in vitro*. Chloride-mediated synaptic inhibition is not responsible for the temporal coupling between inspiratory and sigh bursts. Rather, removing inhibition shortened the time between a sigh burst and the preceding inspiratory burst. This conclusion contradicts prior studies showing that blockade of glycinergic transmission decoupled sighs from their preceding inspiratory bursts and created free-running sigh burst rhythms that are independent from ongoing inspiratory rhythms (Chapuis et al., 2014; Lieske et al., 2000; Toporikova et al., 2015).

We propose that the discrepancy between those prior results and our present findings are attributable to the late embryonic reversal of the chloride electrochemical gradient. Before embryonic day 15.5 in mice, the dominant expression of cotransporter NKCC1 in brainstem and spinal cord neurons elevates intracellular chloride concentration (Delpy et al., 2008; Ren and Greer, 2006; Viemari et al., 2011) such that chloride currents are inward (i.e., excitatory) at the baseline membrane potential of rhythmically active preBötC interneurons. Perinatally NKCC1 expression decreases in parallel with increasing expression of the chloride symporter, KCC2, which lowers intracellular chloride concentration (Gackiere and Vinay, 2015; Stil et al., 2009). In the mature state, dominant KCC2 expression ensures that the chloride equilibrium potential is more hyperpolarized than spike threshold as well as baseline membrane potential during rhythmic activity; chloride currents are outward and inhibitory.

Here we show, in early postnatal mouse development (P0–4) with elevated (9 mM) $[K^+]$ $]_o$ aCSF to boost slice excitability, that blocking chloride-mediated synapses leads to a larger

depolarizing drive during inspiratory bursts. This suggests that GABA_A and glycinergic inputs are effectively inhibitory, diminishing the effects of excitatory synaptic drive during inspiration. E_{Cl} measured 48 mV during early postnatal development in the preBötC. This equilibrium potential is below spike threshold and approximates the level of baseline membrane potential during the interburst interval. Therefore, GABA_A and glycinergic inputs either shunt the membrane rendering it less responsive to excitatory (depolarizing) drive or hyperpolarize it directly during the preinspiratory phase or during the inspiratory burst itself when the membrane potential trajectory exceeds 48 mV. Thus, in our experimental context strychnine and picrotoxin truly block synaptic inhibition.

We meta-analyzed the development of E_{Cl} in rodents in the context of our own E_{Cl} data (Figure 2.6). Most studies agree that E_{Cl} switches from above to below baseline membrane potential (i.e., from excitatory to inhibitory) around birth, which is consistent with our measurement of $E_{Cl} = 48$ mV. However, there is substantial variability, which may be attributable to rodent species and strain differences, as well as choice of $[K^+]_o$ in the aCSF, which impacts the electrochemical forces that operate in transporters.

Whereas we studied postnatal (P0–4) mice exclusively, Chapuis et al. (2014) and Toporikova et al. (2015) studied embryonic mice (E15.5–18.5). In embryonic mouse slices bathed in elevated (8 mM) $[K^+]_o$ aCSF, E_{Cl} is more likely to be above spike threshold and consequently glycinergic synapses serve to depolarize and evoke action potentials in preBötC neurons (Delpy et al., 2008; Ren and Greer, 2006). Under these conditions, we infer that glutamatergic, glycinergic, and GABA_Aergic synapses are all effectively excitatory and link sigh bursts to their preceding inspiratory bursts. When net excitatory drive is perturbed (such as by blocking chloride-mediated synapses) then inspiratory-sigh coupling weakens, and the sigh

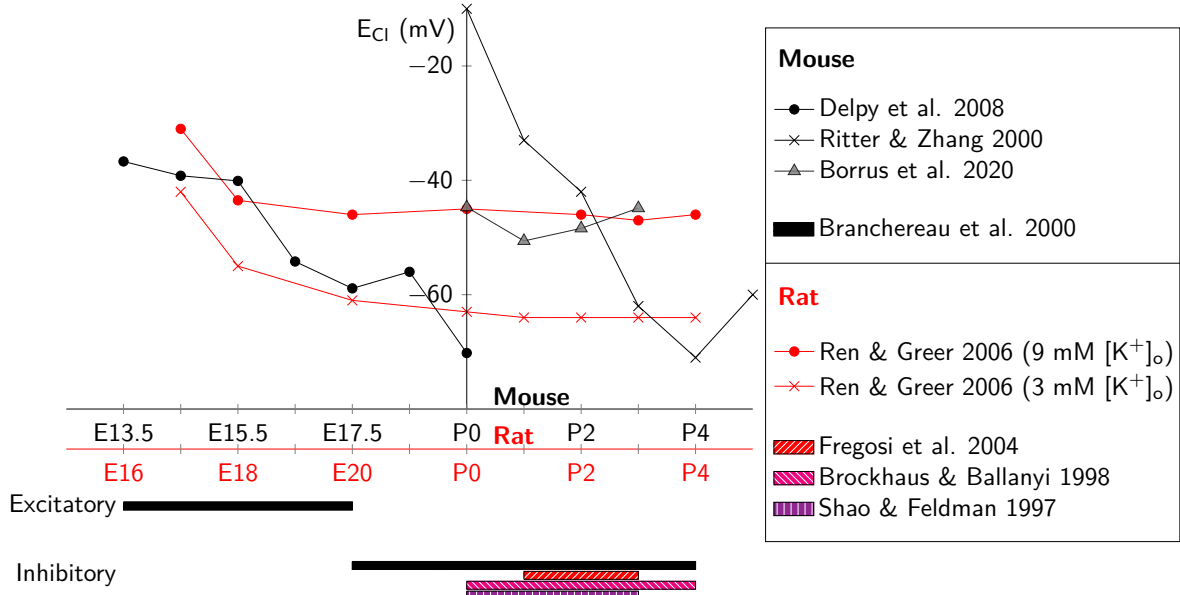


Figure 2.6: Meta-analysis of E_{Cl} during development in hindbrain and spinal cord of mice and rats. Red reflects rat data; black reflects mouse. The abscissa shows E_{Cl} (in mV) as a function of age. Below the x-axis we show binary classification of E_{Cl} as either above (excitatory) or below (inhibitory) baseline membrane potential as a function of developmental age. Our present data are labeled Borrus et al., 2020. Note: Branchereau et al. (2000); Brockhaus and Ballanyi (1998); Fregosi et al. (2004); Shao and Feldman (1997) are only cited in this figure not in the main narrative.

rhythm proceeds in a manner that is temporally independent of the inspiratory rhythm. Those results, in conjunction with our work showing disinhibition strengthens inspiratory-sigh coupling, leads us to our primary conclusion: that excitatory (not inhibitory) synaptic transmission links the inspiratory and sigh rhythms of the preBötC.

Development and chloride gradients might also explain the discrepancies between our results and Lieske et al. (2000), who also concluded that glycinergic synapses couple inspiratory and sigh rhythms. Those authors reported using mice aged 0–2 weeks, a postnatal window that overlaps and extends beyond ours. We surmise that their sigh burst experiments were performed exclusively or predominantly using preparations from P0 mice with immature chloride gradients. As Figure 2.6 shows, Ritter and Zhang (2000) employed perforated-patch recordings and reported that E_{Cl} remained depolarizing and ostensibly excitatory as late as P3. Therefore, it is conceivable, even likely, that the same explanation holds for Lieske et al.

(2000). Namely, chloride gradients favoring inward currents (with suprathreshold reversal potential) render glycine synapses ostensibly excitatory.

Chloride-mediated synaptic inhibition does not contribute to the post-sigh apnea. Instead, we suggest the post-sigh apnea is likely caused by activation of the intrinsic cellular mechanisms that help terminate inspiratory bursts, which are recruited to a greater degree during sigh events (compared to typical inspiratory cycles). These burst-terminating mechanisms include activity-dependent outward currents such as the electrogenic Na/K ATPase pump current, Na⁺-dependent K⁺ current, and ATP-dependent K⁺ current (Del Negro et al., 2009; Krey et al., 2010), as well as excitatory synaptic depression (Guerrier et al., 2015; Kottick and Del Negro, 2015). The magnitude of inspiratory burst-related depolarization directly evokes corresponding levels of post-burst hyperpolarization in preBötC neurons, from which the neurons must recover prior to generating the next inspiratory burst (Baertsch et al., 2018). The sigh burst in this context is an extreme version of that same mechanism: the increased magnitude and duration of the sigh event correspondingly evokes larger-than-average activity-dependent refractory (outward) currents and depresses excitatory synapses to a greater extent than during typical inspiratory bursts of lower magnitude and duration. The larger-than-average hyperpolarization (and depressed synapses) extends the duration of the interburst interval, thus creating the post-sigh apnea.

Here we demonstrate that chloride-mediated synaptic inhibition plays no obligatory role in coupling the inspiratory and sigh rhythms in P0–4 mice *in vitro*. Although sigh bursts are often closely preceded by inspiratory bursts, their temporal coordination is more variable than previously documented. We speculate that this principle may also apply to juvenile and adult stages because E_{Cl} is expected to remain below spike threshold and inhibitory; in

fact, we expect it to descend lower than 48 mV during further maturation. A model of the preBötC core that generates inspiratory and sigh oscillations should emphasize the primacy of excitatory synaptic interactions, which probably extends to embryonic development when chloride-mediated synapses are functionally excitatory.

2.4 Appendix: Materials and Methods

Ethical approval and animal use

The Institutional Animal Care and Use Committee at our institution approved these protocols, which conform to the policies of the Office of Laboratory Animal Welfare (National Institutes of Health, Bethesda, MD, USA) and the guidelines of the National Research Council (National Research Council (U.S.) et al., 2011). CD-1 mice (Charles River, Wilmington, MA) and genetically modified mice (described below) were maintained on a 14-hour light/10-hour dark cycle at 23°C and were fed ad libitum with free access to water.

To obtain patch-clamp recordings from preBötC neurons derived from progenitors that express the embryonic transcription factor Developing brain homeobox 1 (i.e., Dbx1) we used two Cre-driver mouse strains: homozygous knock-in mice generated by inserting an IRES-CRE-pGK-Hygro cassette in the 3 UTR of the Dbx1 gene, i.e., Dbx1Cre mice (Bielle et al., 2005) (IMSR Cat# EM:01924, RRID:IMSR_EM:01924) and homozygous knock-in mice generated by inserting an IRES-CreERT2 cassette in the 3 UTR of the Dbx1 gene, which provides conditional Cre recombinase expression following activation of the tamoxifen-sensitive estrogen receptor, i.e., Dbx1CreERT2 mice (Hirata et al., 2009; Picardo et al., 2013) (IMSR Cat# JAX:028131, RRID:IMSR_JAX:028131).

We crossed females of both strains with males from a reporter strain featuring Cre-dependent expression of the fluorescent Ca²⁺ indicator GCaMP6f dubbed Ai148 by the Allen Institute (Daigle et al., 2018) (IMSR Cat# JAX:030328, RRID:IMSR_JAX:030328). We refer to their offspring as Dbx1;Ai148 mice. During neonatal development and through adulthood, Dbx1;Ai148 mice express GCaMP6f in Dbx1-derived cells, the majority of which are neurons (Kottick et al., 2017).

Breathing-related measurements *in vitro*

Mouse pups of both sexes were anesthetized by hypothermia and then killed by thoracic transection at postnatal day 0 to 4. The neuraxis was removed in less than two minutes and further dissected in artificial cerebrospinal fluid (aCSF) containing (in mM): 124 NaCl, 3 KCl, 1.5 CaCl₂, 1 MgSO₄, 25 NaHCO₃, 0.5 NaH₂PO₄, and 30 dextrose equilibrated with 95% O₂-5% CO₂ 2, pH 7.4. Isolated neuraxes were glued to an agar block and then cut in the transverse plane to obtain a single 550 μ m-thick slice that exposed the preBötC at its rostral face. Atlases for wild-type and Dbx1 reporter mice show that the loop of the inferior olive and the semi-compact division of the nucleus ambiguus collocate with the preBötC during early postnatal development (Ruangkittisakul et al., 2011, 2014). Slices were then perfused with aCSF at 28°C in a recording chamber either below a stereomicroscope that enabled us to position suction electrodes under visual control, or on a fixed-stage microscope with dipping objectives and epifluorescence illumination to visually identify GCaMP6f-expressing (rhythmically active) Dbx1-derived neurons for patch-clamp recordings.

In both configurations, we elevated extracellular K⁺ concentration ([K⁺]_o) to 9 mM to increase preBötC excitability (Funk and Greer, 2013). Inspiratory-related motor output

was recorded from the hypoglossal (XII) nerve rootlets, which are captured in transverse slices along with the XII motoneurons and their axon projections to the nerve rootlets, using suction electrodes and a differential amplifier. Field potentials were recorded from the preBötC by forming a seal over it with a suction electrode at the slice surface. Amplifier gain was set at 2000 and the band-pass filter was set at 300–1000 Hz. XII and preBötC bursts were full wave rectified and smoothed for display and quantitative analyses of burst events.

We obtained on-cell patch-clamp recordings under visual control. Patch pipettes were fabricated from borosilicate glass (OD: 1.5 mm, ID: 0.86 mm, 4–6 M Ω in bath) and filled with solution containing 150 mM KCl and 10 mM HEPES). We added gramicidin (CAS number 1405-97-6, product G0550000 from Millipore Sigma, Burlington, MA) acutely at the start of the experiment from stock solution (2 mg gramicidin per 1 ml dimethyl sulfoxide) such that the final concentration was 20 μ g/ml. We also added Alexa fluor 568 hydrazide (50 μ M, ThermoFisher Scientific) to the patch solution, which verifies the integrity of the gramicidin perforated patch as GCaMP6f fluorophore is expressed in the soma whereas Alexa 568 is limited to the adjacent pipette. Patch pipettes with a bath resistance of 4–6 M Ω were backfilled first with a drop of gramicidin-free patch solution in order to ensure gramicidin molecules did not interfere with the initial seal to the membrane. After backfilling, 200 μ l of patch solution with gramicidin was added to the pipette. We employed an EPC-10 patch-clamp amplifier exclusively in current-clamp mode (HEKA Instruments, Holliston, MA) because perforated patches cause a large access resistance at the interface between pipette and target neuron, which produces a voltage-divider circuit and precludes accurate voltage clamp.

We acquired and digitized the signals at 4 kHz with a low-pass filter set to 1 kHz using a 16-bit analog-to-digital converter (AD Instruments, Colorado Springs, CO). All recordings were corrected offline for a liquid junction of 3.74 mV (Barry and Lynch, 1991; Neher, 1992). For both field recordings and associated perforated-patch experiments, the glycine receptor antagonist strychnine hydrochloride (CAS number 1421-86-9, product S8753, Millipore Sigma) and the GABA_A receptor antagonist picrotoxin (CAS number 124-87-8, product P1675, Millipore Sigma) were bath-applied at 5 μ M.

All gramicidin perforated-patch experiments began no earlier than 30 minutes after achieving a seal on the plasma membrane exceeding 1 G Ω (i.e., gigaohm seal), which was sufficient for gramicidin to form ionophores and thus allow intracellular access and current-clamp recording. After we observed a stable recording configuration for 10 minutes, which we considered the control conditions for subsequent analysis, then we applied strychnine and picrotoxin.

When locally applying GABA_A and glycine receptor agonists (muscimol and glycine) onto patch-recorded neurons, we fabricated similar pipettes (as described above) from which to eject glycine and muscimol (dubbed ‘puffer pipettes’). Puffer pipettes were filled with 150 μ M glycine (CAS number 56-40-6, Millipore Sigma) and 30 μ M muscimol (CAS number 2763-96-4, Millipore Sigma) diluted into aCSF containing 9 mM [K⁺]_o (as described above). 30 minutes after forming a gigaohm seal on the plasma membrane, the puffer pipette was positioned to within 50 μ m of the neuron being recorded. Glycine and muscimol were ejected using 7–9 psi pressure pulses lasting 25–200 ms, which we triggered by TTL commands from the EPC-10 amplifier.

Patch-recorded preBötC neurons were identified as neurons by their ability to discharge

action potentials, recognizable 30 minutes after forming a gigaohm seal. The high impedance of gramicidin patches filters high frequency signals like action potentials, thus spike amplitude peaks below 10 mV while the integrity of the patch is maintained. The developmental genetic origin of neurons patched from wild-type preparations was not specified, thus we refer to these neurons as unspecified. Neurons patched in Dbx1;Ai148 mouse slices, which were rhythmically active in sync with XII motor output, are referred to as Dbx1 neurons. For puffing experiments, we added 1 μ M tetrodotoxin (TTX) to the bath after \gtrsim 30 minutes to prevent spike-driven chemical synaptic transmission and isolate postsynaptic responses to muscimol and glycine. We held preBötC neurons at a range of baseline membrane potentials using bias currents. We measured membrane potential trajectories in response to puffed glycine and muscimol, in which the previous 2 seconds of membrane voltage were used as baseline.

Breathing-related measurements *in vivo*

We measured breathing in unrestrained, adult mice of both sexes ($n = 7$ mice total), using a whole-body plethysmograph (EMKA Technologies, Falls Church, VA) with a balanced flow rate of 1 l/min in normoxia (21% O₂ and 79% N₂). The mice were placed in the sealed chamber with constant air flow 10 minutes prior to data collection during each session for acclimation. We observed the mice during every session. Locomotion (exploring), grooming, and sniffing (with synchronized whisking) entrain and modify breathing so we only analyzed epochs of calm breathing absent orofacial or motor behaviors. A pneumotachograph with access to the chamber containing the mouse, and a reference chamber open to room air, were included in the circuit and connected to a differential pressure transducer (AD Instru-

ments, Colorado Springs, CO., RRID:SCR_017551). The raw data reflect airflow, which was acquired and analyzed in LabChart 8 software (AD Instruments). Airflow was digitally integrated to determine volume changes during breathing and in particular to determine tidal volume (V_T). The pressure transducer was calibrated by injecting 0.2 ml of air into the chamber during each trial. We analyzed continuous 60-minute sessions of plethysmography. Epochs of calm breathing contain eupnea and sighs. Sighs were distinguished by inhaled volume exceeding V_T by $2\text{--}3\times$ (the inspired air during a sigh draws on the inspiratory reserve volume of the lungs, and thus exceeds V_T by definition) and by the presence of a post-sigh apnea, i.e., a pause in breathing 1.3x longer than the average inter-breath interval during eupnea.

Identification and analysis of sigh bursts

We measured burst area and cycle time for each event in preBötC field recordings (Figure 2.7). We distinguished a sigh burst from an inspiratory burst by considering the area of an event in conjunction with the cycle time following that event. Sigh bursts have z-scores (mean/SD) for burst area that almost always exceed 2 (and are most often in the range 4–10) whereas inspiratory bursts have an average z-score of 0 (range 2–2). Sigh bursts are followed by a cycle time as long or longer than $1.3\times$ the average cycle time for all events lumped together. Figures 2.7A and B illustrate these measurements for a typical field recording.

The average inspiratory cycle time (\bar{T}) is computed from the six inspiratory cycles preceding the sigh ($T_{\epsilon_1} T_{\epsilon_6}$). T_Δ is the inspiratory-sigh interval computed as the peak time of the sigh burst minus the peak time of the inspiratory burst. T_σ is the duration of the post-

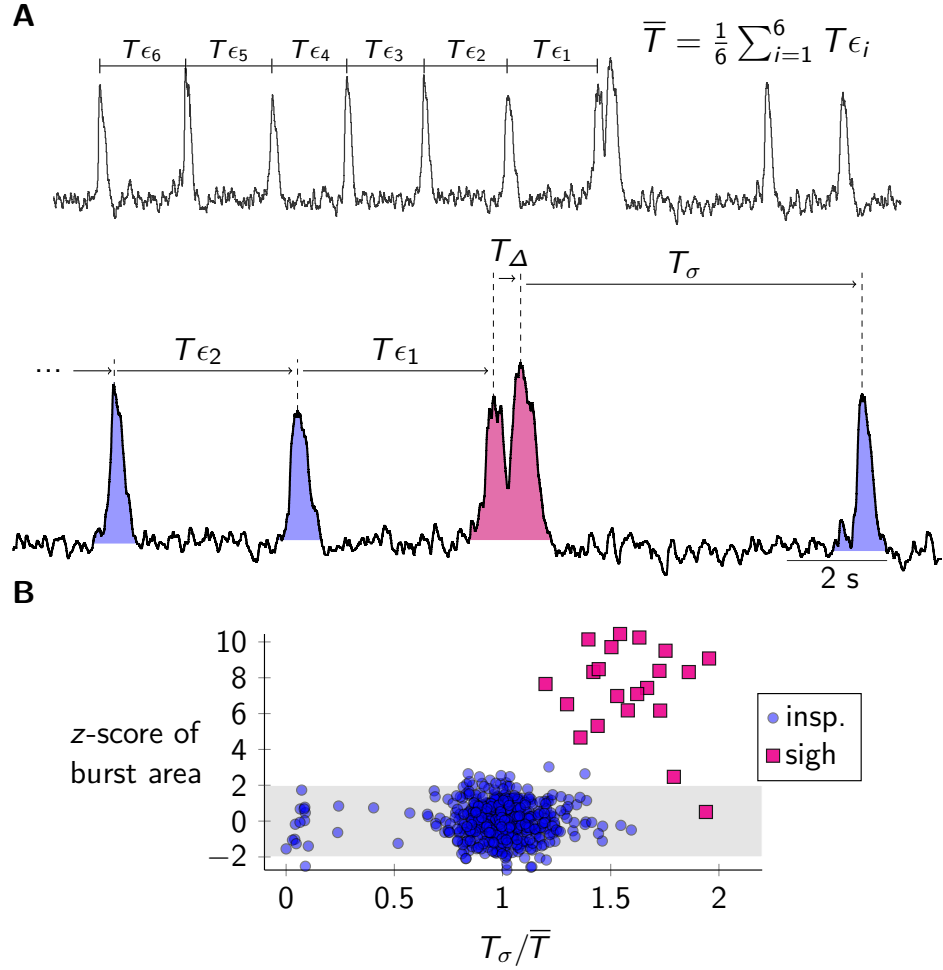


Figure 2.7: A: Field recording of preBötC activity, which includes inspiratory and sigh bursts. Average inspiratory cycle time (\bar{T}) is calculated from six preceding cycle periods ($T_{\epsilon_1} T_{\epsilon_6}$). T_{ϵ} represents period of a single inspiratory cycle; T_{Δ} represents the inspiratory-sigh interval; T_{σ} reflects the duration of the post-sigh apnea. B: A scatter plot showing z-score transformation of burst area plotted against the post-sigh apnea duration, T_{σ} (normalized to the average inspiratory cycle time, \bar{T}). z-score distribution is calculated from all bursts from this slice.

sigh apnea. We normalize T_{Δ} and T_{σ} by \bar{T} in order to minimize the slice-by-slice variation in frequencies.

Measurements and statistics

We analyzed data and computed statistics using LabChart 7 & 8 (AD Instruments), MATLAB 2018b (Mathworks, Natick MA., RRID:SCR_001622), and Igor Pro 8 (Wavemetrics, Oswego, OR., RRID:SCR_000325). We describe the statistical hypothesis tests used as

they appear in the main text.

Chapter 3

The preinspiratory phase of eupnea

**rhythmogenesis requires more than
recurrent excitation**

3.1 Introduction

The cellular and synaptic origins of the inspiratory rhythm that drives eupnea, have been studied since the preBötC was identified as the rhythm's source, 30 years ago (Smith et al., 1991). Most of what we understand comes from studies using rhythmically active slices that provide optimal access to the rhythmogenic neurons for biophysical measurements. Figure 3.1 shows a typical network field recording from the preBötC, with phases of the rhythm demarcated by the primary mechanisms putatively involved in the process, starting from the termination of one inspiratory burst and finishing at the generation of the next burst.

As discussed in Section 1.5, activity in the preBötC builds via recurrent excitation

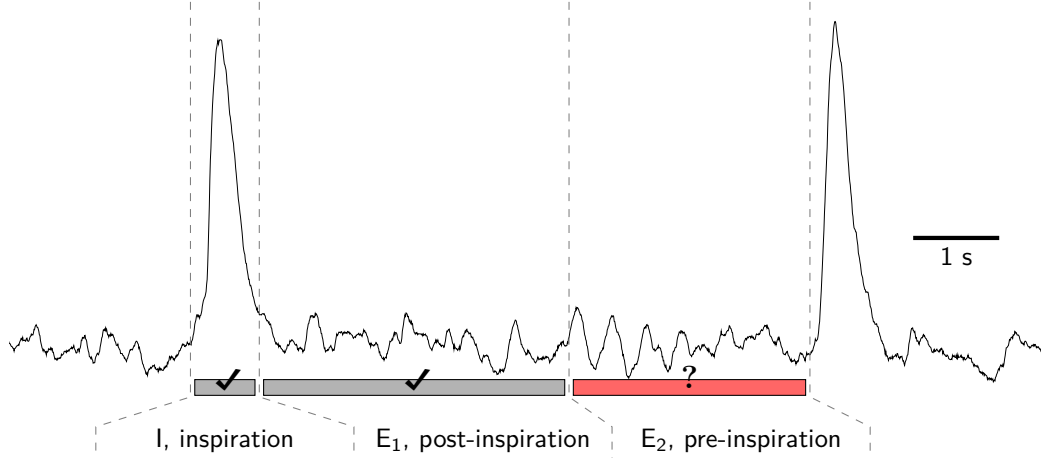


Figure 3.1: Representative trace of the inspiratory rhythm recorded as via local field potential in the preBötC. Dashed lines demarcate the phases of one inspiratory cycle, separated by primary mechanism. Grey bars and check marks underneath the trace represent phases whose mechanisms are well known. The red bar with a question mark, denoted as E₂, the preinspiratory phase, is the primary focus of this section.

and groups of neurons become active together. This phenomenon is known as a burstlet. If the entire network joins in the burstlet, and pattern-forming currents such as I_{CAN} are recruited to bolster excitability, the event becomes a *bona fide* inspiratory burst. Regardless of whether the event reaches burst status, or remains a burstlet, this inspiratory phase of the cycle ends via synaptic depression (Guerrier et al., 2015; Kottick and Del Negro, 2015) and the recruitment of activity-dependent outward currents (Del Negro et al., 2009; Krey et al., 2010).

The system recovers from the burst-terminating mechanisms on the time course of 2 seconds (Baertsch et al., 2018; Kottick and Del Negro, 2015). This second phase of the respiratory cycle is called E₁, or postinspiration. A subsequent inspiratory burst cannot be generated during this time, even by exciting the core rhythmogenic neurons. Work done *in vivo* has also shown stimulating the preBötC soon after the inspiratory phase does not decrease the time to the next inspiration (Alsahafi et al., 2015; Cui et al., 2016; Vann et al., 2018). There is some window of recovery, wherein after this refractory period, another full-

sized inspiratory burst can occur spontaneously or it may be evoked. The system is no longer recovering; it is ready and able to generate another burst. This Chapter is concerned with the possible cellular and synaptic mechanisms that set the duration of this preinspiratory phase.

While the cellular and synaptic mechanisms that underlie inspiratory burst generation, termination, and recovery are well known, the period of time between recovery from the burst event (postinspiration) and the start of the next burst (inspiration) is still a mystery. Two observations for the preinspiratory phase frame our modeling choices and lead to insights into mechanisms underlying inspiratory rhythmogenesis. First, there is no correlation between the duration of the inter-event interval and the amplitude of the subsequent inspiratory burst. This suggests that whatever mechanism sets the timing for the next burst event, it has no impact on the burst generation per se. Thus, the mechanisms responsible for terminating the burst, and setting the recovery window, i.e., synaptic depression and activity-dependent outward currents, do not directly influence the duration of the preinspiratory phase, and thus cannot influence the cycle period. These processes must have recovered completely before the next burst, and then, presumably, a different cellular mechanism determines the preinspiratory timing phase.

This leads directly to the second observation: that the mechanism that determines the time until the next inspiratory burst is time-dependent. That is, it cannot be the integration of random excitatory post-synaptic potentials (EPSPs), or random network communication that leads to the burst event. If the neuron was waiting for a random event that has some probability of occurring per unit time, the time between successive events is expected to be exponentially distributed. However, it is well-known that the time between events in the

inspiratory rhythm, both *in vivo* and *in vitro*, is not exponentially distributed. Therefore, it stands to reason that the mechanism that determines the time between system recovery and the start of the next burst must be time-dependent. Burst events must become more likely as the time elapsed since the previous burst increases.

To further explore the implications of these two observations, and to verify these principles more rigorously, we developed several mathematical models of the inspiratory rhythm.

3.2 Activity models of episodic bursting

We constructed an activity-based model of inspiratory rhythm generation in order to study the mechanisms that drove the inspiratory system. This work is a collaboration between my advisors Gregory D. Conradi Smith and Christopher A. Del Negro, as well as my colleague Cameron Grover.

The inspiratory system model follows the work of Tabak, Rinzel, and O'Donovan (Tabak et al., 2000a, 2001a). As reviewed in (Tabak and Rinzel, 2005a), a minimal yet realistic approach to modeling spontaneous episodic activity in developing spinal cord networks begins with an ODE for the network firing rate that takes the form $\tau_a da/dt = a_\infty(w \cdot s \cdot d \cdot a) - a$ where s and d represent synaptic depression operating on slow and fast time scales, respectively, and the parameter w represents synaptic gain. In the Tabak-Rinzel model, fast synaptic depression, d , leads to oscillatory dynamics during the active phase of each burst. Because this fast oscillatory activity does not occur in our system, a reasonable starting point for an activity model of episodic bursting of the preBötC is the following two-variable dynamical

system,

$$\tau_a \frac{da}{dt} = a_\infty(w \cdot s \cdot a) - a \quad (3.1)$$

$$\tau_s \frac{ds}{dt} = s_\infty(a) - s, \quad (3.2)$$

where a is the network activity and s accounts for the dynamics of synaptic depression ($s = 1$ indicates the absence of depression, while $s = 0$ corresponds to full depression). In Equations 3.1-3.2, the functions a_∞ and s_∞ are increasing sigmoids,

$$a_\infty(x) = \frac{1}{1 + e^{4(\theta_a - x)/k_a}} \quad (3.3)$$

$$s_\infty(x) = \frac{1}{1 + e^{4(\theta_s - x)/k_s}}. \quad (3.4)$$

Because k_a is positive, a_∞ is a monotone increasing function of x , which in Equation 3.1 is the aggregate synaptic drive, calculated as the triple product $w \cdot s \cdot a$ (the standard value for the synaptic gain is $w = 1$, see Table 3.1). Conversely, k_s is negative and s_∞ is monotone decreasing function of the network activity (a). The 4 that appears in Equations 4.6–4.7 makes k_a and k_s the inverse of the slope of a_∞ and s_∞ at their respective half-maxima. At steady state, the network activity (a) solves the algebraic equation,

$$\bar{a} = a_\infty(w \cdot \bar{s} \cdot \bar{a}). \quad (3.5)$$

Using the default value for the gain of recurrent excitation ($w = 1$), Figure 3.2 shows that the network activity can have 1–3 steady states (solutions of Equation 3.5) depending on the state of synaptic depression (s). For intermediate values of s , the excitatory network is

bistable; there are two stable steady states separated by one unstable steady state.

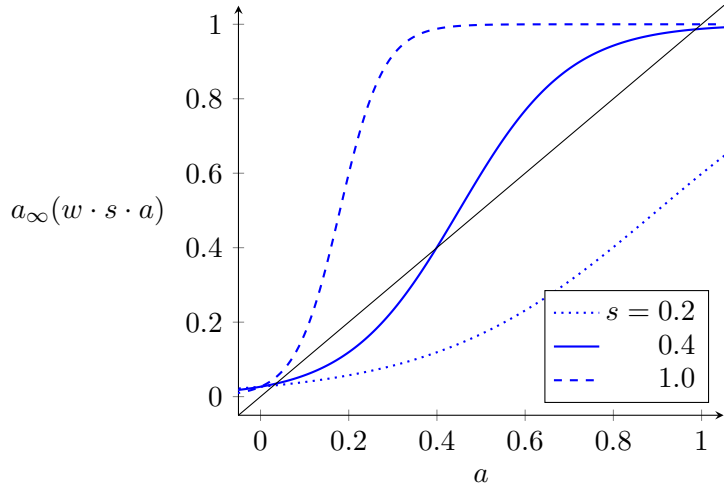


Figure 3.2: For intermediate values of the synaptic depression variable (s), the recurrent excitatory network is bistable, as indicated by the three intersections of steady state activity a_∞ (solid blue curve) and the 45 degree line (black). The synaptic depression variable takes values between 0 (complete depression) and 1 (no depression). Parameters: $w = 1$, $\theta_a = 0.18$, $k_a = 0.2$.

3.2.1 Dynamics of synaptic depression

Figure 3.3 shows representative phase planes that illustrate how the two-variable model (Equation 3.2) may exhibit episodic network activity. The blue curve shows the s nullcline, which is given by points in the (s, a) -plane for which $ds/dt = 0$,

$$s \text{ nullcline: } s = s_\infty(a), \quad (3.6)$$

with s_∞ given by Equation 4.7. The a nullcline ($da/dt = 0$) is given by the implicit expression $a = a_\infty(w \cdot s \cdot a)$, which is equivalent to the explicit expression

$$a \text{ nullcline: } s = \frac{4\theta_a - k_a \ln [(1-a)/a]}{4wa}. \quad (3.7)$$

Figure 3.3 shows that the two-variable Tabak-Rinzel-like activity model of the preBötC may exhibit two distinct forms of excitability and/or oscillations (namely, type 1 and type 2) depending on the parameters used; for review see Rinzel and Ermentrout (1998). Figure 3.3A shows the nullclines that give rise to type 2 oscillations; Figure 3.3B shows nullclines associated with type 1 excitability. The bifurcation diagram of Figure 3.3C show oscillations emerging via a Hopf bifurcation (type 2). The bifurcation diagram of Figure 3.3D show oscillations that arise from a saddle-node on an invariant circle bifurcation (type 1).

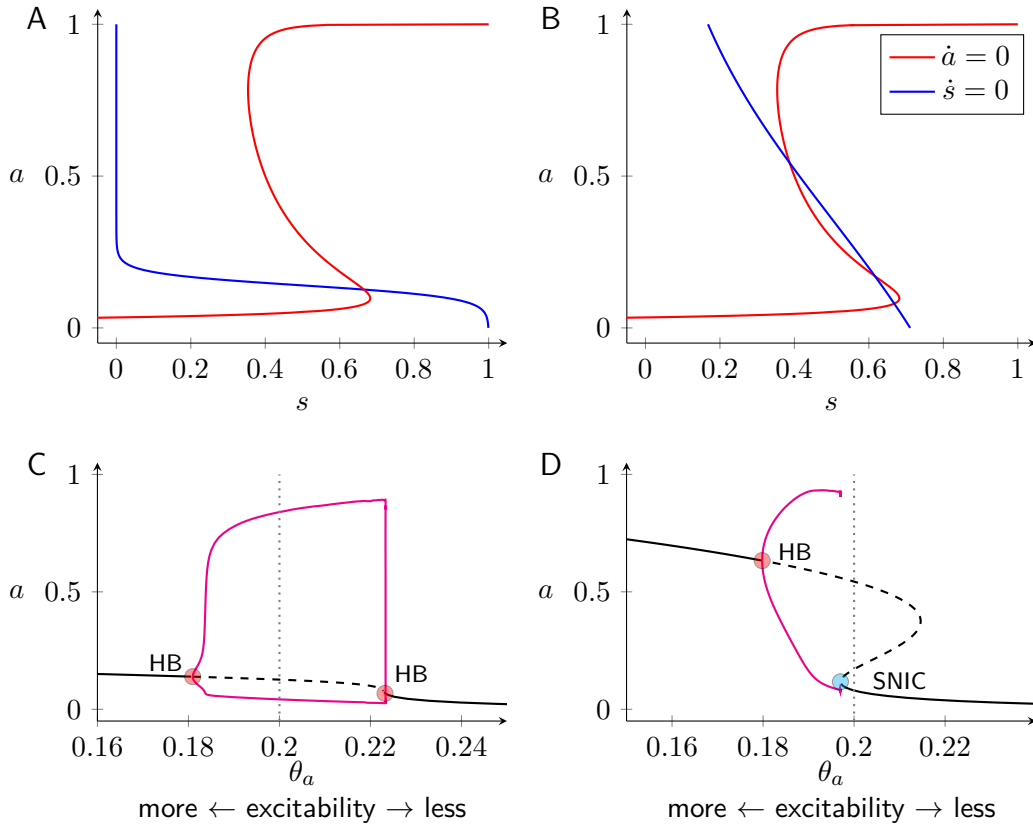


Figure 3.3: Phase plane, nullclines and bifurcation diagrams for the two-variable Tabak-Rinzel-type model of episodic network activity (Equations 3.6-3.7). A, type 2 oscillations; $\theta_s = 0.14$, $k_s = -0.08$. B, type 1 excitability; $\theta_s = 0.3$, $k_s = -1.0$. Other parameters: $w = 1$, $\tau_a = 10$, $\theta_a = 0.2$, $k_a = 0.2$. HB: Hopf bifurcation; SNIC: Saddle-node on an invariant circle bifurcation. C and D, bifurcation diagrams show emergence of oscillations as the cellular adaptation half-maximum (θ_a) is varied (lesser values of θ_a lead to greater excitability, see Equation 4.6). Solid black lines represent s steady states. Dashed black lines represent unstable steady states. Magenta lines represent limit cycle oscillations.

3.2.2 Inspiratory dynamics with two variables (one fast and one slow)

How well does the two variable minimal model (Equations 3.1-4.7) of the inspiratory rhythm emulate *in vitro* preBötC recordings? Figure 3.4A (left) shows a representative *in vitro* network field recording of preBötC electrical activity. The scatter plot and histogram (right panel) illustrate two salient empirical characteristics of this rhythm. (1) The size of a burst event has little relationship to the duration of the preceding interval ($r^2 = 0.01$). (2) The distribution of inter-burst intervals is bell-shaped ($\mu = 5.4 \text{ s}$, $\sigma = 2.0 \text{ s}$).

Figure 3.4B shows trajectories of episodic activity (a) and synaptic depression (s) for the two-variable inspiratory model with parameters leading to type 2 excitability. For realism, additive Gaussian white noise, $\hat{\xi}(t)$, has been introduced to Equation 3.1, as follows:

$$\tau_a \frac{da}{dt} = a_\infty(w \cdot s \cdot a) - a + \hat{\xi}(t) \quad (3.8)$$

$$\tau_s \frac{ds}{dt} = s_\infty(a) - s. \quad (3.9)$$

The noise term, $\hat{\xi}(t)$, is a rapidly fluctuating function of time with mean zero, $\langle \hat{\xi}(t) \rangle = 0$ and variance that depends on system state (see Section 3.6). In the type 2 parameter regime, the two-variable inspiratory model exhibits stochastic oscillations with inter-burst intervals distributed in a bell-shaped manner that is consistent with experiment (Figure 3.4B histogram, $\mu = 4.1 \text{ s}$, $\sigma = 0.21 \text{ s}$). However, this episodic activity exhibits an unrealistic positive correlation between preceding interval and burst size (scatter plot, $r^2 = 0.21$). This correlation is a consequence of fluctuations in network activity that are visible at the bottom knee of the a nullcline in the corresponding phase plane. The system in this configuration

Table 3.1: Standard parameters for inspiratory model (dimensionless).

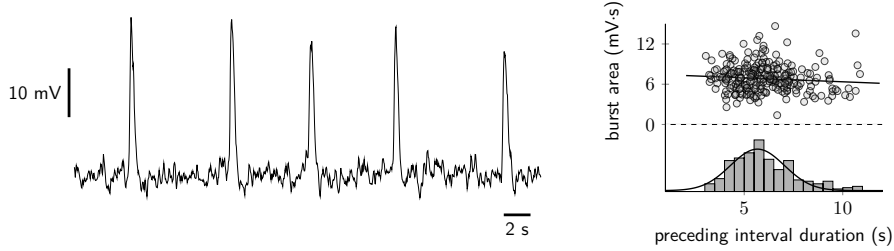
Symbol	Definition	Value
w	network connectivity	1
θ_a	average firing threshold (half activation)	-0.3
k_a	reciprocal of slope of a_∞ at half activation	0.2
τ_a	network recruitment time constant	0.15
θ_s	half activation of s	0.14
k_s	reciprocal of slope of s_∞ at half activation	-0.08
τ_s	time constant of synaptic depression	0.75
θ_θ	half activation of θ	0.15
k_θ	reciprocal of slope of θ_∞ at half activation	0.2
τ_θ^{\max}	maximum of time constant of cellular adaptation	6
τ_θ^{\min}	minimum of time constant of cellular adaptation	0.15
θ_{τ_θ}	half max of $\tau_\theta(a)$	0.3
k_{τ_θ}	reciprocal of slope of $\tau_\theta(a)$ at half activation	-0.5

is intrinsically oscillatory, but noise impacts when the system will fall off the bottom right knee of the activity nullcline. Variation in the level of synaptic depression when bursts are initiated leads to variable inter-burst intervals Tabak et al. (2006).

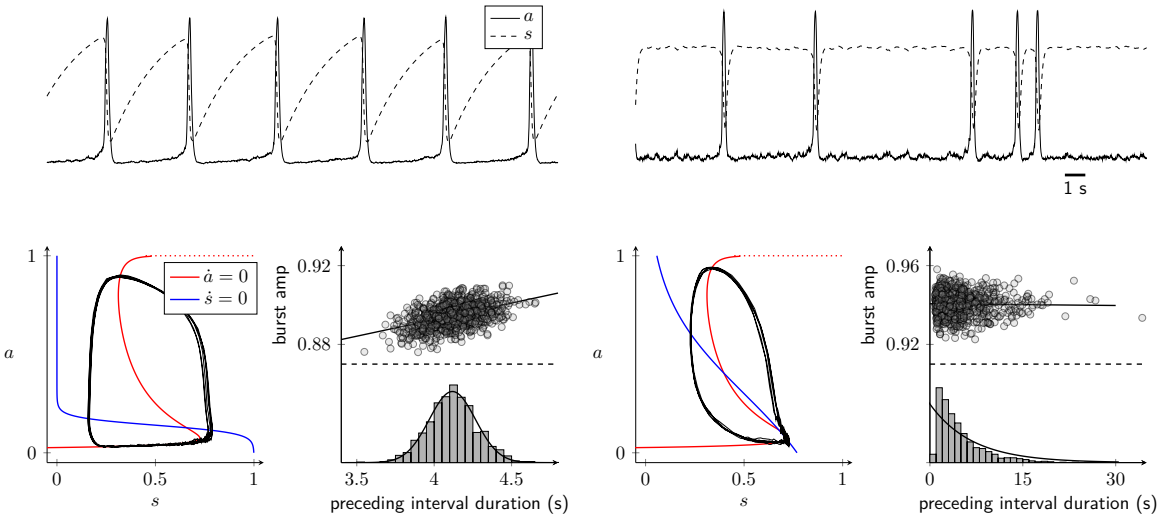
For comparison, Figure 3.4C shows simulations of the two-variable inspiratory model with parameters leading to type 1 excitability and rhythms that occur stochastically when noise is present in the system.. In this parameter regime, the system is subcritical to a saddle-node on an invariant circle (SNIC) bifurcation. Because synaptic depression recovers to the same value before the onset of each network burst, the burst amplitudes are uncorrelated with the duration of preceding inter-event intervals ($r^2 < 0.01$). However, because bursts do not occur unless triggered by sufficiently large fluctuations (rare events), the inter-burst intervals are distributed in an exponential fashion ($\mu = 6.8 \text{ s}$), albeit shifted by the amount of time required for recovery of synaptic depression. Because this inter-burst interval distribution is inconsistent with *in vitro* (Figure 3.4A) experimental observations, type 1 stochastic excitability is an unrealistic starting point for our activity model of episodic

bursting in the preBötC.

A *in vitro*



B simulation - type 2 excitability



C simulation - type 1 excitability

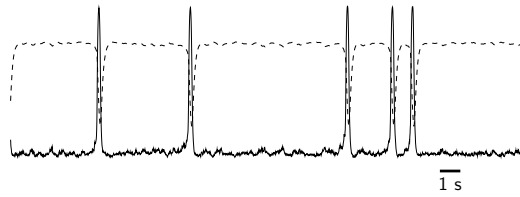


Figure 3.4: Limitations of the two-variable inspiratory model. A, network recording of preBötC activity. Right: Scatter plot of the relationship between burst size (area) and the duration of the preceding inter-burst interval. The histogram shows the distribution of inter-event intervals. B, simulations using the two-variable model with parameters giving type 2 stochastic oscillations. C, simulations using the two variable model with parameters leading to type 1 stochastic excitability.

In summary, the simulations of Figure 3.4 show that the two-variable model of inspiratory dynamics is unrealistic in the following sense. If parameters are chosen for type 2 oscillations, the inter-burst intervals are distributed in a realistic manner, but the positive correlation between the burst amplitude and the duration of the preceding interval is inconsistent with experiment. Conversely, if parameters are chosen for type-1 excitability with oscillations driven stochastically, there is no correlation between burst amplitude and the duration of the preceding interval (consistent with experiment). But in this case the distri-

bution of the inter-event intervals exhibited by the model is unrealistic (more variable than observed in experiment).

3.2.3 Inspiratory dynamics with three variables (one fast and two slow)

The model development and analysis of the previous section suggests that the mechanism(s) that determines the inter-burst interval in the preBötC is distinct from the synaptic depression mechanism that is responsible for burst termination. For this reason, our proffered activity model of the inspiratory subsystem includes a second slow variable, θ , representing activity-dependent cellular adaptation. This three-variable model includes the following ODEs,

$$\tau_a \frac{da}{dt} = a_\infty(w \cdot s \cdot a - \theta) - a + \hat{\xi}(t) \quad (3.10)$$

$$\tau_s \frac{ds}{dt} = s_\infty(a) - s \quad (3.11)$$

$$\tau_\theta(a) \frac{d\theta}{dt} = \theta_\infty(a) - \theta, \quad (3.12)$$

with a_∞ and s_∞ given by Equations 4.6-4.7. The steady-state level of cellular adaptation given by

$$\theta_\infty(a) = \frac{1}{1 + e^{4(\theta_\theta - a)/k_\theta}}, \quad (3.13)$$

is an increasing function of network activity ($k_\theta > 0$). The time constant for cellular adaptation, τ_θ , is chosen to be the following function of network activity,

$$\tau_\theta(a) = \frac{\tau_\theta^{\max} - \tau_\theta^{\min}}{1 + e^{4(\theta_\theta - a)/k_{\tau_\theta}}} + \tau_\theta^{\min}. \quad (3.14)$$

In this expression, parameters are chosen to ensure that cellular adaptation accumulates rapidly in the active phase (large a), but recovers slowly during the silent phase when network activity is low (Table 3.1). Figure 3.5A shows a representative simulation of the three-variable inspiratory model exhibiting episodic bursting. In this three-variable model, synaptic depression terminates the bursts, but burst onset is determined by the recovery of cellular adaptation (θ must be sufficiently small). These modeling assumptions are consistent with the experimentally observed normal distribution of inter-burst intervals and lack of correlation between inspiratory burst and preceding interval (compare Figure 3.5D and E). In particular, (1) the inter-burst interval distribution is normally distributed with realistic mean and variance ($\mu = 4.3\text{ s}$, $\sigma = 0.044\text{ s}$), and (2) there is no correlation between burst amplitude and the duration of the preceding inter-burst interval ($r^2 < 0.01$).

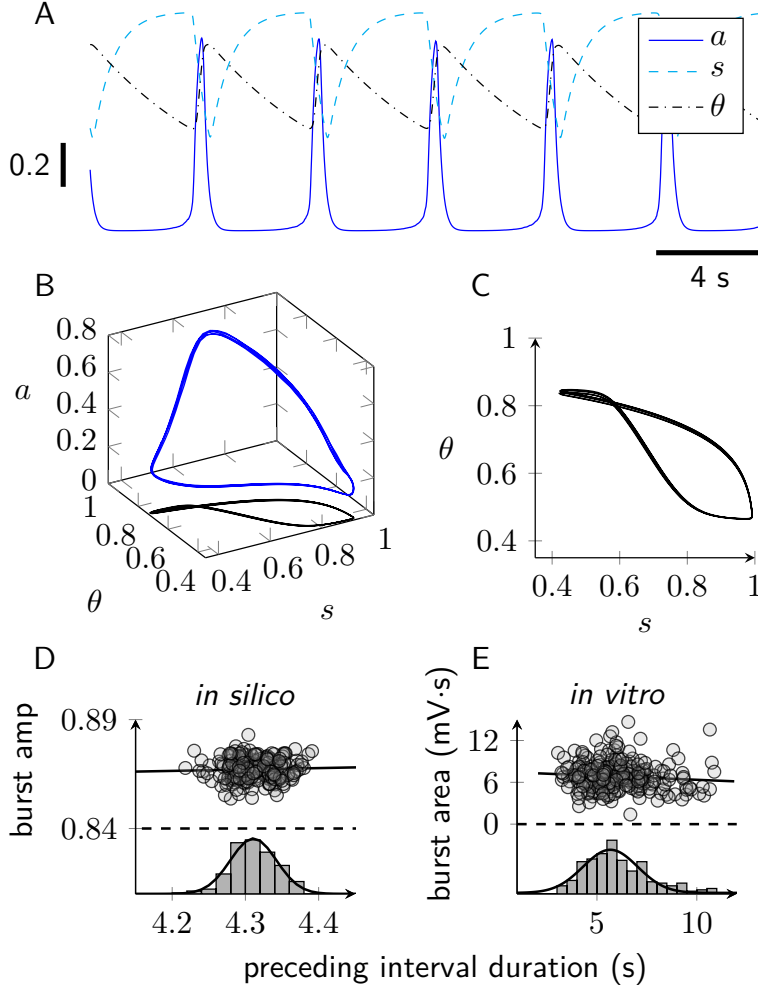


Figure 3.5: Three-variable model of episodic network activity gives realistic inspiratory dynamics (see Equations 3.10-3.12). A, representative trajectory of the three-state model showing network activity (a) and the dynamics of two slow variables: synaptic depression (s) and cellular adaptation (θ). B, trajectory in 3d phase space (blue curve, left) with projection emphasizing the relationship between synaptic depression and cellular adaption (s and θ , black curve, right). C, comparison of burst amplitude and inter-burst interval duration according to the model (*in silico*) and experiment (*in vitro*, reproduced from Figure 3.4A).

3.2.4 Takeaways from the activity-based model for inspiratory rhythmogenesis

The activity-based model for inspiratory rhythmogenesis revealed a required mechanism that does not impact the size of the burst event, and is time dependent. In the model, we include the parameter θ , which we refer to as cellular adaptation, to achieve this property.

However, a direct biological equivalence for this state variable is unclear.

Two possible mechanisms come to mind that may act as the required time-dependent dynamic thresholds for network activation, that sets the time of the subsequent inspiratory burst. One possibility is that the depolarization-activated potassium current, I_A , acts as a clamp on excitability in the network, specifically in the dendrites of the preBötC interneurons. It is well known that preBötC neurons express I_A (Phillips et al., 2018) and that I_A influences rhythm generation (Hayes et al., 2008). I_A might act as a gate against the initial build of activity, as suggested by Hayes et al. (2008). As the burst-terminating mechanisms recover from the preceding burst (E_1 postinspiration, Figure 3.1), neurons begin to fire action potentials and communicate again. If there were no shunt on the network, recurrent activity would quickly build and lead to a network-wide burst within several hundred milliseconds. However, I_A , localized in the dendrites of the preBötC neurons, counteracts spurious EP-SPs and keeps excitability down. It is only once activity, and the rate of EPSPs, has built up enough (and perhaps synchronized) to inactivate I_A , then the outward current from I_A diminishes, and a more rapid, and nonlinear, build up of network activity occurs.

A second possibility is that the network topology prolongs the build up of recurrent excitation, from several hundred milliseconds to several seconds. Changes in network inter-connectivity may impact the rate of activity propagation. A sparsely coupled network of excitatory neurons might be more suitable for generating localized bursts of activity, without activating the entire network at once. Conversely, a highly connected network, where the connection from any neuron to another in the network is only two or three synapses away, would be unable to localize excitability for long, because activity would spread across the entire network with only two or three synaptic connections. Addressing this possibility

necessitates a different modeling approach that is described in the following section.

3.3 Studying recurrent excitation in a network of coupled oscillators

To study how a *bona fide* network of neurons oscillate together via recurrent excitation and synaptic inhibition (as apposed to the minimal activity model of Section 3.2), we us the formulation of pulse-coupled oscillators. This type of model consists of N neurons that each oscillate with some arbitrarily defined frequency. Here, ‘oscillation’ refers to the cycle of generating one action potential (spike). It can be helpful to think of each neuron as a clock with one hand. Every time the hand passes 12 o’clock the neuron completes a cycle and generates one action potential, and sends a pulse its downstream neurons, incriminating their phase’s. This is unlike excitatory synaptic drive in the sense that the pulse is instantaneous and lasts for zero duration, but which decreases the time until those neurons complete their own cycle. The neurons are connected in a directed network.

Consider a network of N neurons, where the phase of a given neuron, θ_i is given by

$$\dot{\theta}_i = 1 - \cos \theta_i + [1 + \cos \theta_i] I_i, \quad (3.15)$$

where I_i determines the characteristic frequency of the i th node. See Figure 3.6 for a phase diagram of Equation 3.15 with different values of I_i . When I_i is positive, θ_i will increase until $\theta > \pi$. At this point, the node fires a signal to downstream neighbors, and starts the cycle over at $\theta = -\pi$. When I_i is negative, the system settles to a stable steady state. A kick of

sufficient magnitude, large enough to increase θ_i beyond the one unstable steady state, will cause the system to complete one full cycle before returning to the stable steady state.

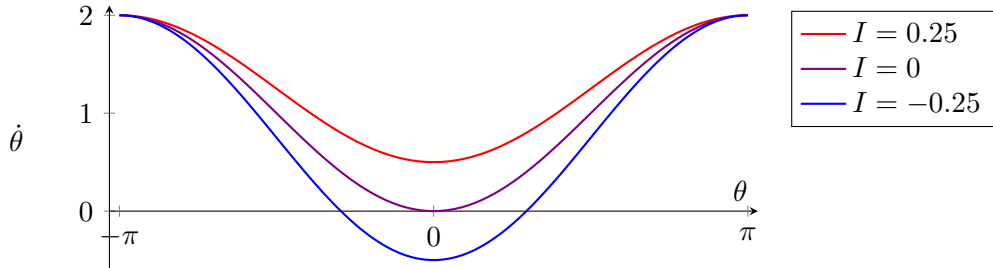


Figure 3.6: Phase diagram for $\dot{\theta}$, a representative neuronal oscillator (Equation 3.15) for different values of I , the intrinsic frequency. For positive values of I , there are no steady states and θ increases until $\theta > \pi$. At $I = 0$, there is a fold bifurcation, which creates a stable steady state when $I < 0$.

The particular form of Equation 3.15 is used because it replicates the dynamics of a saddle-node on an invariant circle (SNIC) bifurcation, but with only one state variable. The dynamics of this so called θ neuron are type-1, i.e., the frequency of the oscillations can be made arbitrarily slow.

A network of excitatory pulse-coupled oscillators with positive and identical intrinsic frequency will synchronize given enough time (Canavier and Achuthan, 2010; Strogatz and Stewart, 1993). However, each will spike only once during a network-wide burst; the nodes will be quiescent until the next collective spike. To produce a more realistic train of spikes during a network-wide oscillation, we include a synaptic conductance component for each node. Now, rather than giving a downstream neuron a single kick of activity after a spike, the neuron provides a transient excitation to its downstream neighbors, similar to a neuron receiving an EPSP.

To achieve this effect, we include one additional state variable for each neuron. s_i measures the synaptic conductance that neuron i provides to its downstream neighbors. By default, synaptic conductance decays away with some time constant (s_τ), thus the ODE for

s_i has the form,

$$\dot{s}_i = -s_i/s_\tau. \quad (3.16)$$

Whenever neuron i completes one oscillation, or one cycle, it “fires” and steps up its synaptic conductance by an amount proportional to s_{gain} ,

$$s_i(t+1) = s_i(t) + s_{\text{gain}}(1 - s_i(t)). \quad (3.17)$$

So after a spike, a neuron sends an “EPSP” to its downstream neighbors that decays away with rate s_τ .

Without a shunt on excitation, and with sufficient synaptic gain, activity in the network would quickly build until all the neurons were oscillating as some maximal rate (Figure 3.7). Therefore, we introduce synaptic depression, which acts on a slower timescale than recurrent excitation, and is biologically consistent with properties our constituent preBötC neurons are known to express. Synaptic depression introduced two state variables into the system. m , similar to s , decays away at a constant rate m_τ . After every cycle, a neuron “fires” and m increases by an amount proportional to m_{gain} . Tracking slightly behind this variable m , is n which increases in a time-dependent manner proportional to m , and decays at a rate of n_τ . This can be written

$$\dot{m}_i = -m_i/m_\tau \quad (3.18)$$

$$\dot{n}_i = \alpha_n m_i(1 - n_i) - n_i/n_\tau \quad (3.19)$$

where on the time step after a spike,

$$m_i(t+1) = m_i(t) + m_{\text{gain}}(1 - m_i(t)). \quad (3.20)$$

The state variable n is akin to vesicle depletion. Synaptic depression, y , is computed as $y = 1 - n$. When $y = 1$ synaptic depression is essentially off, and when $y = 0$ the synapse has no vesicles remaining and the synapse is completely depressed. The product of synaptic conductance and synaptic depression determines the magnitude of synaptic drive a neuron sends to all the neurons to which it projects. At each time step, the amount of external drive that neuron i receives is summated with the neuron's intrinsic frequency. Thus,

$$I_i = I_0 + d \sum_j s_j y_j \quad (3.21)$$

where I_0 is the intrinsic frequency of neuron i (this can be the same for every neuron, or pulled from a distribution). d is the strength or gain of the synaptic connection, a scalar. s_j is the synaptic conductance of the presynaptic neuron j to neuron i . y_j is the synaptic depression for the presynaptic neurons j from neuron i . Thus, Equation 3.21 reads: The external current a neuron i receives at any time step is equal to an intrinsic current (I_0), plus the strength of all upstream neuron synapses (a product of their synaptic conductance (s_j) and recovery from synaptic depression (y_j)). This fast-slow subsystem generates oscillations in the network through recurrent excitation and synaptic inhibition (Figure 3.7).

The neurons in this simulation (Figure 3.7) are wired together based on an Erdős-Rényi random (ERR) graph connectivity scheme (Erdős et al., 1960; Newman, 2010; Prettejohn et al., 2011). In an ERR graph, any two nodes (neurons) have a probability, ρ , of being

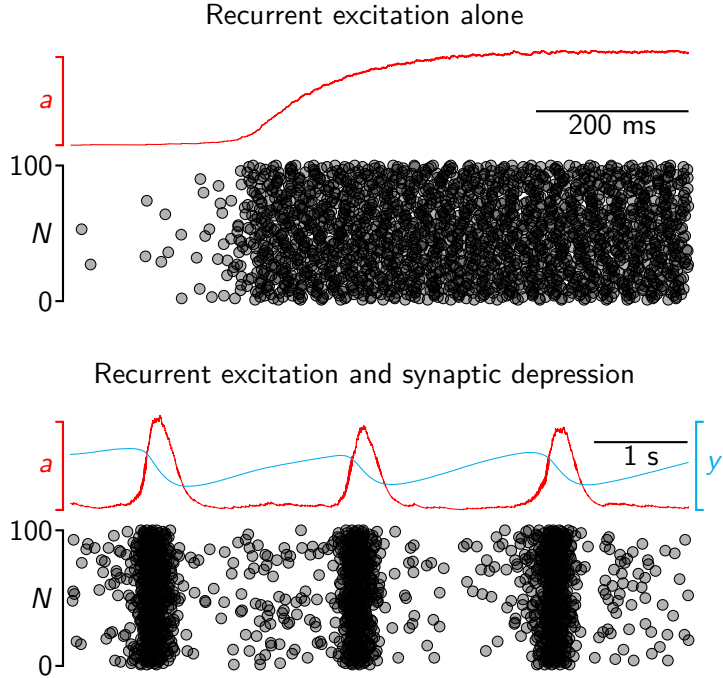


Figure 3.7: Simulation of coupled oscillators in a random network. Top: Simulation with only recurrent excitation. The red trace shows average activity in the network, below is a raster plot, where each black dot marks the time where that neuron spiked. Below: Simulation with recurrent excitation and synaptic depression. Red shows average activity in the network, and blue shows the average synaptic depression. Below is a raster plot, where each black dot marks the time where that neuron spiked. Parameters for the bottom simulation can be found in Table 3.2. Parameters for the top simulation are the same as Table 3.2, but $m_{\text{gain}} = 0$.

connected. Intrinsic firing rates were drawn from a distribution with mean I_μ and standard deviation I_σ . See Table 3.2 for the parameters used.

An important characteristic of this network and the associated network oscillation is that a different collection of neurons can initiate the burst on any cycle. This echos the biology, where a preBötC neuron may lead an inspiratory burst on one cycle but spike only on the network burst in another instance. Now that we have a functioning model of a network of neurons generating oscillations through recurrent excitation and synaptic inhibition, we can use the model to ask questions about how activity builds up in the network.

The first observation from analyzing this model is activity builds rapidly in the network. See the top panel of Figure 3.7. With realistic time constants for synaptic conductance and

Table 3.2: Standard parameters for network model.

Symbol	Definition	Value
N	number of neurons	100
d	synaptic gain	0.03
I_μ	mean intrinsic frequency	-9×10^{-4}
I_σ	standard deviation of intrinsic frequency	1×10^{-7}
m_{gain}	discrete step for synaptic depression term m	0.2
τ_m	time constant for synaptic depression term m	300 ms
α_n	rise parameter for n	0.011
τ_n	time constant for synaptic depression term n	1300 ms
s_{gain}	discrete step for synaptic conductance term s	1
τ_s	time constant for synaptic conductance term s	15 ms
ρ	probability of connection (for ERR network)	0.1

synaptic depression, activity builds in the network in roughly 200-300 milliseconds. This time course for network activity buildup matches with the depolarization ramp seen in preBötC type-1 neurons at the onset of an inspiratory burst, as discussed in Chapter 1, as well as in Gray (1999); Picardo et al. (2013); Rekling et al. (1996). However, the time course for this recurrent excitation does not account for time period between the recovery of burst-terminating mechanisms and the generation of the burst, what is known as the preinspiration phase (Figure 3.1). My question thus remains, what time-dependent process is responsible for determining when the inspiratory burst occurs.

We propose that network topology, the way the network of neurons is wired together, prolongs the build up of activity from a few hundred milliseconds to 2 or 3 seconds.

3.3.1 The network-based model can be configured for type-1 and type-2 excitability

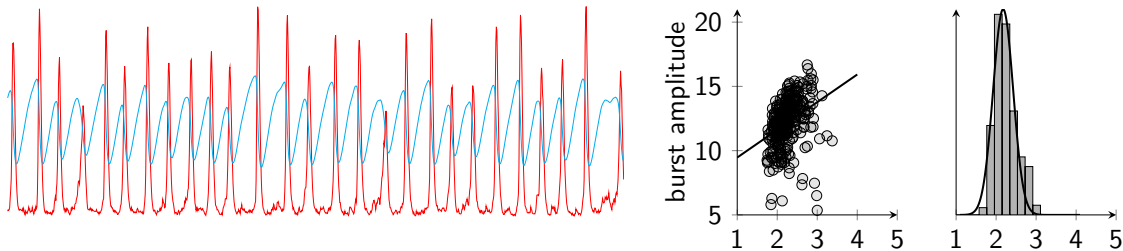
A careful observer might notice a connection between the configuration of this model's rhythmicity and that of the activity based model described in Section 3.2. In this parameter

space, recurrent excitation overcomes decreasing synaptic depression and triggers a burst event. This is reminiscent of the oscillations observed in the type-2 configuration of the activity-based model. Since, in this regime, synaptic depression is not allowed to recover completely before the next burst, we can predict from our previous work that there should be a positive correlation between the preceding interval and the magnitude of the burst (Figure 3.8). Indeed, while the relationship is not as strong as in the activity-based model, there is still a noticeable correlation between preceding interval and the amplitude of the following burst. Furthermore, the inter-event intervals between burst events is normally distributed, as predicted from the activity-based model.

Therefore, to test if we would observe a similar phenomenon in a network-based model, we configured the network-based model to mimic the type-1 excitable system we observed in the activity-based model. Indeed, we were able to achieve something similar. Now, synaptic depression is allowed to recover before a burst can occur, and the network needs to wait for enough random activity to initiate the next burst. The distribution of inter-event intervals is noticeably more exponential, and the size of the bursts is less correlated with preceding interval duration.

While the statistics concerning the correlation between inter-event interval and burst size, as well as those for the distribution of inter-event intervals, are not as strong as in the activity-based model, it is still surprising we see this phenomenon in a model of individual units. After all, remember that the actual “activity” is not a state variable of the model. It’s a calculation of the spikes per neuron per second. Similarly, mean synaptic depression is not exactly consistent across the network, and closer to a distribution for different neurons. It is interesting, and reassuring, that we could replicate our finding from the activity-based model

Recurrent excitation and synaptic depression (type 2)



Recurrent excitation and synaptic depression (type 1)

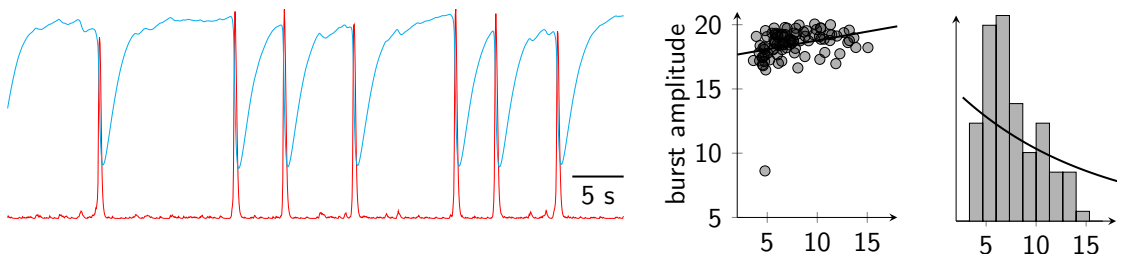


Figure 3.8: Simulation of network-model in two configurations. Top: Activity (red trace) escapes from the recovering synaptic depression (blue trace). Middle scatter plot shows burst amplitude versus preceding interval duration. Each mark is one burst cycle. The black line is a regression fit to a line. Right histogram shows the distribution of all inter-event intervals (i.e.i.) in the simulation. Here the black line is a regression fit to a gaussian. Total Simulation time is 720 seconds. Parameters are as in Table 3.2. Bottom: Synaptic depression (blue trace) fully recovers before noise kicks the network activity (red trace) into a burst. Middle scatter plot shows burst amplitude versus preceding interval duration. Each mark is one burst cycle. The black line is a regression fit to a line. Right histogram shows the distribution of all inter-event intervals (i.e.i.) in the simulation. Here the black line is a regression fit to an exponential function. Total Simulation time is 720 seconds. Parameters are the same as above, except $I_\mu = -1.18 \times 10^{-3}$.

with the network-based model, and further validates our conclusions: in order to construct an accurate model of the inspiratory rhythm (i.e., a system that has normally distributed inter-event intervals and no correlation between burst size and preceding interval), we need an additional mechanism. A time-dependent process that sets the time for the next inspiratory burst event, without influencing the size of the burst.

3.3.2 The network-based model oscillates with various topologies

Four network topologies and their impact on percolation, or the build-up of network activity, were investigated. In the interest of clarity, the author will only use the word

network when discussing the collection of neurons in the network-based model. The structure known as a graph describes the different topologies and wiring patterns used throughout this section. A graph, in mathematics, is a collection of nodes and edges. The descriptor will suffice for differentiating between a specific topology and a network of neurons like those in the network-based model.

Erds-Renyi

The default connectivity in our model is an Erds-Renyi random (ERR) graph, as was mentioned briefly above (Erdos et al., 1960; Newman, 2010; Prettejohn et al., 2011). The construction of this topology is the simplest. Each pair of nodes in the graph have a probability ρ of sharing a connection. Since the graph in our model is directed, the connections are not reciprocal. Also, as a rule, a node cannot connect to itself. Thus, for a graph of size N there are $N^2 - N$ possible edges. Giving us an average degree, or average number of outgoing (or incoming) edges, of $\langle k_{\text{in/out}} \rangle = N\rho$, where k_{out} is the number of outgoing edges for a node and k_{in} is the number of incoming edges. Due to the implicit randomness when building the ERR graph, the number of edges for all the nodes is a distribution with mean k .

Small world

Formally, a small-world graph (Watts and Strogatz, 1998) describes a structure in which as you increase the number of total nodes N , the average distance between any two nodes, $\langle d \rangle$, grows sublinearly to N . The name “small world” hints at this phenomenon, whereby despite a large graph (for example, $N = 1000$), the distance between any two nodes is only a few edges away (< 4 edges). To visualize, and to see how this graph is constructed, imagine

a ring of nodes where each node is connected to their M closest left and right neighbors (Figure 3.9, here $M = 4$). This structure would currently have no small world properties, as it would take a many edges to go from one side of the ring to the other (Figure 3.9, left). To create a small-world graph, consider each edge that exists already and, with some random probability ρ_w , rewire this edge between a currently connected node and a random node in the ring. This process is known to lead to a topology with small world properties (Prettejohn et al., 2011).

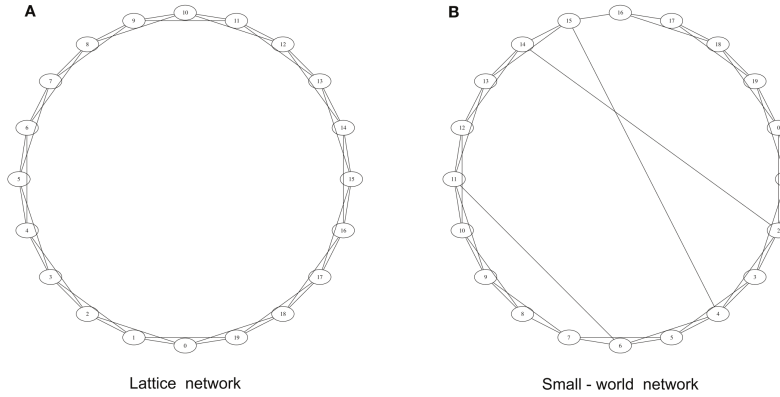


Figure 3.9: Construction of a small-world graph with the Watts and Strogatz (1998) algorithm. Left: a ringed lattice where each node connects to its M closest neighbors. Right: The lattice has been converted into a small-world graph. Here, $M = 4$, $\rho_w = 0.05$, and $N = 20$. Figure adopted from Prettejohn et al. (2011).

Scale free

A scale-free graph describes a topology whereby the degree distribution of the nodes follows a power law distribution. A degree distribution is simply a count of the degrees (edges in or out) each node has. A visual way to determine if a graph is scale free is to plot the fraction of nodes with degree k against the degree k . If on a log plot, this distribution follows a straight line, the graph is scale free. In this style of graph, most nodes have only a few (1 or 2 connections). But a select few nodes have several orders of magnitude more edges.

Many real world systems have scale free connectivity. For example, airport hubs, scholarly citations, human social networks, and even URLs on the world-wide-web have all been shown to exhibit scale free properties. Although, the question of how to define a scale-free graph, and whether or not they are extremely rare or common in the real world, is an ongoing and fascinating debate (Barabási, 2018; Barabasi and Albert, 1999; Broido and Clauset, 2019; Clauset et al., 2009; Holme, 2019).

Scale-free graphs can be constructed artificially, and studied in simulations these topologies have interesting resiliency properties. Scale-free systems are highly resistant to attack. Meaning if nodes are randomly selected and removed, the effect on the graphs structure and function is usually minimal.

A scale-free graph is constructed using the original algorithm from Barabasi and Albert (1999), often referred to as the *rich-get-richer* approach. Whereby, nodes are added to the graph and assigned edges. The chances of receiving an edge with any node already in the graph is dependent on that nodes degree. Thus, nodes with a large number of edges are more likely to receive an additional edge, and thus, the rich get richer.

2d lattice

The final graph depends largely on spatial arrangement. Here, all the nodes are arranged in a two-dimensional lattice. The chances of any two nodes in the lattice sharing an edge are directly proportional to their distance from one another in 2d space. This graph is included because it had been used previously to model a network of excitatory neurons in the preBötC that oscillated via synaptic depression (Guerrier et al., 2015). Otherwise, the lattice is the least realistic for neural systems, which (unlike heart and pancreas cells) are geometrically

unconstrained in their connectivity possibilities.

The network-based model oscillates with various topologies

The model generates oscillations in all four topological configurations (Figure 3.10). The graphs for this simulation do not all have matching average degrees (average edges for each node). Therefore, to control for the different number of connections a neuron might have for a given topology, total synaptic gain d is normalized by the average degree $\langle k \rangle$ of the entire network. This was the only change required between simulations in order to achieve oscillations in a new topology.

An example adjacency matrix for each graph type is shown in Figure 3.10. Each dot in the square represents a 1 in the adjacency matrix, or a connection from neuron i (column) to neuron j (row). The adjacency matrix for the Erds-Renyi graph looks, unsurprisingly, like a random smattering of dots. Every element in the adjacency matrix has a probability ρ of being equal to 1, thus it is truly a random collection of dots (with the lone rule of no dots on the diagonal, i.e., no self connections).

The adjacency matrix for the small-world graph follows next to (but not on) the diagonal, since each node first connects to its neighbors. Then random rewiring of the edges creates some random noise in the adjacency matrix, akin to the ERR graph.

The scale-free graph begins with an all-to-all connected hub of neurons (in this case 30 neurons), and then builds a topology with the *rich-get-richer* approach. This structure can be seen in the adjacency matrix as well, where the top left hub of the matrix is highly dotted, whereas the lower right corner is more sparsely dotted.

The adjacency matrix for the 2d lattice has a pattern of repeating diagonals. The

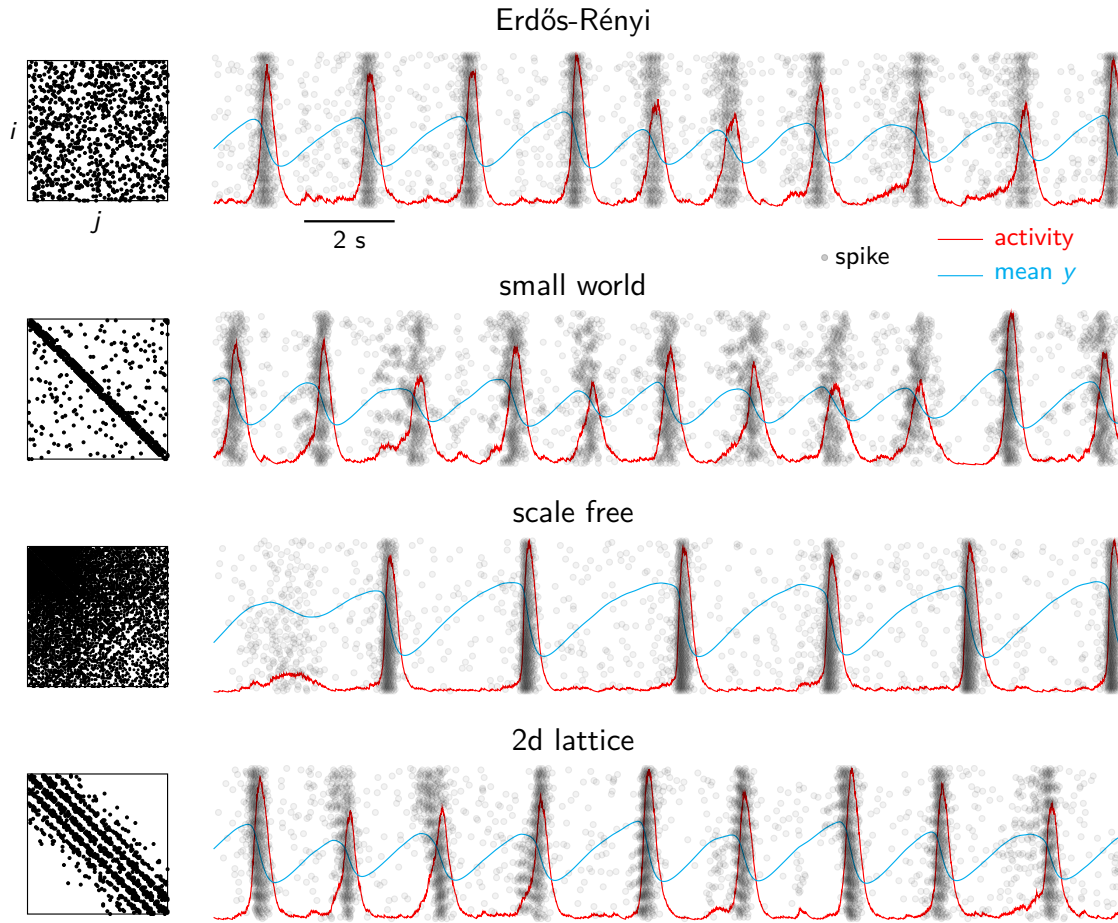


Figure 3.10: Left column: adjacency matrices for each graph type. A dot represents a 1 in the matrix, and a connection from neuron i to neuron j . Notice all matrices, except for the scale-free, are not diagonally symmetric, and are therefore directed networks. Right: Network simulations for different topologies. Red and blue traces represent activity and mean synaptic depression, respectively. Overlaid on the traces is the raster plot, where each black circle represents a spike.

neurons are arranged on a 10 by 10 grid, and then connected based on distance. The repeated diagonal lines in the adjacency matrix are the result of the 10 by 10 grid structure, where new diagonals represent a skip of 10 neurons, to the next closest (11th) neuron. Jitter in the diagonals is the result of random chance, since while close neurons are more likely to be connected, there is still a dice roll on whether or not to connect them.

3.3.3 Different topologies lead to differences in rhythm pattern

While all four topologies do lead to oscillations (Figure 3.10), the shapes, or patterns, of the activity are noticeably different.

Most apparently, oscillations in the networks with small world and 2d lattice connectivity have a longer build up of activity before the burst than oscillations in the other two topologies. This is likely due to the spatial dependence of these graphs, unlike the ERR and scale-free which are entirely spatially independent. Another contribution is the small-world (ironically) and the 2d lattice (unsurprisingly) have the longest average path length¹. Table 3.3 shows the calculated statistics on each of the example graphs used in Figure 3.10. The longer average path length increases delay in network-wide communication, since, on average, it takes more intermediate neurons to activate the entire network at once. That characteristic, along with the spatial relationship between the neurons, causes excitability to take slightly longer to percolate in these networks, and for the propagation of activity to resemble a wave pattern in the raster plot.

Graph	average path length	average degree
Erds-Renyi	2.23 edges	9.71 edges
small world	2.84 edges	6 edges
scale free	1.47 edges	50.7 edges
2d lattice	2.83 edges	9.89 edges

Table 3.3: Average path length and average degree in four different graphs of size $N = 100$

This is in contrast to the next observation from these simulations, which is that the network with scale-free topology has much sharper transitions from recovery to a burst event.

¹It may seem counter intuitive that the small-world graph has the longest path length. After all, the goal when generating the small-world graph was to keep average path length low. But remember, the definition of small-world graph is one where the average path length grows sublinearly with the graph size. It just so happens in this case, where N is relatively small, that the ERR and scale-free graphs have a shorter average path length. However, if we were to increase N , we would see the average path length of the small-world graph grow at the lowest rate

This is no doubt due to how well the network is connected, with an average path length of 1.47 edges, the nodes in this graph are highly connected, leading to more rapid transitions between a quiescent and active state. This is true despite downscaling the strength of an individual synapse, which is normalized by the mean degree of all the nodes in the graph.

Another observation is the apparent failed burst in the network with scale-free topology. Towards the beginning of the scale free simulation, the network seems to be on its way towards a wide-scale burst event, but something fails and the oscillation falls apart. This phenomenon is highly interesting to me, because it is reminiscent of a burstlet in the preBötC (Feldman and Kam, 2015; Kallurkar et al., 2020; Kam et al., 2013b). A future step of this work will be to understand exactly why the network would fail to generate a burst in this situation (Ashhad and Feldman, 2020; Slepukhin et al., 2020).

Ultimately, the goal of these topology studies is to investigate if any variations in network interconnectivity can lead to a more gradual build up of network activity, on the course of 1 or 2 seconds. In order to ask this question, excitability of the system is toned back so that it will operate in what we have been calling type-1 excitability mode, where synaptic depression fully recovers and another process initiates the next burst event. So far, this process has been network noise, but perhaps with a specific network topology, the oscillation can achieve a slow network-distributed build up of activity.

Changing a combination of synaptic gain and average intrinsic firing rate of the network resulted in oscillations where synaptic depression could entirely recover (Figure 3.11) before the next burst. These preliminary simulations however, tell a similar story to what we observed in the ERR graph. After synaptic depression recovers, the system waits for some random network noise to drive the next burst event, and thus the timing of the burst events

is sporadic and the inter-event intervals are not normally distributed (distribution statistics not shown). Despite manipulating the network topology, we were not able to configure such a network whereby excitability was stored and built up on the order of seconds in the network-based model.

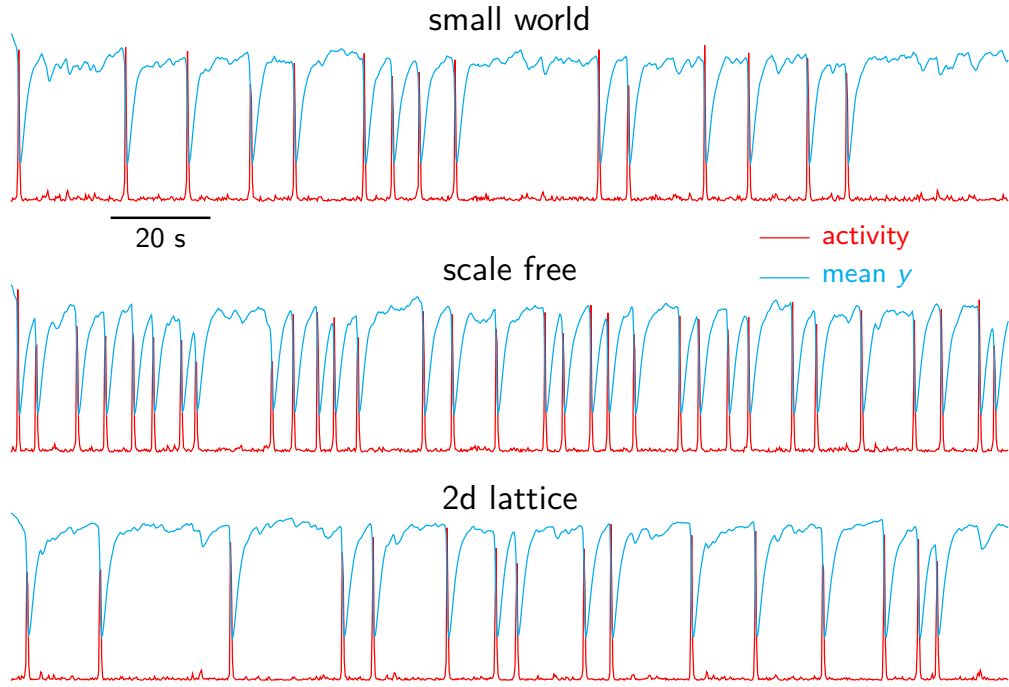


Figure 3.11: Simulations of a network with each topology, and where synaptic depression is allowed to recover entirely before the next burst. Red and blue traces represent activity and mean synaptic depression, respectively.

However, the inability to configure such a topology on-the-fly is not proof that the interconnectivity structure does not play an important role in inspiratory rhythm generation. It is possible something was overlooked in the original model assumptions that prohibits a prolonged (1 to 2 second) build up of activity in the network. Perhaps another parameter can be manipulated to prolong the percolation of activity. Another possibility is, in trying to tone back the excitability of the networks, a regime where the recurrent excitation takes 1 or 2 seconds to build up was passed over. That is a danger of parameter studies, and we would want to think carefully about how to rigorously test the possibility that there is a regime for

the network where burst percolation last an order of magnitude longer than 100 ms.

Nonetheless, the usefulness of the network-based model is undiminished. As discussed in the next section, the simple network-based model of the inspiratory rhythm can be applied to real world experiments to gain insights into possible topology of the preBötC.

3.3.4 Different topologies lead to differences in rhythm breakdown

Another way to compare how realistic the oscillations generated by different topologies are to the real inspiratory rhythm is through a simulated ablation experiment. As mentioned in Chapter 1, experimentalists have targeted Dbx1 neurons in the preBötC with laser ablations and observed how the inspiratory rhythm breaks down as neurons are removed from the network (Wang et al., 2014). In these studies, rhythmogenic Dbx1 neurons in the preBötC were identified and then photo ablated with an ultra-fast pulsed laser, removing them one-at-a-time, in series, from the system, while monitoring respiratory motor output. The study found that rhythm frequency and burst amplitude decreased immediately after the first few cell ablations, and when around 10% of the neurons were ablated, the rhythm stopped entirely. Before the rhythm went completely silent, variance in interburst intervals increased, suggesting laser ablation was deleteriously affecting the core rhythmogenic neurons and their function.

The ablation experiment was replicated with the network-based model by removing nodes and the associated edges from a network (Figure 3.12). This study was repeated for each of the four graph types: Erds-Rényi, small-world, scale-free, and the 2d lattice. The change in burst frequency and burst amplitude was quantified after a random 10% and after a random 20% of the network was removed.

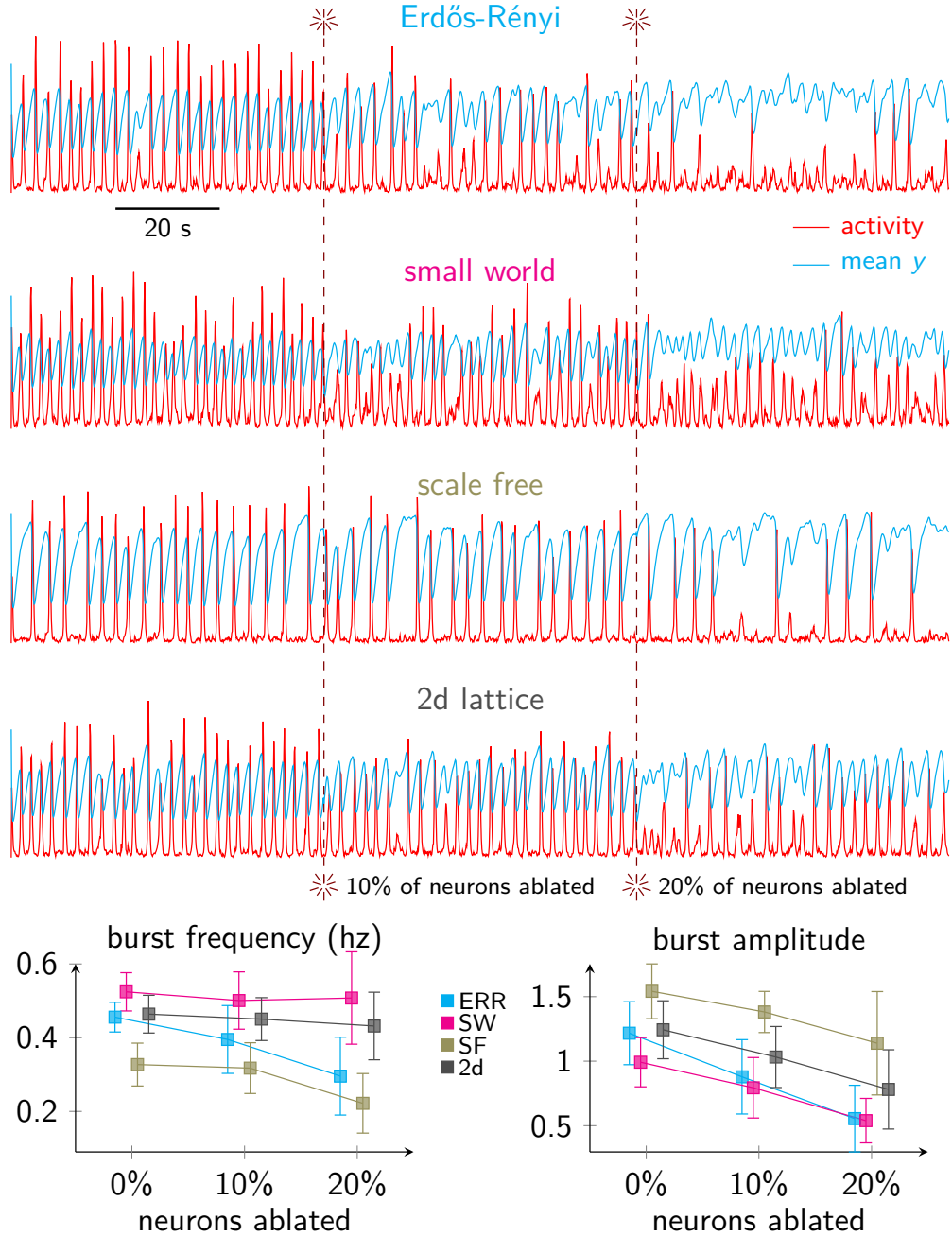


Figure 3.12: Simulated laser ablation study. Top four rows show simulations for each of the four networks. Network activity level and average synaptic depression are shown in red and blue, respectively. Time points where 10 neurons (10% of the initial total) are removed are shown by a dark red 10-pointed star and a dark red dashed line. Below the traces are aggregated data from each network oscillation for different percentages of neurons ablated, 0%, 10%, and 20%. The network with Erds-Rényi (ERR) connectivity is shown in cyan, the network with small-world (SW) connectivity is shown in magenta, the network with scale-free (SF) connectivity is shown in gold, and the network with the two-dimensional lattice (2d) connectivity is shown in grey.

The group data indicate mean frequency of the rhythm was unchanged after removing

10% of the neurons (10/100 neurons total), but the variance in inter-event intervals increased in all cases. Burst amplitude decreased similarly across all networks for both the 10% ablated and the 20% ablated conditions. Interestingly, when 20% of the network was removed, burst frequency in the small world and 2d lattice networks was relatively unperturbed, although inter-event interval variance increased for both rhythms. Meanwhile, burst frequency in the ERR and scale free networks began to drop, and inter-event interval variance increased as well. It is surprising that despite removing 20% of the neurons in the network, oscillations in the networks with small world and 2d lattice topologies continued at the same rate. This is the opposite of what we saw in the biological data, where the inspiratory rhythm amplitude dropped off after the first few ablations, and the period of the rhythm lengthened (i.e., slowed down) and became irregular. Both the ERR and scale-free network track more closely to the biological data. Though, all the models seem to be surprisingly more robust than the preBötC inspiratory rhythm, whose frequency and amplitude decreased after the first couple neurons were ablated.

In conclusion, the networks with ERR and scale free topologies look most similar to the biological network when comparing their change in burst amplitude and frequency after removing individual neurons from the system. Burst frequency decreased, and became very irregular, in the ERR and scale free systems. Additionally, burst amplitude dropped, despite normalizing the activity level by the remaining neurons. Activity is measured in spikes per neuron per second. So after removing a neuron from the network, it is necessary to alter the calculation for activity to account for the change in neurons. Despite this, maximal activity level decreased for all the networks tested as neurons were removed. The small world and 2d lattice systems had the most interesting response to removal of neurons – where the frequency

of the bursts stayed near what it was for the unablated network. This is unexpected, because if recurrent excitation is driving the burst events, then removing neurons should decrease the frequency of that rhythm. It is an oddity that deserves further investigation, perhaps as a next step for the ablation simulations.

3.4 Percolation is sensitive to network topology

Our last, and latest venture into understanding the underlying circuitry of recurrent excitation utilized network science and percolation theory. Our question remained, how can network topology play a role in slowing the build up of activity in a network? We reasoned that one characteristic a “slow build up” network would have is the capacity to contain several isolated clusters of nodes at once. If activity could be stored in sections of the network, rather than activity increasing in the network uniformly, this characteristic could be harnessed to propagate the activity gradually. Therefore, we analyzed different topologies, and recorded how connected the graphs were as nodes were introduced.

In graph theory, the number of components a graph has is the number of isolated clusters it contains. If you can start at one node, and travel to all the other nodes in the graph via the edges, then the graph has one component. If there are still some nodes you cannot reach with the edges available, then the graph has more than one component. See Figure 3.13 for two example graphs with a different number of components.

To algorithmically calculate the total number of components in a graph, start at a node and label that node with a 1. Using edges, travel to every node you can and label each with a 1. Once you have reached all possible nodes, check if there are any nodes still in the graph which have not been labeled. If there are, move to an unlabeled node and assign it a 2.

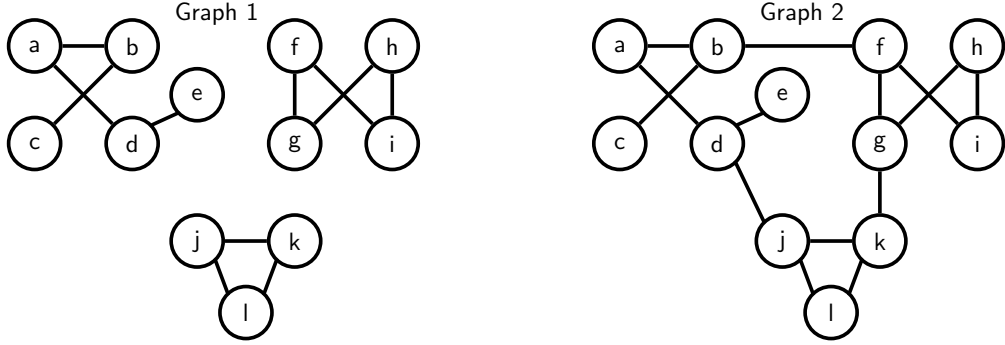


Figure 3.13: Two example graphs with a different number of components. Each graph has 12 nodes (a,b,...,l). Edges are unlabeled solid black lines. Left: Graph 1 has three components. The largest component of Graph 1 is 5 nodes (a,b,...,e). Right: Graph 2 has one component (with 12 nodes), because you can get to any node from any other node.

Continue to move to connected nodes via edges and label each node with a 2. Repeat this process, ratcheting up the number for the label each time you restart the search from an unlabeled node. When no unlabeled nodes remain in the graph, the final labeling number is the total number of components.

Consider a silent network, where none of the nodes are firing. In this network, we can imagine that the edges of the graph are “offline”. They are not relaying any information, and are essentially dead connections. As a neuron starts to spike, we can imagine that node and all of its outgoing edges are added into the graph, or the edges come “online”. We can selectively add one neuron at a time (akin to saying this neuron went from silent to spiking), consequently, we add that neuron’s outgoing edges into the graph since those edges are now relaying information and are effectively “online”.

We simulate a network coming “online” by adding nodes one at a time back into a graph, and calculate the size of the largest component in the graph as a metric for how connected the graph is. First, we build a graph and remove all of the nodes and edges. Then, we pick a random node and reintroduce that node and the edges of that node back into the graph. We continue to add a random node and its associated edges, but after every addition we

recalculate the size of the graph's largest component. By default, the maximum the largest component can be in a growing graph is N , the total number of nodes. This analysis derives from the study of percolation in network science (Stauffer, 1992). We are asking, at what rate does a graph with a certain topology go from mostly separated nodes to one component?

This type of percolation analysis was run for the four different graph topologies that have been investigated thus far: Erds-Renyi, small-world, scale-free, and the 2d lattice (Figure 3.14). It was important for this analysis that the average degree of the graphs be similar. The parameters of each graph were calibrated to produce a structure with a mean degree (out and in) of $\langle k \rangle = 6$. We wanted to keep the mean degree low, but within possible physiological conditions, because we predicted this would have the largest effect on the rate components of the graph would connect. 5000 graphs were built and analyzed for each of the four graph types, and the average statistics are shown in Figure 3.14.

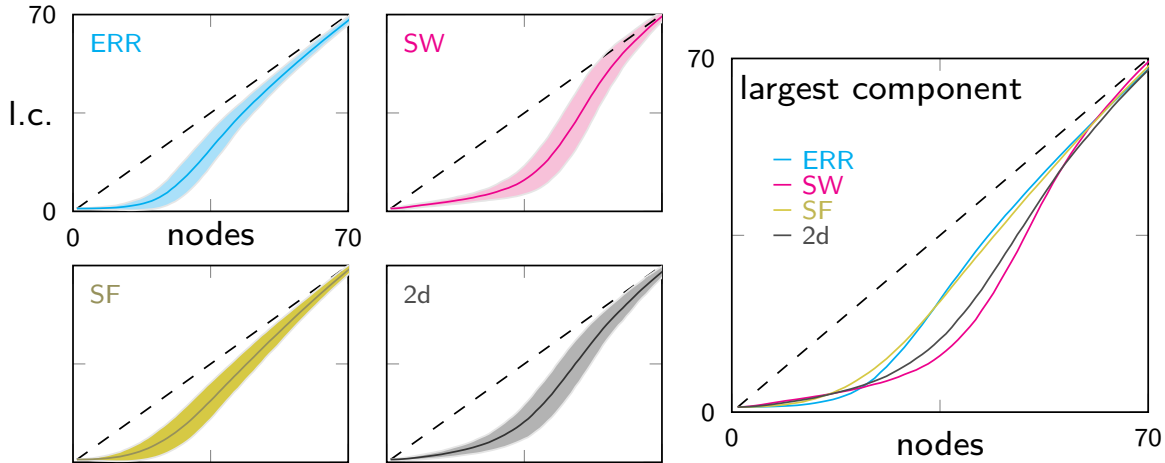


Figure 3.14: Percolation analysis for each graph type, where mean degree is $\langle k \rangle = 6$. A random node, and the outgoing edges of that node, are reintroduced to a graph one at a time. After each node is added, the size of the largest component (l.c.) is calculated. 5000 graphs are simulated for each type (Erds-Renyi: ERR, cyan; small-world: SW, magenta; scale-free: SF, gold; 2d lattice: 2d, grey). The solid line is the average size of the largest component after adding a node. The shaded areas display one standard deviation from that mean. The dashed line is the identity line; this represents the maximum possible size for the largest component, since you cannot have a larger component than you do nodes in the graph. Right: The average largest component at different graph sizes for each of the four types. Graphs are size $N = 100$ nodes, but the axis are zoomed to $N = 70$ nodes to highlight the interesting region.

In all four of the graphs tested, the largest component starts small and remains well below the identity line as the first 10 to 20 nodes are added. This is because as random nodes are added, the chances of these early additions sharing a connection to each other is unlikely. However, as more nodes are added, the size of the largest component begins to increase, and by the time the 70th neuron is added, the graph is entirely connected into a single large component. The small-world topology, and to some degree the 2d lattice and ERR graphs, has an interesting nonlinear curve, around $N = 40$. This suggests the graph undergoes a dramatic phase shift with the activation of just a few neurons. This graph goes from unconnected clusters to one large component with just a few added connections. Compare this to the scale-free structure, which grows more linearly. This tells us that as nodes are added to the graph, they likely are already connected to the largest component, even when the number of nodes is very small. This should not surprise us, since if one of the highly connected nodes of the scale free graph is added, it will connect a significant portion of the graph, and thus most nodes will be included in the largest component.

If we compare the average largest component for different numbers of activated neurons across graph types (Figure 3.14, right), we see the small world (SW, magenta) graph has the strongest nonlinear response to new nodes added to the network. This might suggest that that topology can store distributed activity to a greater degree than the other graphs, especially compared to the scale-free and ERR.

The magnitude of the effect of topology on percolation and the largest component begins to diminish as the average degree in the graph increases. This makes sense, because as the average number of edges for each node increases, the chance to form a single large component becomes more likely, whereas remaining in isolated clusters becomes more difficult (Figure

3.15).

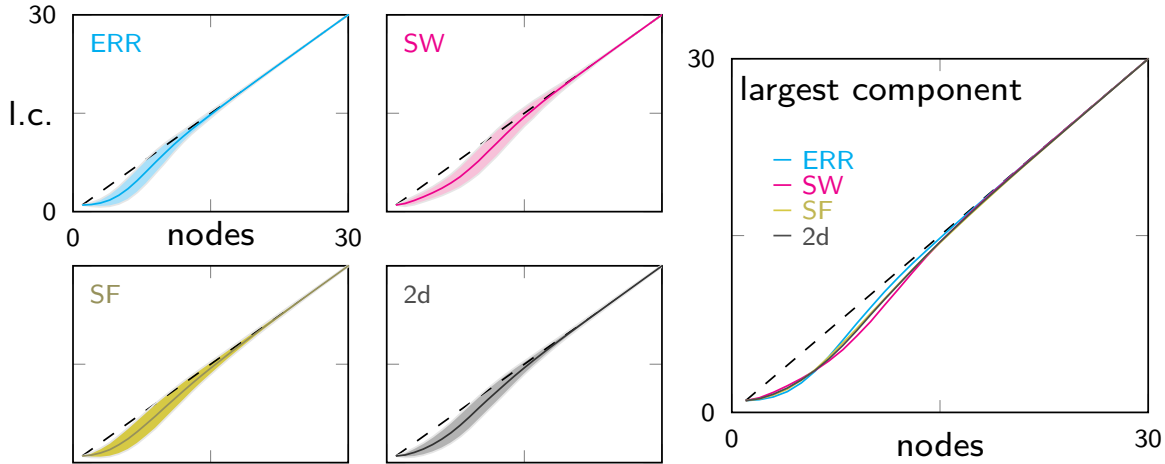


Figure 3.15: Percolation analysis for each graph type, where mean degree is $\langle k \rangle \geq 30$. 5000 graphs are simulated for each type (Erdős-Rényi: ERR, cyan; small-world: SW, magenta; scale-free: SF, gold; 2d lattice: 2d, grey). The solid line is the average size of the largest component after adding a neuron. The shaded areas display one standard deviation from the mean. The dashed line is the identity line; this represents the maximum possible size for the largest component. Right: The average largest component at different graph sizes for each of the four types. Graphs are size $N = 100\text{nodes}$, but the axis are zoomed to $N = 30\text{nodes}$ to highlight the interesting region.

The attempt to apply percolation theory showed that network topology impacts network-wide activation and the rate at which a network comes “online”. The spatially constrained graphs (small world and the 2d lattice) had the most nonlinear response to adding nodes to the system. Therefore, we reason those networks based on those topologies are more likely to facilitate the percolation of activity via isolated clusters in the network. The scale-free graph was the fastest to connect into a giant component, and this partially explains why the bursts of the scale free system in our network simulations (Figure 3.10) came on so rapidly (faster than any other network). That analysis presumes that when a neuron synaptically excites a post-synaptic partner, that is akin to the assembly of a graph connection, which is reasonable. The impact of topology on percolation decreased across all graphs as the mean degree increased, and this finding explains the other reason the bursts from the scale-free

system in the network-based model came on so rapidly, as the scale free system had a larger mean degree than any other network (Table 3.3). This analysis also explains why the 2d lattice system had the most graded build up of activity in the network-based model. The transition to a single large component takes the most number of edge additions in the 2d lattice (more so than in the ERR and scale free networks), and it had a relatively small average degree (compared to the scale-free system) (Table 3.3).

3.5 Discussion

This section covered my work on inspiratory rhythmogenesis. Recall from Figure 3.1 the different phases of the inspiratory rhythm. As discussed earlier, the burst termination phase (Del Negro et al., 2009; Guerrier et al., 2015; Kottick and Del Negro, 2015; Krey et al., 2010), the refractory or recovery phase (Kottick and Del Negro, 2015), and burst generation (Cui et al., 2016; Guerrier et al., 2015) have all been well studied and are essentially solved problems. The last remaining question for inspiratory rhythmogenesis is: what happens between system recovery from the burst-terminating mechanisms and the initiation of the next burst, known as the preinspiratory phase? Perhaps it is a slow (1 to 2 second) build up of activity in the excitatory interneurons of the preBötC, facilitated by network topology, that controls the timing of this ramp up. However, the network-based model could not replicate this phenomenon.

There are several reasons why this could have happened. First, something may have been overlooked during the construction of the model – and therefore an important mechanism the network requires was left out. Alternatively, all the mechanisms the model requires are there, and it is simply some parameter that has been constraining that would solve this issue.

The time constants for synaptic conductance (15 ms) and synaptic depression (1300 ms) was never changed, to keep those parameters in physiological ranges. It is likely that changing synaptic conductance to have a longer time constant would help prolong the buildup of activity, perhaps on the order of a second or two. However, it is unlikely that would be that helpful, since 15 ms is a close estimate for the time constant of an EPSP, and changing this would stray the model too far from realistic parameters.

It's also possible the true topology of the preBötC does play an important role in delaying the propagation of activity, but that we did not test a structure that was close enough to this topology. A 3 dimensional lattice, where the connections have some spatial dependence, seems the most realistic to the author. But exactly how the connections are made and directed is not obvious.

The last possibility, and a next possible step in the project, is contribution from the potassium-mediated depolarization-activated outward current I_A acts as a shunt on excitation. This current is known to impact the inspiratory rhythm (Hayes et al., 2008); when I_A is blocked the frequency of the inspiratory rhythm becomes more irregular. Additionally, I_A has been shown to be expressed on the dendrites of type-1 neurons (Phillips et al., 2018). These two observations fit perfectly into our narrative for what could be responsible for the preinspiratory phase of inspiratory rhythmogenesis. First, the fact that the inspiratory rhythm becomes irregular when I_A is blocked suggests I_A is important for setting the timing for the next burst event. Without a shunt on excitation, the system depends mostly on random noise to drive a burst, and the timing between the events becomes irregular and more exponentially distributed. Second, the fact that the outward current generated by I_A is localized to the dendrites minimizes the impact it has on the size of the next burst. Whereas

an outward current generated near the soma will counteract subthreshold inward currents and reduce the magnitude of an inspiratory burst, an outward current in the dendrites simply dampens EPSPs and does not have as much of an influence on the interactions of somatic currents. I_A inactivates after a few hundred milliseconds, therefore, it may act to diminish spurious EPSPs, until the network activity is high enough to inactivate I_A in the dendrites and initiate a burst event. My next step in this project would be to include something like I_A in the network- or activity-based model, and see if this would reconcile the preinspiratory phase of inspiratory rhythmogenesis with our observations about burst size and preceding inter-event interval.

3.6 Appendix: Modeling noise in the activity models

Figure 3.4 shows simulation of episodic activity (a) and synaptic depression (s) for the two-variable inspiratory model with parameters leading to type 2 stochastic oscillations (panel B) and type 1 stochastic excitability (panel C). The Gaussian white noise term ($\hat{\xi}$) of equation 3.1 is a rapidly fluctuating function with mean zero ($\langle \hat{\xi}(t) \rangle = 0$) and two-time covariance of the form (Keizer, 1987)

$$\langle \hat{\xi}(t)\hat{\xi}(t') \rangle = \gamma(a, s)\delta(t - t'), \quad (3.22)$$

consistent with intrinsic noise that accounts for stochastic action potential firing. The state-dependent magnitude of these intrinsic fluctuations, $\gamma(a, s)$, is derived by considering the rates of the forward and reverse elementary processes implied by the deterministic ODE for

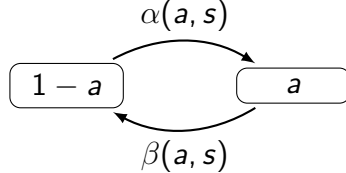
the network activity (Equation 3.1),

$$\frac{da}{dt} = \frac{a_\infty(w \cdot s \cdot a) - a}{\tau_a} = \frac{a_\infty(s, a) - a}{\tau_a}.$$

where $\lim_{x \rightarrow -\infty} a_\infty(x) = 0$ and $\lim_{x \rightarrow \infty} a_\infty(x) = 1$ (Equation 4.6). To understand the second equality, recall that $a_\infty(w \cdot s \cdot a) = a_\infty(a, s)$ is a function of both state variables, but w is a parameter. Defining α and β to simultaneously solve $\tau_a = 1/(\alpha + \beta)$ and $a_\infty = \alpha/(\alpha + \beta)$, we see that Equation 3.1 is equivalent to

$$\frac{da}{dt} = \alpha(a, s) \cdot (1 - a) - \beta(a, s) \cdot a,$$

where $\alpha = a_\infty/\tau_a$ and $\beta = (1 - a_\infty)/\tau_a$ are functions of a and s through $a_\infty(a, s)$. This equation is consistent with forward and reverse elementary processes as diagrammed below:



The amplitude of fluctuations used in Equation 3.1 is the sum of the forward and reverse rates of transition, given by $\alpha(a, s) \cdot (1 - a)$ and $\beta(a, s) \cdot a$, respectively. Thus, the state-dependent fluctuation magnitude is

$$\begin{aligned}\gamma(a, s) &= \eta [\alpha(a, s) \cdot (1 - a) + \beta(a, s) \cdot a] \\ &= \frac{\eta}{\tau_a} [a_\infty(a, s) \cdot (1 - a) + (1 - a_\infty(a, s)) \cdot a],\end{aligned}$$

where η scales the strength of the noise. Larger networks with more neurons will have

reduced noise compared to smaller networks. In the two-variable eupnea model (Equations 3.8-3.9 and Figure 3.4), we do not include a noise term in the equation for s because the number of synapses is several orders of magnitude greater than the number of neurons. In the three-variable eupnea model (Equations 3.10-3.12 and Figure 3.5), three uncorrelated noise terms are included. The best fit with experiment was obtained by scaling the noise strength for cellular adaptation (θ) to be several-fold greater than the noise for network activity.

Chapter 4

The preBötzinger complex generates sigh rhythm via intracellular calcium oscillations in mice

4.1 Introduction

Rhythms are ubiquitous throughout the brain. They are involved in countless behaviors, from cognitive tasks like attention (Fiebelkorn et al., 2018; Helfrich et al., 2018) and memory (Latchoumane et al., 2017), to motor activities such as locomotion (Kiehn, 2016), chewing (Westberg and Kolta, 2011), and breathing (Del Negro et al., 2018). Understanding the neural origins of behavior requires understanding the cellular and synaptic mechanisms that endow circuits with rhythmicity. This is particularly true for motor systems, in which periodic body movements can be attributed to central circuits that produce the underlying rhythm and rudimentary motor pattern for the behavior (Grillner, 2006; Grillner and

El Manira, 2020). Breathing behavior presents a challenging problem for neuroscientists because it involves two disparate rhythms: one that generates eupnea to ventilate the lungs for gas exchange (0.2 Hz) and another much slower rhythm for sighs, which optimizes pulmonary function (< 0.01 Hz).

Both of these rhythms are generated in the preBötzinger Complex (preBötC), located in the ventral medulla (Del Negro et al., 2018; Smith et al., 1991). Bursts of neural activity in the preBötC drive the inspiratory phase of eupnea. This phenomenon occurs on the order of seconds, and is referred to as the inspiratory rhythm. The inspiratory burst emerges via recurrent excitation amongst a network of glutamatergic interneurons and is terminated by synaptic depression and other activity-dependent membrane currents (Del Negro et al., 2002a, 2009; Feldman and Kam, 2015; Funk et al., 1993; Kottick and Del Negro, 2015; Krey et al., 2010; Wallen-Mackenzie et al., 2006). A sigh breath also begins as a network-wide burst in the preBötC (Li and Yackle, 2017; Lieske et al., 2000; Ramirez, 2014; Ruangkittisakul et al., 2008). Typically, the volume of exchanged air during a sigh is two to five times that of a eupneic breath, and the corresponding burst of neural activity in the preBötC has a larger amplitude and integrated area than the inspiratory-related activity. The rhythms are temporally coupled: sigh bursts typically build from the crest of – or immediately follow – an inspiratory burst. After a sigh event is a post-sigh apnea, where the subsequent inspiratory burst is delayed by a third, to a half of, one additional inspiratory period. These observations affirmed by numerous *in vivo* and *in vitro* recordings suggest that eupnea and sigh rhythms are certainly coupled (Borrus et al., 2020; Li and Yackle, 2017; Lieske et al., 2000), but they do not clarify whether the rhythms come from one or rather two separate populations within the preBötC.

While the origins of the inspiratory breathing rhythm are well understood (Ashhad and Feldman, 2020; Baertsch and Ramirez, 2019; Kallurkar et al., 2020; Kam et al., 2013b), the cellular and synaptic origins of the sigh rhythm are still unclear. When the preBötC was originally identified as the source of the sigh rhythm, every recorded neuron that participated in the sigh burst also participated in the inspiratory burst, suggesting the populations that drove both rhythms were entirely overlapped (Lieske et al., 2000). However, in 2008, one team showed that roughly 5% of inspiratory preBötC neurons participated in the sigh bursts exclusively, and were uncorrelated with the inspiratory rhythm (Tryba et al., 2008). They dubbed these sigh-only neurons. That same year, another group using Ca^{2+} imaging of preBötC neurons found the opposite result; they did not find a single neuron that participated in the sigh burst exclusively, and they concluded the populations that generate inspiratory and sigh rhythms are entirely overlapped (Ruangkittisakul et al., 2008). Thus, there is currently substantial ambiguity over the issue of whether the sigh rhythm emerges from the same population of neurons that drive the inspiratory rhythm, or whether the populations only partially overlap and there is a population of sigh-only neurons.

The most developed framework for sigh rhythmogenesis suggests that intracellular calcium (Ca^{2+}) oscillations in preBötC interneurons drive the rhythm (Toporikova et al., 2015). This group showed that cadmium, a non-specific Ca^{2+} -channel antagonist, disrupts sigh activity *in vitro*. While cadmium blocks extracellular Ca^{2+} channels, it may result in a decrease in intracellular Ca^{2+} that interferes with ongoing intracellular Ca^{2+} oscillations, lending support to their hypothesis that intracellular Ca^{2+} oscillations drive the sigh rhythm. Additionally, they show that the sigh rhythm is voltage-insensitive, and it depends on the hyperpolarization-activated inward current I_h . Surprisingly, their model assumes that the

population of neurons generating the sigh rhythm is entirely separate from the population generating the inspiratory rhythm. Furthermore, the coupling between the two rhythms in their model depends on synaptic inhibition, which was recently shown to not be necessary for temporally linking the oscillations (Borrus et al., 2020).

In this study, we differentially modulate the inspiratory and sigh rhythms to investigate their underlying mechanisms. We find that, in fact, I_h is not important for generating the sigh rhythm. We show that cellular excitability readily regulates the frequency of the inspiratory rhythm, but it has only a minimal impact on sigh frequency, suggesting a voltage-independent mechanism for sigh rhythmogenesis. Whereas the inspiratory rhythm slows and eventually stops at low levels of cell excitability, the sigh rhythm continues to operate even at excitability levels lower than were sufficient to stop the inspiratory rhythm.

The sigh rhythms relative independence on membrane excitability could be compatible with a possible glial role in sigh rhythmogenesis. However, here we disrupt purinergic gliotransmission (which is the dominant form of glia-neuron signaling in the preBötC) and find no effect on sigh frequency or amplitude. Next, we determined if the inspiratory and sigh rhythms come from one or two population of neurons. Using Ca^{2+} imaging to monitor population activity in preBötC, we find no evidence of sigh-only neurons, i.e., neurons that are only active during sigh events, suggesting a single population underlies both rhythms.

Based on these observations, we construct a model for inspiratory and sigh rhythm generation whereby the sigh rhythm is generated by a biochemical oscillator dependent on intracellular Ca^{2+} , quasi-independent of voltage-dependent mechanisms that govern inspiratory rhythm. The disparate mechanisms of the two rhythms enable them to operate independently within the same neuronal population and to be differentially modulated according

to physiological exigencies. Unlike the previous model for sigh generation, ours does not depend on I_h , has one population of neurons generating both inspiratory and sigh rhythms, and does not depend on synaptic inhibition.

Testing the predictions of the mathematical model, we disrupt endoplasmic reticulum calcium uptake by SERCA-type ATPase pumps *in vitro* and find a change in sigh rhythm frequency, which depends on the concentration of SERCA blockers. Next, we show blocking inositol 1,4,5-trisphosphate receptors (IP_3 Rs) in the preBötC leads to a substantial decrease in sigh frequency, which also agrees with model predictions as well. This work elucidates, on a cellular level, how intracellular Ca^{2+} oscillations drive the sigh rhythm and reveals how one neural population can produce two distinct rhythms, providing a model example of a dual rhythm generator that helps elucidate how a multitude of brain rhythms, with different frequencies and amplitudes, may be concurrently generated.

4.2 Results

4.2.1 I_h does not contribute to sigh rhythmogenesis

We tested the role of the mixed-cation-mediated hyperpolarization-activated inward current, I_h in sigh rhythmogenesis. In rhythmically active slices, we recorded the frequencies of the inspiratory and sigh rhythms before and after bath application of 50 μM ZD7288, a selective blocker for I_h . Sigh rhythm continued in the presence of the I_h antagonist, and its frequency was unaffected (control sigh frequency measured $0.87 \pm 0.55 \text{ min}^{-1}$, following application of ZD7288 the sigh frequency measured $1.12 \pm 0.38 \text{ min}^{-1}$, N=3, paired t-test p=0.41) (Figure 4.1B). These data suggest that I_h does not contribute to sigh rhythmoge-

nesis. These results differ from the findings of a previous study (Toporikova et al., 2015), perhaps due to an age difference in the mice used. Whereas our experiments use postnatal mice (P0–P4), the previous study used exclusively embryonic mice, which might express different ion channels and pumps, influencing the sigh generation pathway. Figure 4.1C shows event frequency, when counting both sigh and inspiratory bursts, significantly increases after the block of I_h (control event frequency measured 0.19 ± 0.06 Hz, following application of ZD7288 event frequency measured 0.22 ± 0.07 Hz, $N=3$, paired t-test $p=0.026$)

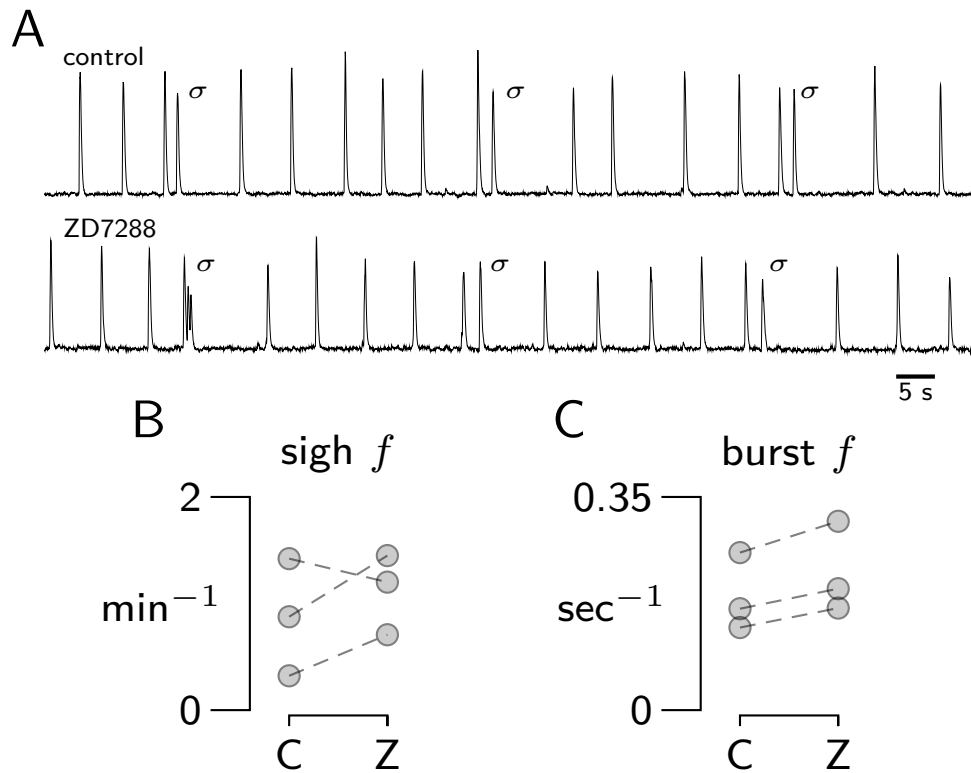


Figure 4.1: Impact of pharmacological block of the mixed-cation hyperpolarization-activated inward current I_h on sigh and inspiratory rhythm. A: Representative traces from XII rootlet of the inspiratory and sigh rhythms during control and after application of the I_h blocker ZD7288. Sigh bursts are denoted with a σ . B: Change in sigh frequency after application of ZD7288 (Z) for $N=3$ slices. Each set of markers connected by a dashed line represents one slice, or one experiment. Y-axis is sighs per minute. C: Change in burst frequency (inspiratory and sigh bursts counted together) after application of ZD7288 (Z). Y-axis is in Hz, or events per second.

4.2.2 The sigh rhythm is more voltage-independent than the inspiratory rhythm

We examined the role of cellular excitability on preBötC rhythms to gain insights into their underlying mechanisms. We recorded the frequencies of the inspiratory and sigh rhythms while manipulating the baseline membrane potential of constituent preBötC neurons via extracellular K⁺ concentration ([K⁺]_o). Both rhythms are displayed in a preBötC field recording under control conditions where ([K⁺]_o) is maintained at 9 mM (Figure 4.2A, left). When ([K⁺]_o) is lowered to 3 mM, inspiratory frequency slows until it is ostensibly silent. The sigh rhythm, however, continues despite the decrease in network excitability (Figure 4.2A, right).

We quantified the rhythm frequencies at intermediate values for ([K⁺]_o), and found the inspiratory rhythm was voltage-dependent (Figure 4.2B, left) (Kallurkar et al., 2020). At typical control conditions of 9 mM ([K⁺]_o), mean inspiratory frequency measured 0.14 ± 0.05 Hz (N = 19). Frequency slowed as network excitability decreased. At or below 5 mM ([K⁺]_o) the inspiratory rhythm ceases in most cases, which reflects, for group data, a 100% decrease from starting inspiratory frequency (Figure 4.2B). These data suggest that the mechanism underlying the inspiratory rhythm slows down, and often stops, when excitability is decreased.

In contrast, we found that the sigh rhythm did depend on baseline excitability, but to a lesser extent than did the inspiratory rhythm (Figure 4.2B). At control conditions of 9 mM ([K⁺]_o), the mean sigh frequency was 0.66 ± 0.17 min⁻¹ (N = 13). The sigh rhythm slowed as cellular excitability dropped, and when ([K⁺]_o) was reduced to 3 mM ([K⁺]_o) the mean sigh rhythm was 0.26 ± 0.08 min⁻¹ (N = 5). That represents a 60.6% reduction in sigh

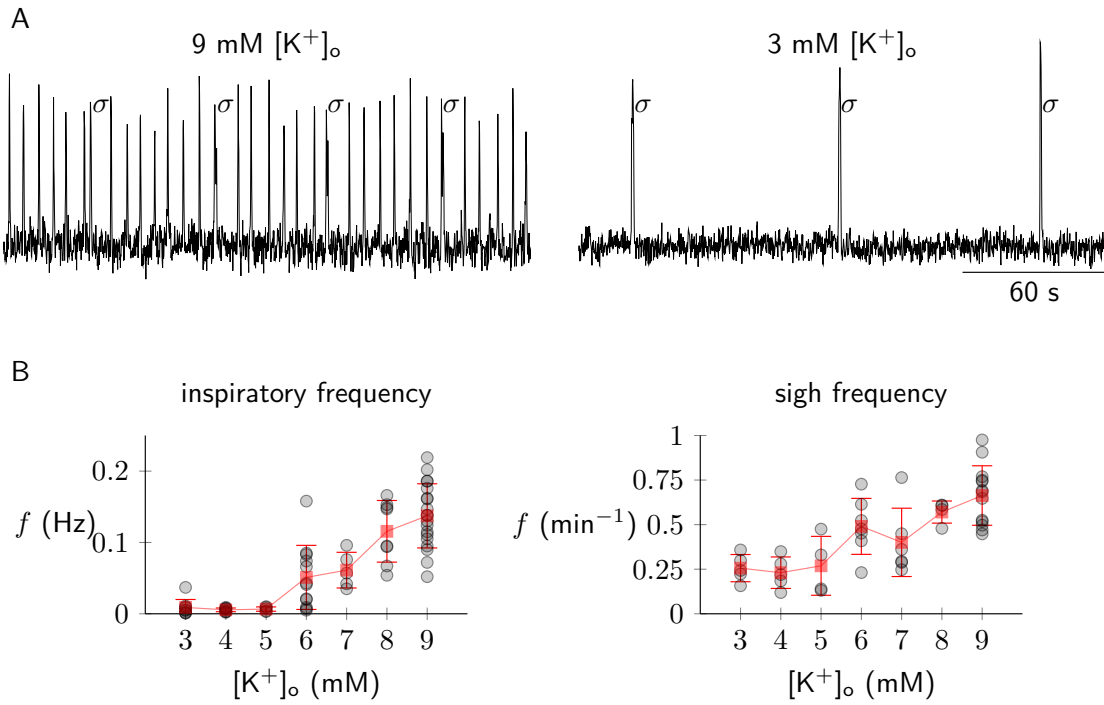


Figure 4.2: Differential voltage-dependence of inspiratory and sigh rhythms. A left: preBötC field recording capturing both the inspiratory rhythm and the sigh rhythm at control conditions of 9 mM extracellular K⁺ ($[K^+]$ _o). Sigh events are highlighted with a σ , and can be distinguished by their increased area and the presence of a post-sigh apnea. A right: preBötC field recording at 3 mM ($[K^+]$ _o). Sigh events are highlighted with a σ . X scale bar is 60 seconds. B left: Quantification of inspiratory event frequency for discrete extracellular K⁺ concentrations, ($[K^+]$ _o). Each black circle for a particular ($[K^+]$ _o) represents one slice. The red square shows the mean frequency across all slices (black circles) in that condition. N=19. B right: Quantification of sigh event frequency across discrete ($[K^+]$ _o). N=13.

frequency. While the sigh rhythm does depend on the cellular excitability, it is much less sensitive than the inspiratory rhythm, which stopped entirely.

Despite the silencing of inspiratory-related emergent network activity, the sigh rhythm continued to operate. This observation suggests the sigh rhythm does not depend on input or feedback from the inspiratory rhythm.

4.2.3 Glia-mediated purinergic signaling is not necessary for sigh rhythm generation

Because the sigh rhythm lacks strong voltage dependence, we considered whether the sigh-generating network might be non-neural (Ramirez et al., 2021). Glia represent a possible candidate, as glia are known to generate spontaneous intracellular Ca^{2+} oscillations as well as intercellular Ca^{2+} waves (Charles, 1994; Guthrie et al., 1999; Hirase et al., 2004). Gliotransmission is also known to modulate the inspiratory preBötC rhythm (Huxtable et al., 2010; Okada et al., 2012; Rajani et al., 2016, 2018; Reklow et al., 2019), leading us to investigate what role, if any, glia have in generating the sigh rhythm.

Using two-photon imaging, we record calcium transients in preBötC interneurons derived from progenitors that express the transcription factor Dbx1, which comprise the rhythmic preBötC kernel for inspiration (Figure 4.3A) (Bouvier et al., 2010; Gray et al., 2010; Vann et al., 2016, 2018; Wang et al., 2014). We simultaneously record motor output from the XII nerve rootlet to monitor inspiratory and sigh rhythms. The ΔF traces of Dbx1 preBötC neurons show a large calcium transient during sigh events (Figure 4.3B). Blocking purinergic P2 receptors with bath application of a cocktail of antagonists ($50 \mu\text{M}$ PPADS and Suramin with $10 \mu\text{M}$ TNP-ATP, MRS2179, and MRS2578) did not stop these large calcium transients (Figure 4.3C). In the presence of the P2 antagonist cocktail, neither the sigh frequency ($0.73 \pm 0.22 \text{ min}^{-1}$ in control vs $0.74 \pm 0.18 \text{ min}^{-1}$ in blockers) nor the event frequency ($0.27 \pm 0.06 \text{ Hz}$ in control vs $0.26 \pm 0.07 \text{ Hz}$ in the presence of the P2 antagonist cocktail) was significantly affected (Figure 4.3D and 4.3E).

We developed a quantitative approach for determining the presence of sigh bursts that depends on the post-sigh apnea. We expect a distribution of inter-event intervals from pre-

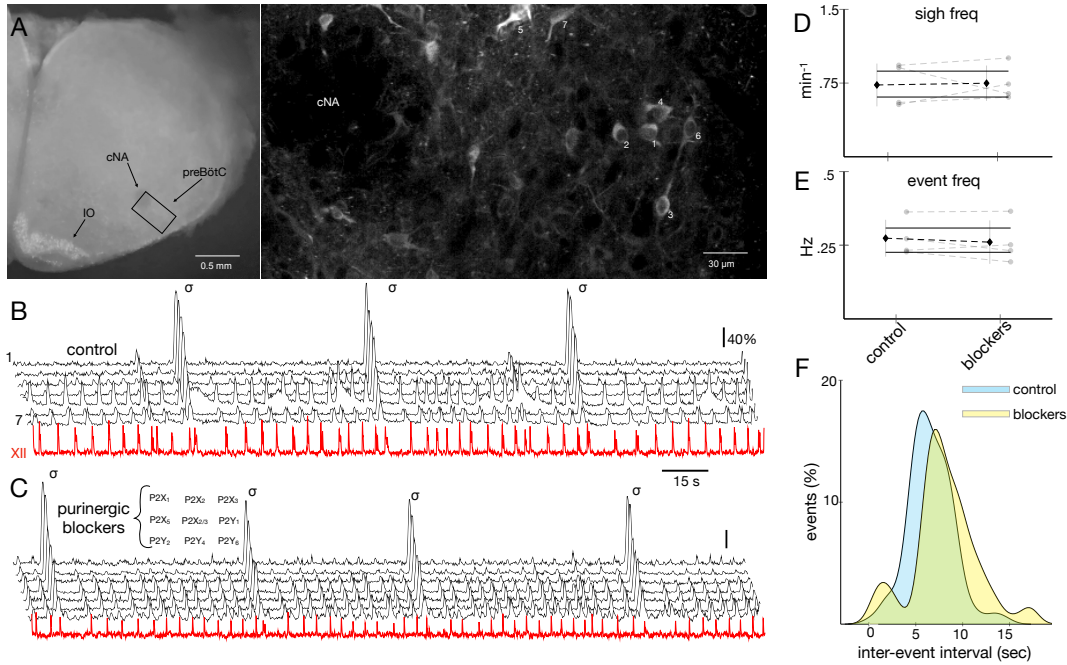


Figure 4.3: Purinergic signaling is not necessary for generating the sigh rhythm. A: Images of the *in vitro* slice preparation and a zoom in on the preBötC. Highlighted for references are in inferior olive (IO) and compact nucleus ambiguus (cNA). B: Calcium imaging of seven Dbx1 neuron. In red is motor output recorded from XII rootlet. Sighs are marked with σ . C: Calcium imaging after application of the purinergic blockers. D & E: Group data on the change in sigh frequency (D) and burst frequency (E). Black markers and dashed lines show average change over all experiments. Grey markers and dashed lines show frequency data for individual experiments. D y-axis is in sigh per minute. E y-axis is in bursts per second. F: Distribution of the inter event intervals between all events in control (blue) and in glycinergic blockers (yellow).

BötC recordings to have a bimodal distribution – one peak for intervals between inspiratory events and one smaller peak for prolonged intervals due to post-sigh apneas. We observe this bimodal distribution in control conditions (Figure 4.3F), where the mean inter-event interval peaks near 5 s, but there is a discernable peak around 13 s that reflects a smaller number of post-sigh apneas, which are less numerous because the sigh rhythm is slower. This bimodal distribution becomes even more discernible after blocking purinergic signaling. Note that a third peak can be observed in the antagonist cocktail near the 1 s mark; this likely reflects the short (< 1 s) time gap between a sigh and the closely preceding inspiratory burst (Borrus et al., 2020). This analysis shows quantitatively that the sigh rhythm is present in control

and after blocking purinergic signaling. Together with the calcium recordings, these data demonstrate that the sigh rhythm is unlikely to be glial in origin.

In addition to the cocktail of purinergic receptor antagonists, we also investigated the role of P2Y₁ receptors specifically with the P2Y₁ receptor antagonist MRS2279. P2Y₁ receptors on preBötC neurons can modulate preBötC inspiratory frequency (Rajani et al., 2016, 2018). Furthermore, a recent report in preprint form presents evidence that the P2Y₁ receptors are critical for sigh rhythm generation (Ramirez et al., 2021). Therefore, we bath applied the P2Y₁ receptor antagonist MRS2279 and observed the sigh rhythm with two-photon imaging as above. However, we found that the sigh rhythm was not impacted during or after application of MRS2279 (Figure 4.4), further indicating gliotransmission does not help generate the sigh rhythm.

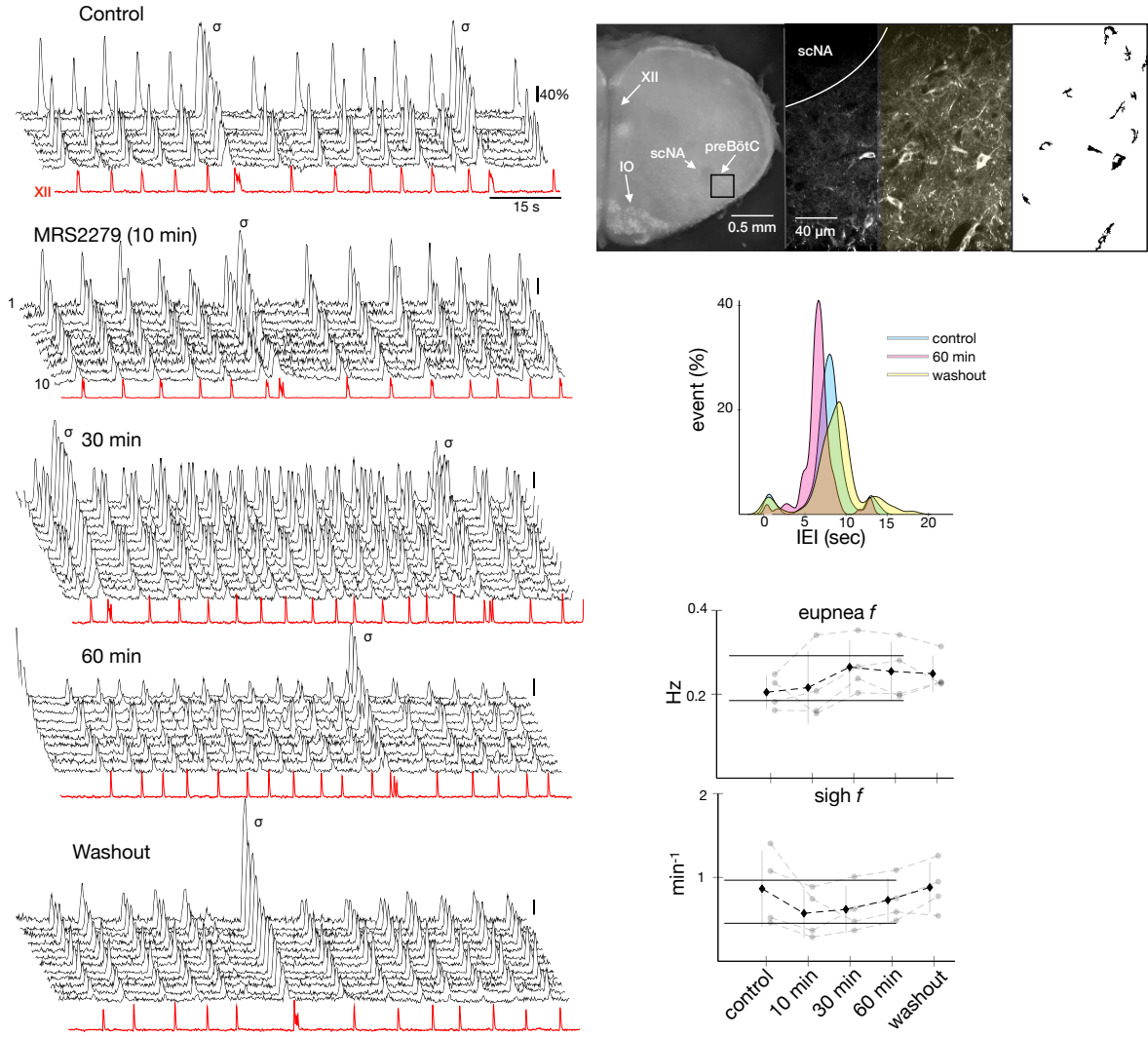


Figure 4.4: Investigating effect of MRS2279 (20 mM) application on sigh frequency. A left, slice containing preBötC with XII motor nucleus, inferior olive, and nucleus ambiguus labeled. A middle, average fluorescent change of ventral medulla. The preBötC is highlighted yellow. A right, regions of interest within preBötC. B, individual fluorescence traces (black) of regions of interest and hypoglossal motor output (red) during control, at different time points of MRS2279 application, and during washout. Sighs are marked with σ . C, group data of average eupnea (top) and sigh (bottom) during control, at different time points, and during washout. A seven-minute epoch centered at the provided time point was used to calculate these averages. Horizontal black bars represent 95% confidence interval. Histogram of inter-event intervals in control, at 60 minutes, and in washout.

4.2.4 The sigh and inspiratory rhythms arise from the same population of neurons

Neuronal activity in the preBötC is recorded using Ca^{2+} imaging with the two-photon system. We record statistics on the presence of putatively sigh-only neurons, and then a

conclusion about the existence of sigh-only neurons will be drawn.

Out of the several dozen imaging studies, which included several hundred neurons, there has been no sigh only neurons. This preliminary observation casts doubt on the hypothesis that there is a population of preBötC neurons that are sigh-only. Quantitative analysis on the statistics for this study have not been calculated yet.

4.2.5 Intracellular Ca^{2+} oscillations can lead to sigh bursts

The sigh rhythm continues to operate despite a substantial decrease in cellular excitability and after disrupting gliotransmission. Additionally, our two-photon imaging studies reveal a large calcium transient in preBötC neurons during a sigh event. These observations suggest the mechanism underlying the oscillations could be biochemical involving intracellular Ca^{2+} oscillations.

We propose a framework for sigh rhythrogenesis, whereby sigh events are driven by slow intracellular Ca^{2+} oscillations. In this model, Ca^{2+} enters the neuron, during inspiratory-related burst events or by passive Ca^{2+} entry into the cytosol, and is sequestered into intracellular calcium stores such as the endoplasmic reticulum (ER) via SERCA pumps. The Ca^{2+} concentration continues to increase in the ER, and in the cytosol to a lesser extent as the concentration gradient across the ER becomes more extreme. On the time course of minutes, Ca^{2+} in the cytosol reaches a critical concentration. Binding to inositol 1,4,5-trisphosphate receptors (IP_3R) on the ER, it begins a positive feedback loop of Ca^{2+} -induced Ca^{2+} release which leads to a large Ca^{2+} dump from the ER. This Ca^{2+} flux into the cytosol triggers calcium-activated non-specific currents (I_{CAN}), leading to a network-wide burst event. Excess Ca^{2+} is extruded out of the cytosol and the entire process starts again.

We constructed a mathematical model that simulates the key components of the inspiratory rhythm, as well as our proposed framework for sigh rhythm generation and the mechanisms that couple the two oscillators (Figure 4.5). The inspiratory subsystem is based on the recurrent excitation hypothesis for inspiratory rhythmogenesis, and the mathematics follow the work of Tabak et al. (2000b, 2001b), reviewed in Tabak and Rinzel (2005b). In the model, network activity (a) settles to a steady-state level, dependent on the current activity. In our case, the steady-state activity is always greater than the current activity level, therefore, network activity will increase through recurrent excitation until the network is at a maximum activity state. To counter this runaway activity, synaptic depression (s) shunts and terminates the activity by decreasing the steady-state a level to below the current a . With only activity (a) and synaptic depression (s), we can construct an activity-based model with oscillations, akin to Tabak et al. (2000, 2001). We discovered that, in order to configure the model of inspiratory rhythm generation so that it replicates the statistical observations of the inspiratory rhythm *in vivo*, we required an additional slow variable (θ) to set the timing of the next burst event (Figure 3.5). We refer to this variable as cellular adaptation; it sets a dynamic threshold for the activation of the next burst, making a burst more likely as time goes on.

Two additional state variables model intracellular calcium dynamics: cytosolic calcium concentration (c) and total calcium concentration in the cell (c_{tot}) (Figure 4.5B). The calcium subsystem modeling builds off of work from Keizer et al. (1995a) and Friel and Chiel (2008b). We couple the inspiratory and sigh subsystems based on the movement of intracellular Ca^{2+} (Figure 4.5C). That is, when Ca^{2+} concentration in the cytosol (c) transiently increases during a Ca^{2+} -induced Ca^{2+} release event, it activates I_{CAN} which drives an inward current

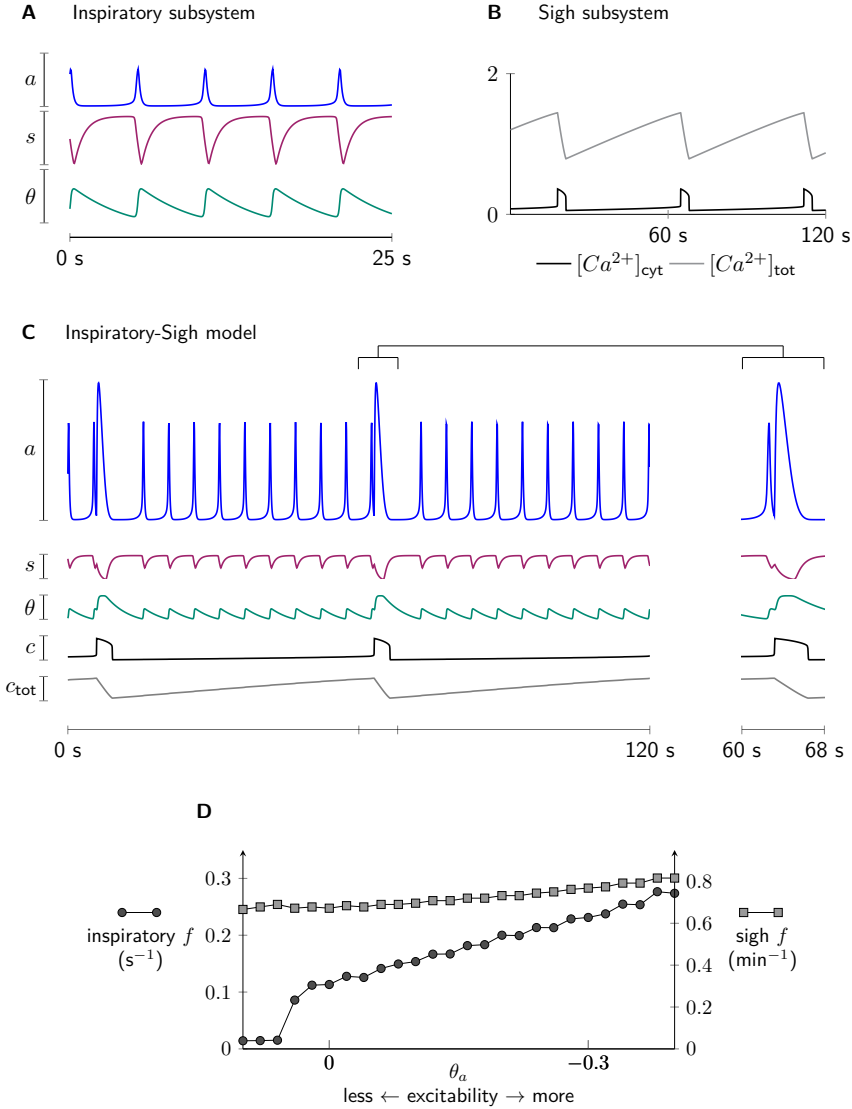


Figure 4.5: (Caption next page.)

leading to an oversized burst event, or a sigh burst. Conversely, during each inspiratory burst, Ca^{2+} enters the neuron and increases the cytosolic and ER Ca^{2+} concentrations, decreasing the time until the next sigh burst. For extended information on the development of the sigh model, and how it was connected to the inspiratory model, see Section 4.5.

We validated our model of inspiratory and sigh rhythmogenesis by replicating the differential voltage-dependence we observed *in vitro*. We manipulated the excitability of the model system and found that the inspiratory rhythm was highly sensitive to the change

in excitability while the sigh rhythm was more robust (Figure 4.5D). This mirrors the experimental results we found *in vitro* (Figure 4.2). The math model demonstrates that our hypothesis for how one group of neurons generates two distinct oscillations can work *in silico*.

Figure 4.5: Validation of an inspiratory and sigh rhythm generator from the same population *in silico*. A: Trajectories for the inspiratory subsystem. a , s , θ are the network activity, synaptic depression, and refractoriness respectively. The y axes range from 0 to 1. B: Trajectories for the sigh subsystem. The black line shows the cytosolic calcium concentration, the grey line shows total calcium in the cell (calcium in the cytosol + calcium in the ER). C: Simulation of the coupled inspiratory and sigh systems. Magnification on the right highlights a sigh event. D: Dependence of the two rhythms on excitability in the coupled model. Black circles track the inspiratory frequency, matched with the y axis on the left showing frequency (f) in seconds $^{-1}$. Grey squares show the sigh frequency, and their y axis is on the right showing frequency (f) in minutes $^{-1}$. The x axis shows the tuning of a parameter, θ_a , that sets the midpoint for the activity steady-state curve. See Section 4.5 for more details.

4.2.6 Disrupting SERCA activity impacts sigh frequency

To test the importance of intracellular calcium dynamics in generating the sigh rhythm, we sought to impair SERCA activity in preBötC interneurons. Model simulations predicted that when SERCA activity was partially blocked, sigh frequency would increase while sigh magnitude would decrease (Figure 4.6A). As SERCA blockers diminish the ability to refill the ER, the Ca^{2+} stores build up more slowly than during control, and IP_3 receptors are activated more quickly, due to increased Ca^{2+} in the cytosol. Thus, the sigh rhythm frequency increases, but sigh burst area decreases due to a reduced Ca^{2+} release event (Figure 4.7). The model also predicts that when the SERCA pumps are impaired further, sigh events will stop entirely (Figure 4.6A).

We tested these predictions *in vitro* on rhythmically active slices from neonatal mice brainstem preparations ($N = 9$). Sigh frequency can be determined from either the preBötC field recording or XII motor output. However, we only measure sigh magnitude from preBötC field recordings, since XII activity is filtered by premotor neuron processing postsynaptic from the preBötC. We bath applied 10 μM thapsigargin to partially block SERCA pumps of preBötC interneurons. In all cases, we observed an increase in sigh frequency (Figure 4.6B,C). On average sigh frequency increased from $0.80 \pm 0.48 \text{ min}^{-1}$ to $1.23 \pm 0.90 \text{ min}^{-1}$ (paired t-test, $p=0.04$), and returned to $0.8 \pm 0.42 \text{ min}^{-1}$ in washout. Consistent with our model, we also found sigh magnitude decreased by $32 \pm 0.16\%$ during drug application (Figure 4.6C). The effect on sigh frequency was completely reversible after washout, as was the effect on sigh area in most cases.

Next, we blocked SERCA pumps in the preBötC entirely, and selectively, by injecting 100 μM thapsigargin bilaterally into the preBötC. To verify our method of dual preBötC drug

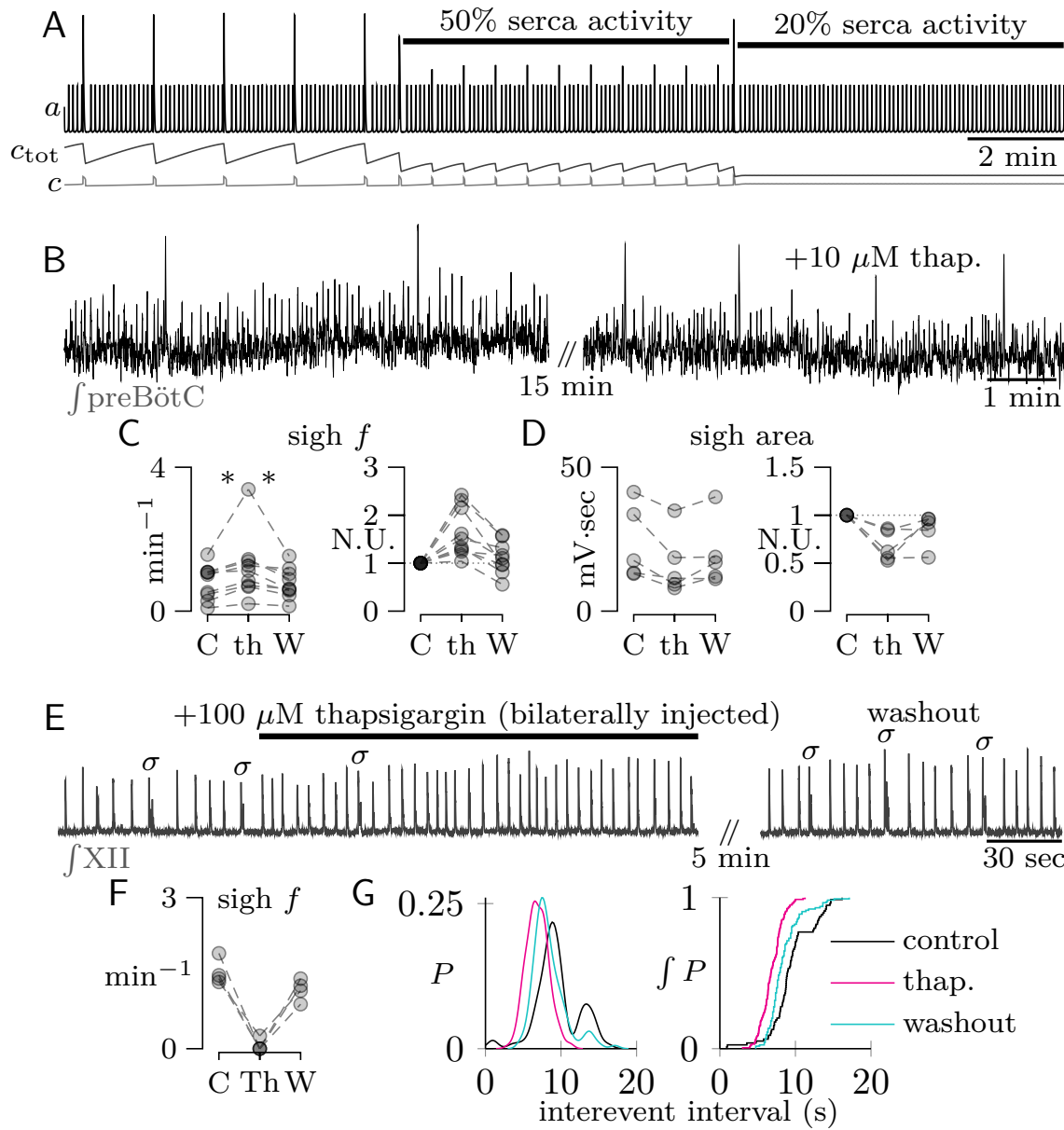


Figure 4.6: (Caption next page.)

application, we first puffed high (25 mM) K⁺ aCSF into both preBötC. This would locally increase excitability of preBötC interneurons, and indeed we saw a rapid and reversible increase inspiratory frequency (Figure 4.8). We also tested if 1% dimethylsulfoxide (DMSO) aCSF, the vehicle needed for 100 μM thapsigargin, would disturb preBötC rhythms but found no effect (Figure 4.8). When 100 μM thapsigargin was delivered to both preBötC via

bilateral injection, sigh frequency decreased (Figure 4.6D,E; N = 4). In three of four trials, sighs disappeared entirely during thapsigargin application. In the remaining experiment, sigh frequency dropped by 81%.

We quantified post-event intervals to further elucidate the presence or absence of sigh events. Sigh bursts are characterized by a post-sigh apnea, and in control distributions, these prolonged apneas manifest in the inter-event interval distribution as a second, delayed peak (Figure 4.6F). During 100 μ M thapsigargin application, the inter-event interval became entirely monophasic, suggesting all intervals were the same length and that sighs were not present or generating post-sigh apneas. The sigh rhythm recovered after sufficient washout. Additional experiments yielded identical results (Figure 4.8).

Figure 4.6: Investigating the role of SERCA pumps in sigh generation with modeling and pharmacology. A: Math model simulation of the inspiratory-sigh system with attenuated SERCA pumps (in the model, v_3 , see Section 4.5). Horizontal black bars indicate a parameter change. Scale bar is 2 minutes. B: preBötC field recordings are shown in blue, root recordings from XII motor nerve are shown in black. On the left is a slice in control conditions, on the right is 15 minutes after bath application of $10 \mu\text{M}$ thapsigargin. Scale bar is 1 minute. C: Group data showing average sigh frequency (f) during control, thapsigargin application, and washout. Each grey circle is one experiment from one slice, Grey circles connected by dashed lines show one slice over the course of the experiment ($N=9$). Normalized frequency is shown on the right, where sigh frequencies at each condition are normalized to the control frequency. The horizontal dotted line indicates a value of 1, or no change. N.U. is normalized units. C, T, and W stand for control, $10 \mu\text{M}$ thapsigargin, and washout respectively. D: Group data of integrated sigh area during control, thapsigargin, and washout conditions. Grey circles connected with dashed lines represent one slice over the course of the experiment ($N=5$). On the right are shown normalized values (N.U. is normalized units) where the average area is divided by the average area during control for that slice. E: XII root recording showing inspiratory and sigh rhythm. Sighs are highlighted with a , but can also be recognized by the increased area and post-sigh apnea. Black bars above data indicate application of $100 \mu\text{M}$ thapsigargin injected bilaterally into the preBötC. Scale bar is 30 seconds. F: Group data from the $100 \mu\text{M}$ thapsigargin studies, grey circles connected with dashed lines show one slice ($N=4$). Y axis is sigh frequency (f) in minutes $^{-1}$. Thap. is thapsigargin. G left: Distributions of inter-event intervals calculated during either control, $100 \mu\text{M}$ thapsigargin (thap), or washout. Interval time is measured in seconds. G right: Cumulative distributions of inter-event intervals.

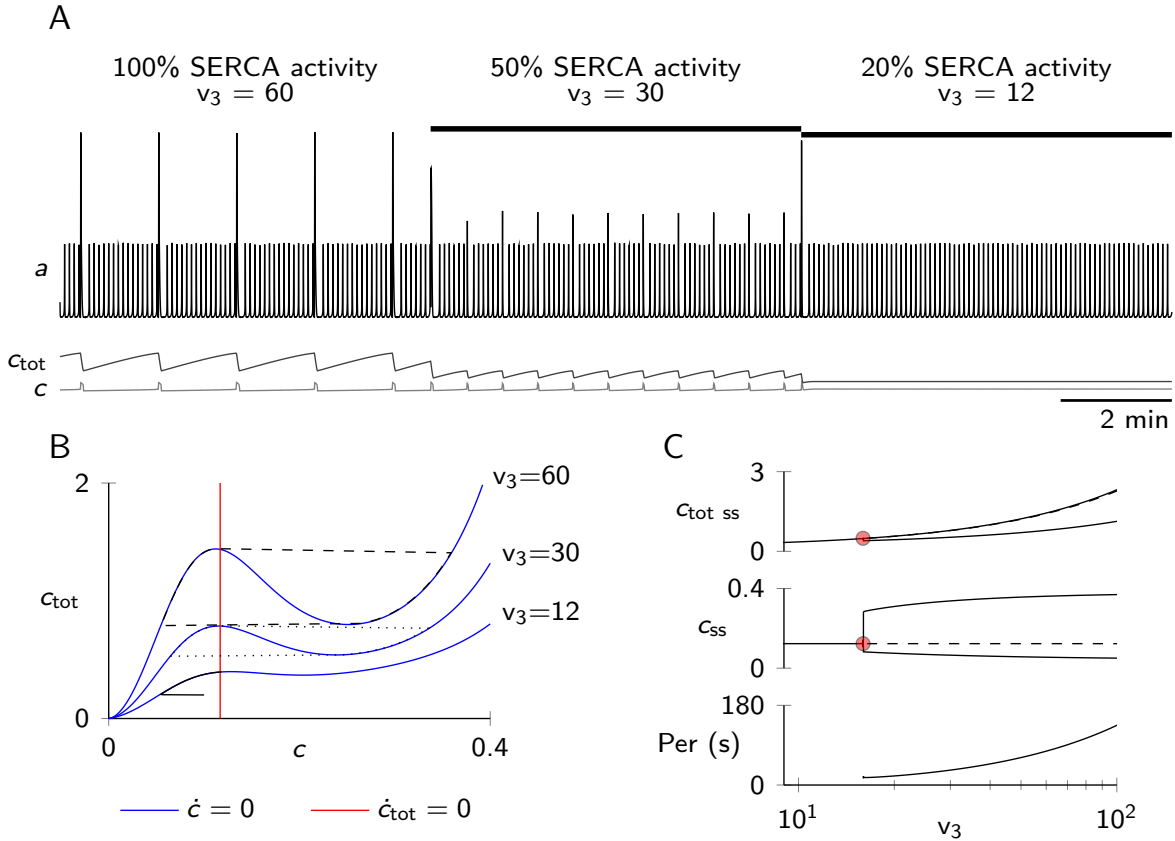


Figure 4.7: Model analysis of SERCA blockade. A, trajectories of network activity (a), cytosolic calcium concentration (c), and total calcium concentration (c_{tot}). Black bars show decrease in maximum rate of SERCA (v_3). B, phase plane. Cyan curves are the c nullclines for different values of v_3 . The red line is the c_{tot} nullcline. Dashed, dotted, and solid black curves are solutions for $v_3 = 60$, 30, and 12s^{-1} , respectively. For $v_3 = 60$ and 30s^{-1} , limit cycle oscillations are observed. For $v_3 = 12\text{s}^{-1}$ the system has a globally attracting steady state (filled circle). C, bifurcation analysis with maximum SERCA rate (v_3) as a bifurcation parameter. Filled red circles indicate Hopf bifurcations. Solid curves indicate stable steady states or, alternatively, the upper and lower values of a limit cycle oscillation. Dashed curves indicate unstable steady states. Bottom trace shows the period (T , in seconds) of the sigh rhythm as v_3 changes. The x axis is logarithmic.

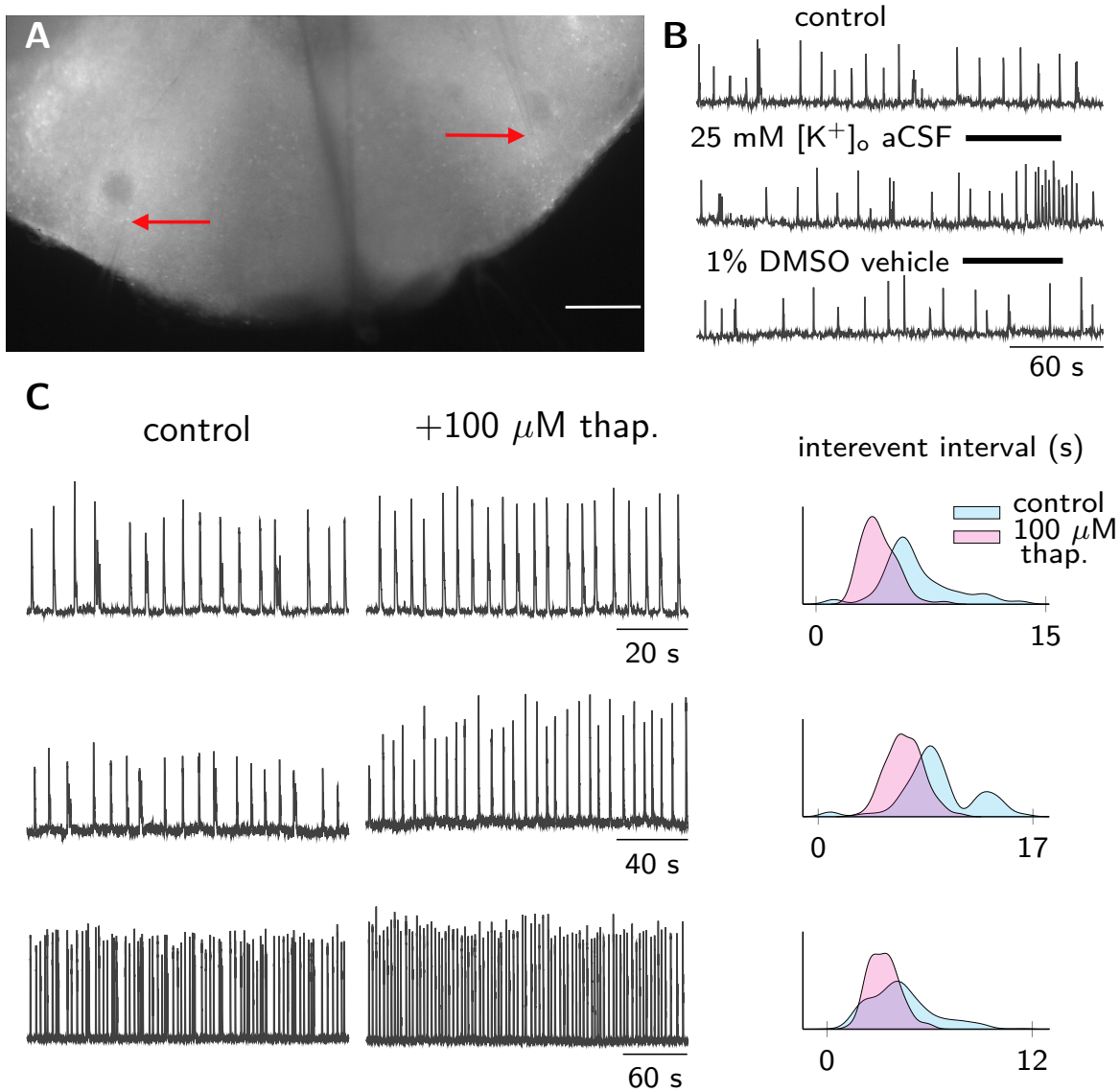


Figure 4.8: Validation of bilateral injection method and expanded results from SERCA blockade. A, image of the *in vitro* slice preparation. Red arrows indicate the tips of the two injector pipettes. Scale bar is 500 μm . B, XII root recordings of preBötC activity. Black bars above traces indicate bilateral injection into the preBötC. Scale bar is 60 seconds. C, representative traces from three slices that received 100 μM thapsigargin (thap.) injections. Control traces are on the left. Traces on the right were recorded during continuous thapsigargin application. Representative traces from each slice are shown at progressively slower sweep speeds. Histograms quantify the inter-event interval in seconds, counting any burst event (blue, control; red, thapsigargin).

4.2.7 Blocking IP₃R diminishes sigh rhythm frequency

While SERCA pumps move Ca²⁺ into the ER, IP₃R mediate Ca²⁺ efflux from the ER into the cytosol. Model predictions suggest that as IP₃R activity is attenuated, sigh rhythm frequency decreases (Figure 4.9A). The ER Ca²⁺ concentration threshold for a Ca²⁺-mediated Ca²⁺ release event is higher, therefore the system spends more time in a quiescent state and the frequency of the sigh oscillation decreases (Figure 4.10).

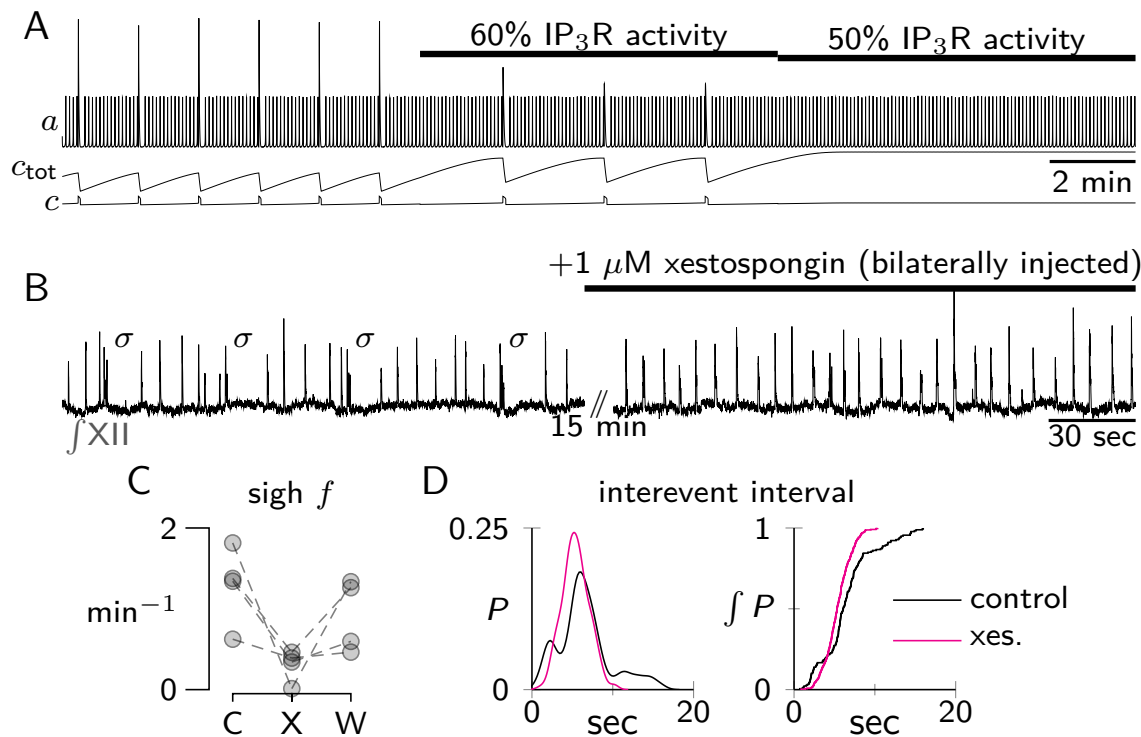


Figure 4.9: Investigating the role of IP₃ receptors in sigh generation with modeling and pharmacology. A: Inspiratory-sigh model trajectories, where *a*, c_{tot} , and c are network activity, total calcium in the cell, and calcium in the cytosol, respectively. Horizontal black bars represent a parameter change, in this case, v_1 – the maximum conductance through IP₃Rs (see Section 4.5). Scale bar is 2 minutes. B: XII root recording. The left trace is control conditions, sighs are highlighted with *a*, and can be recognized by the canonical post-sigh apnea. The right trace is after 15 minutes of 1 μM xestospongin injections, bilaterally delivered to both preBötC. Time scale is 30 seconds. C: Sigh frequency during control, after 15 minutes of 1 μM xestospongin (xes.) application, and after washout ($N=4$). Each grey dot and associated grey dashed lines are one slice preparation. D left: Distribution of the inter-event intervals before and during xestospongin (xes.) application. The x axis is the length of an inter-event interval in seconds. D right: Cumulative distribution of inter-event intervals.

We disrupted IP₃R activity experimentally with 1 μM xestospongin, a selective IP₃R

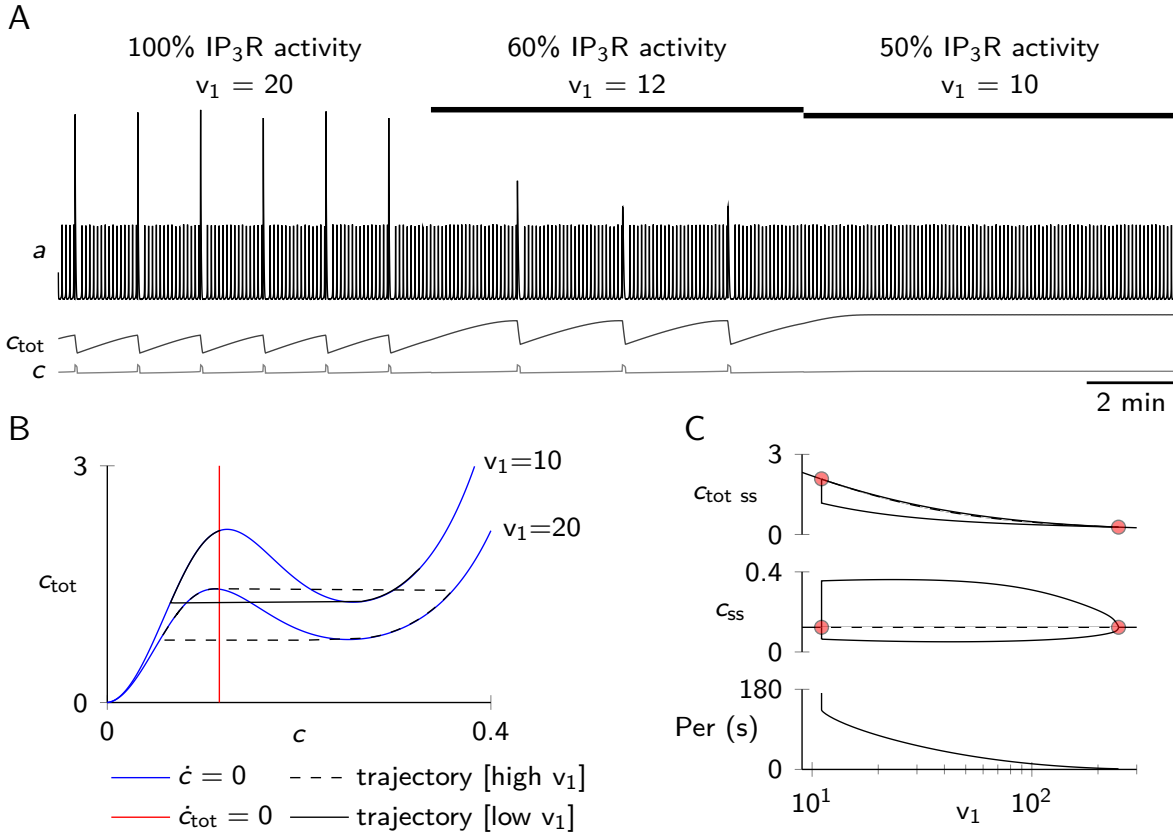


Figure 4.10: Model analysis on blockade of calcium release via IP₃R. A, trajectories of network activity (*a*), cytosolic calcium concentration (*c*), total cell calcium (*c_{tot}*). Black bars indicate a change in maximum IP₃R conductance (*v₁*). B, phase diagram of the calcium subsystem. Blue lines indicate the nullclines for the cytosolic calcium (*c*) for different values of *v₁*. The red line is the *c_{tot}* nullcline. The filled circle indicates the globally attracting steady state for *v₁* = 10 s⁻¹. The dashed black curve shows the limit cycle oscillation for *v₂* = 20 s⁻¹. C, bifurcation analysis with maximum IP₃R conductance (*v₁*) as the bifurcation parameter (see Figure 4.7C caption).

inhibitor (Gafni et al., 1997; Smet et al., 1999), injected bilaterally into the preBötC. We found a substantial decrease in sigh frequency during drug application (Figure 4.9). Average sigh frequency decreased from $1.29 \pm 0.49 \text{ min}^{-1}$ to $0.3 \pm 0.2 \text{ min}^{-1}$ ($N = 4$, Figure 4.9C). The effect was reversible in washout; sigh frequency returned to $0.91 \pm 0.48 \text{ min}^{-1}$.

To help verify the absence of sighs after drug application, we quantified inter-event interval during control and during xestospongin application (Figure 4.9D). During control, inter-event interval density peaks thrice. The earlier peak reflects very short inter-event intervals caused by the short time between a sigh and the preceding eupneic burst. The latest

peak reflects the presence of post-sigh apneas which are distinctly longer than intervals following inspiratory bursts. During application of xestospongin, both these distinct peaks in the inter-event interval distribution disappear, and the distribution becomes unimodally distributed, indicating the presence of a single burst type: inspiratory bursts. The cumulative distribution also describes the presence of sighs in control, and the dearth of them during xestospongin. While the xestospongin cumulative distribution is a clean sigmoidal, reminiscent of a normal distribution, the control curve plateaus twice, suggesting three clusters of inter-event intervals. Those three clusters of inter-event intervals correlate to the short time gap between an inspiratory burst and the sigh burst (< 1 s), the typical inter-event interval between two inspiratory bursts (≈ 8 s), and finally the post-sigh apnea (> 10 s).

4.3 Discussion

4.3.1 A Ca^{2+} based oscillator for sighs suggests excitatory synapses couple the inspiratory and sigh rhythms

We showed, with modeling and *in vitro* pharmacology, the importance of Ca^{2+} , and Ca^{2+} -transporters such as SERCA and IP_3R , in generating sigh events. This framework also provides further support to the idea that synaptic excitation couples the inspiratory and sigh rhythms, specifically the short delay between an inspiratory burst and the associated sigh event. During every inspiratory burst, Ca^{2+} enters the cell through voltage-dependent Ca^{2+} channels. Every one of these Ca^{2+} influxes provide a chance for the cytosolic Ca^{2+} concentration to reach the threshold required to initiation a Ca^{2+} -induced Ca^{2+} release event. This Ca^{2+} handoff would be enough to make sigh events more likely directly after

an inspiratory burst. As getting bumped over the threshold is more likely than surpassing it linearly and monotonically. The Ca^{2+} hypothesis for sigh rhythmogenesis reveals how the canonical sigh, of a sigh breath building off the crest of an inspiratory breath, emerges from the cellular origins.

The Ca^{2+} based model for sigh rhythmogenesis also reaffirms our understanding of the post-sigh apnea. We, and others, have postulated that the post-sigh apnea emerges because of an over recruitment of burst terminating mechanisms, which must reset before the next inspiratory event. In our model, Ca^{2+} from the Ca^{2+} -induced Ca^{2+} release event binds to I_{CAN} , which leads to an oversized burst event. The system must reset for a longer period; in our model, it is the cellular adaptation (θ) that takes longer to return to threshold. Cellular adaptation acts as the refractoriness of the network and sets the timing to the next inspiratory burst. Discovering the biophysical root for this refractoriness component of the model is an important future step for the field.

A caveat that must be addressed is our ability to classify events as inspiratory bursts and sigh bursts. Typically, we use burst area and the presence of a prolonged post-event apnea to determine if a burst is a sigh. In this study, we quantify post-event apnea to show statistically that the rhythm changes after pharmacological perturbation. Using this analysis, in hand with the classic sigh classification approach, we felt comfortable concluding the sigh rhythm had ceased. One possibility, however, is that the sigh rhythm itself is intact, but the pattern formation components are hampered so that the classic sigh shape does not manifest. We postulate that the sigh rhythm manifests in the network by activating Ca^{2+} -activated- Na^+ -currents (I_{CAN}). It is possible the Ca^{2+} oscillations are so diminished, that the release events do not generate a high enough concentration to activate I_{CAN} . These

missed sigh events would not increase activity in the cell during the subsequent burst event, and there would therefore be no post-sigh apnea.

4.3.2 Alternative biochemical sources for sigh rhythmogenesis

The sigh rhythm continues to emerge even after baseline excitability is reduced, and the inspiratory rhythm has ceased. This finding suggests that synaptic communication between neurons is not critical for maintaining the sigh rhythm. There are a few possible alternatives for the kernel of sigh rhythmogenesis. One idea, a vein we chose to investigate, was a glial source for the sigh rhythm. Knowing glia do not use synaptic connections to communicate, it is plausible they could maintain the rhythm while baseline excitability of the neurons was diminished. Alternative ideas include a biochemical oscillator, where the periodic change that drives a network-wide sigh burst is the concentration of a particular ion or molecule over time. While we reason, and show, that Ca^{2+} is a likely candidate for this biochemical oscillation, it is not unreasonable to implicate other actors in the molecular mechanisms underlying sigh generation.

4.3.3 Alternative paths for glia-driven sigh events

We tested the role of glial transmission in generating sigh events by blocking purinergic signaling. It is well known glia communicate to neurons through P2X and P2Y receptors with ATP as the extracellular messenger in the preBötC (Rajani et al., 2016, 2018; Reklow et al., 2019). We disrupted this pathway to study the importance of glia in generating sighs. We found no change in sigh rhythm amplitude or frequency, indicating that this glial transmission pathway is likely not critical for generating sigh events. However, there are

other pathways glia will use to communicate to themselves and neurons, which we did not address in this work. One of the more relevant mechanisms to our work is the ability for glia to sequester extracellular Ca^{2+} by releasing the Ca^{2+} binding protein $\text{S100}\beta$ (Morquette et al., 2015). In rhythmogenic networks, the decrease in free extracellular Ca^{2+} by $\text{S100}\beta$ has been shown to upregulate the activity of persistent sodium current (I_{NaP}), leading to an increase in rhythmic activity. We focused primarily on intracellular Ca^{2+} handling and did not explore the $\text{S100}\beta$ pathway in our work, however this pathway could be involved in sigh generation. If the sigh rhythm was generated in glia cells, either through a Ca^{2+} -dependent biochemical oscillator or another mechanism, the $\text{S100}\beta$ pathway could link the glial oscillation to the neuron-based inspiratory rhythm. Release of $\text{S100}\beta$ indirectly activates I_{NaP} , which might explain the oversized network-wide burst event during a sigh. However, the timescale for this process lasts on the order of seconds and would not account for the relatively short sigh burst event (< 1 s).

4.4 Appendix: Materials and Methods

Ethical approval and animal use

The Institutional Animal Care and Use Committee at William & Mary approved these protocols. These protocols conform to the policies of the Office of Laboratory Animal Welfare (National Institutes of Health, Bethesda, MD, USA) as well as the guidelines of the National Research Council (National Research Council (U.S.) et al., 2011). Mice (described below) were maintained on a 14-hour light/10-hour dark cycle at 23° C and were fed ad libitum with free access to water.

Many of the experiments require neural imaging of preBötC neurons derived from progenitors that express the embryonic transcription factor Developing brain homeobox 1 (i.e., Dbx1). The technique, multiphoton imaging (see below) requires the use of a Cre-driver mouse strain that was a homozygous knock-in mice generated by inserting an IRES-CRE-pGK-Hygro cassette in the 3 UTR of the Dbx1 gene, i.e., Dbx1Cre mice (Bielle et al., 2005) (IMSR Cat# EM:01924, RRID:IMSR_EM:01924).

We crossed females of the driver strain with males from a reporter strain featuring Cre-dependent expression of the fluorescent Ca²⁺ indicator GCaMP6f dubbed Ai148 by the Allen Institute (Daigle et al., 2018) (IMSR Cat# JAX:030328, RRID:IMSR_JAX:030328). We refer to their offspring as Dbx1;Ai148 mice. Throughout their life, Dbx1;Ai148 mice express GCaMP6f in Dbx1-derived cells, the majority of which are neurons (Kottick et al., 2017).

Breathing-related measurements *in vitro*

Mouse pups of both sexes were anesthetized by hypothermia and killed by thoracic transection at postnatal day 0 to 4. The neuraxis was removed in artificial cerebrospinal fluid (aCSF) containing (in mM): 124 NaCl, 3 KCl, 1.5 CaCl₂, 1 MgSO₄, 25 NaHCO₃, 0.5 NaH₂PO₄, and 30 dextrose equilibrated with 95% O₂-5% CO₂, pH 7.4. Isolated neuraxes were glued to an agar block and then cut in the transverse plane to obtain a single 500 μm-thick slice that exposed the preBötC at its rostral face. Atlases for wild-type and Dbx1 reporter mice show that the loop of the inferior olive and the semi-compact division of the nucleus ambiguus collocate with the preBötC during early postnatal development (Ruangkittisakul et al., 2011, 2014). Slices were then perfused with aCSF at 28° C in a recording

chamber below a fixed-stage microscope.

For control conditions, we elevated extracellular K⁺ concentration ([K⁺]_o) to 9 mM to increase preBötC excitability (Funk and Greer, 2013). Inspiratory-related motor output was recorded from the hypoglossal (XII) nerve rootlets, which are captured in transverse slices along with the XII motoneurons and their axon projections to the nerve rootlets, using suction electrodes and a differential amplifier. Field potentials were recorded from the preBötC by forming a seal over it with a suction electrode at the rostral slice surface. Amplifier gain was set at 1000. XII and preBötC bursts were full wave rectified and smoothed for display and quantitative analyses of burst events.

To locally apply 100 μM thapsigargin (CAS number 67526-95-8, Millipore Sigma, Burlington, MA) or 1 μM xestospongin C (CAS number 88903-69-9, Millipore Sigma), pipettes were fabricated from borosilicate glass (OD: 1.5 mm, ID: 0.86 mm) and filled with 9 mM K⁺ aCSF containing the respective drug. Dual pipettes were inserted 200 μm into both preBötC. Pressure pulses of 7–9 psi lasting 8 ms each were delivered at a frequency of 5–7 Hz. During experiments that required the presence of a puffing electrode to locally deliver drugs to the preBötC, acquiring a field recording was difficult and often impossible. Therefore, in those local drug delivery experiments, only recordings from XII nerve rootlets were employed.

Two-photon imaging

We imaged intracellular Ca²⁺ in neurons contained in slices from Dbx1;Ai148 mice using a two-photon laser-scanning microscope (Thorlabs, Newton, NJ) equipped with a Nikon water immersion 20×, 1.0 numerical aperture objective. Illumination was provided by an ultrafast tunable laser with a power output of 950 mW at 940 nm, 80-MHz pulse

frequency, and 100-fs pulse duration (Coherent Chameleon Discovery, Santa Clara, CA). We scanned Dbx1;Ai148 mouse slices over the preBötC and collected time series images at 15 Hz. Each frame reflects one-way raster scans with a resolution of 256 x 256 pixels (116 x 116 μm). Fluorescence data were collected using Thorlabs LS software and then analyzed using Fiji (Schindelin et al., 2012; Schneider et al., 2012), and MATLAB 2021a (MathWorks, Natick, MA, RRID:SCR_001622). Regions of interest were generated using methods previously described (Kallurkar et al., 2020).

Numerical simulations and data analysis

Modeling work was done in MATLAB 2021a (MathWorks, RRID:SCR_001622) and XPPAUT (Ermentrout, 2002). In MATLAB, numerical integrations were done using Eulers method with a time step of 0.01 ms. Integrations in XPP used the default solver settings. Information on model construction and design choice can be found in Section 4.5.

4.5 Appendix: Modeling of sigh rhythm and the coupling to eupnea

The model of eupnea and sigh rhythrogenesis (see Figure 4.11) below and Figure 4.5 of the main text) is an ordinary differential equation (ODE) system with five dynamical variables—three for the activity of the preBötC neuronal network (a , s , θ) and two for the dynamics of intracellular calcium in a representative neuron (c , c_{tot}). The differential

equations for the full model are

$$\tau_a \frac{da}{dt} = a_\infty(w \cdot s \cdot a - \theta, c) - a \quad (4.1)$$

$$\tau_s \frac{ds}{dt} = s_\infty(a) - s \quad (4.2)$$

$$\tau_\theta(a) \frac{d\theta}{dt} = \theta_\infty(a) - \theta \quad (4.3)$$

$$\frac{dc}{dt} = [v_1 f_\infty(c) + v_2] [c_{er} - c] - \frac{v_3 c^2}{\kappa_3^2 + c^2} + \jmath_0 + \jmath_1 a - \frac{v_4 c^4}{\kappa_4^4 + c^4} \quad (4.4)$$

$$\frac{dc_{tot}}{dt} = \jmath_0 + \jmath_1 a - \frac{v_4 c^4}{\kappa_4^4 + c^4}. \quad (4.5)$$

The algebraic functions a_∞ , s_∞ , θ_∞ and τ_θ that appear in the eupnea subsystem (Eqs. 4.1–4.3) are

$$a_\infty(x, c) = \frac{1}{1 + e^{4(\theta_a - x)/k_a}} + \frac{\lambda_c}{1 + e^{4(\theta_c - c)/k_c}} \quad (4.6)$$

$$s_\infty(x) = \frac{1}{1 + e^{4(\theta_s - x)/k_s}} \quad (4.7)$$

$$\theta_\infty(x) = \frac{1}{1 + e^{4(\theta_\theta - x)/k_\theta}} \quad (4.8)$$

$$\tau_\theta(x) = \frac{\tau_\theta^{max} - \tau_\theta^{min}}{1 + e^{4(\theta_{\tau_\theta} - x)/k_{\tau_\theta}}} + \tau_\theta^{min}. \quad (4.9)$$

The first dependent variable (a) is the network activity of the preBötC. This dimensionless quantity has been normalized by the maximum firing rate and takes values between 0 (no activity) and 1 (maximum activity). The dimensionless variables s and θ represent the dynamics of synaptic depression and cellular adaptation, respectively. The variable c represents the concentration of cytosolic free calcium. The variable c_{tot} is the total intracellular calcium concentration that includes contributions from the cytosol as well as intracellular calcium stores such as the endoplasmic reticulum. The algebraic functions that occur in the

calcium subsystem (Equations 4.4–4.5) are $c_{er} = (c_{tot} - c)/\lambda$ and

$$f_\infty(c) = \frac{1}{1 + e^{(\theta_m - c)/k_m}} \cdot \frac{1}{1 + e^{(\theta_h - c)/k_h}}. \quad (4.10)$$

See Tables 3.1,4.1 for a description of parameters and their standard values.

This Section describes the various components of this mathematical model with emphasis on the sigh rhythm. Section 4.5 presents the dynamical model of slow calcium oscillations that drives the sigh rhythm. Section 4.5 gives details regarding the coupling and interaction of these two subsystems and discusses how this mathematical model of the eupnea-sigh rhythm informed experimental work. For a refresher on the dynamics of the eupnea model subsystem, see Section 3.2, which focuses on the activity model of episodic bursting by the preBötC.

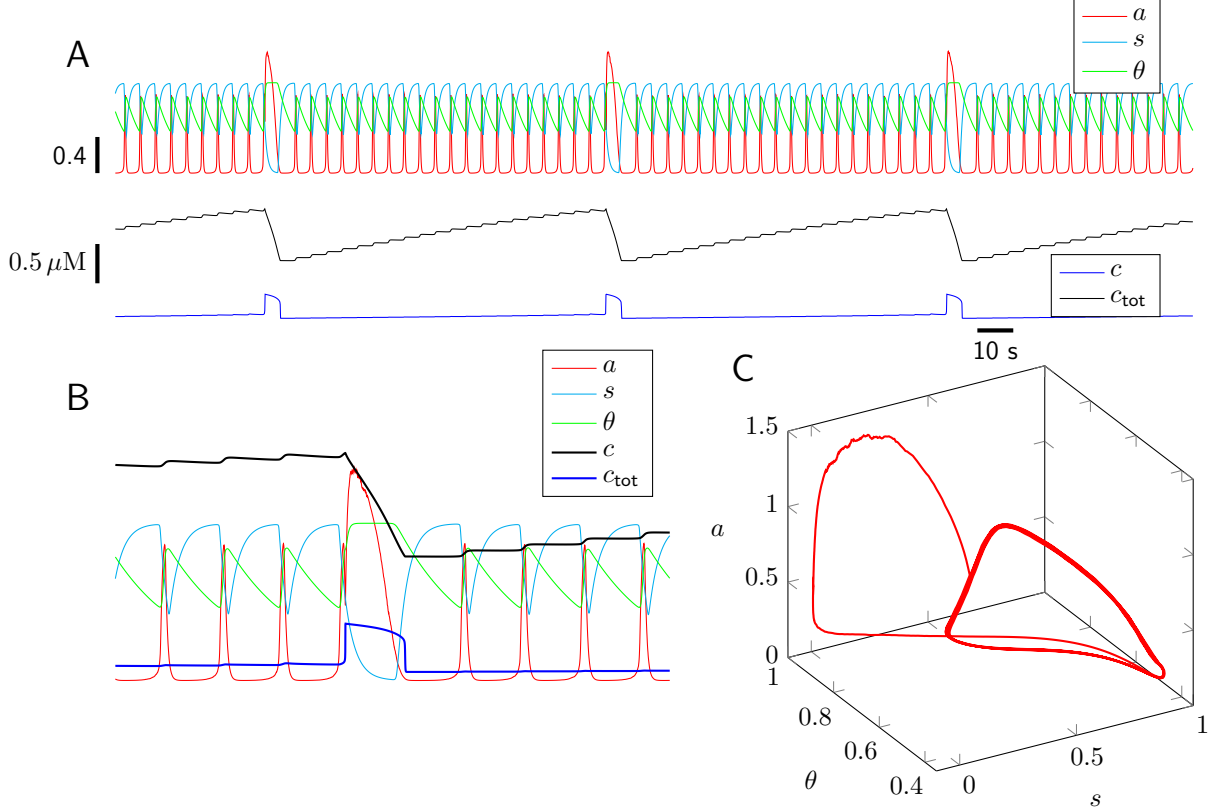


Figure 4.11: Representative simulation of the coupled eupnea and sigh rhythms. A, dynamics of the five dependent variables of the ODE model. B, expanded view that includes a single sigh event that emerges shortly after the onset of eupnea burst. C, three dimensional phase space for the (a, s, θ) subsystem.

Calcium handling and the sigh rhythm

Figure 4.11 shows a representative simulation of the coupled eupnea and sigh rhythms with three sigh events. These occur because eupnea subsystem (a, s, θ) is coupled to oscillatory dynamics for intracellular calcium (c, c_{tot}) that evoke a calcium-dependent increase in network activity (Equations 4.6). The calcium subsystem is the following two ODEs,

$$\frac{dc}{dt} = [v_1 f_\infty(c) + v_2] [c_{er} - c] - \frac{v_3 c^2}{\kappa_3^2 + c^2} + \jmath_0 + \jmath_1 a - \frac{v_4 c^4}{\kappa_4^4 + c^4} \quad (4.11)$$

$$\frac{dc_{\text{tot}}}{dt} = \jmath_0 + \jmath_1 a - \frac{v_4 c^4}{\kappa_4^4 + c^4}, \quad (4.12)$$

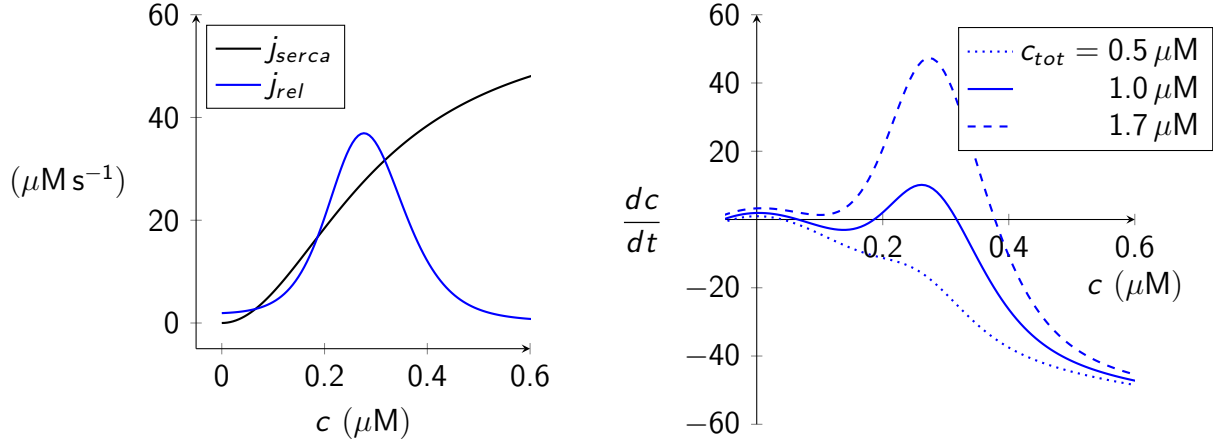


Figure 4.12: Phase diagram of closed cell model of calcium handling. Because plasma membrane fluxes are not included, c_{tot} is constant (see legend). Parameters as in Table 4.1.

where the variable c is the concentration of cytosolic free calcium, and c_{tot} is the total intracellular calcium concentration that includes contributions from the cytosol as well as intracellular calcium stores such as the endoplasmic reticulum. See Friel and Chiel (2008a); Keizer et al. (1995b) for review of calcium dynamics modeled in this fashion.

The parameters v_1 and v_2 are rate constants for calcium induced calcium release and a passive leak, both with a driving force given by the concentration gradient across the ER membrane ($c_{er} - c$). The parameter v_3 is the maximal activity of a SERCA-type reupdate flux given by a sigmoidal Hill-type expression with dissociation constant k_3 . The parameter v_4 is the maximal activity of for a sigmoidal expression representing extrusion of calcium mediated by plasma membrane calcium ATPases (PMCA). The terms $\gamma_0 + \gamma_1 a$ in Equations 4.11–4.12 representing calcium influx that is a linear function of the network activity a where γ_1 is a proportionality constant and γ_0 is the background rate of calcium influx.

The algebraic functions that occur in the calcium subsystem (Equations 4.11–4.12) are

$$c_{er} = (c_{tot} - c)/\lambda \text{ and}$$

$$f_\infty(c) = \frac{1}{1 + e^{(\theta_m - c)/k_m}} \cdot \frac{1}{1 + e^{(\theta_h - c)/k_h}}. \quad (4.13)$$

Table 4.1: Standard parameters for calcium subsystem. The units of network activity, denoted by [a] in the table, are spikes per second per cell.

Symbol	Definition	Value	Units
v_1	rate constant of calcium release	20	s^{-1}
v_2	rate constant of calcium leak	0.25	s^{-1}
v_3	maximum rate of SERCA pumps	60	$\mu\text{M s}^{-1}$
k_3	half maximum for SERCA pumps	0.3	μM
λ	ER/cytosol effective volume ratio	0.15	-
θ_m	activation of intracellular calcium channels	0.25	μM
k_m	reciprocal of slope of m_∞ at half maximum	0.04	μM^{-1}
θ_h	activation of intracellular calcium channels	0.3	μM
k_h	reciprocal of slope of h_∞ at half maximum	-0.06	μM^{-1}
j_0	constant calcium influx rate	0.009	$\mu\text{M s}^{-1}$
j_1	calcium influx rate proportionality constant	0.02	$\mu\text{M s}^{-1}$
v_4	maximum rate of PMCA pumps	0.4	$\mu\text{M s}^{-1}$
k_4	half maximum for PMCA pumps	0.3	μM

This first expression follows from the definition of total cell calcium (expressed as a concentration using the cytosolic volume), that is, $c_{tot} = c + \lambda c_{er}$ where λ is the effective volume ratio accounting for compartment size and buffering capacity of the cytosol and ER. The function $f_\infty(c)$ represents the well-known bell-shaped dependence of the steady-state IP₃R open probability as a function of cytosolic calcium concentration. In Equation 4.13 this bell-shaped dependence emerges as the product of sigmoidal functions representing IP₃R activation ($k_m > 0$, so the first factor is an increasing function of c) and inactivation ($k_h < 0$, the second factor is decreasing). Table 4.1 lists the standard parameters for the calcium subsystem (Equations 4.11–4.13).

Bistability in a closed cell model of calcium handling

The relaxation oscillator dynamics of the calcium subsystem that drive the sigh rhythm can be understood by considering the phase diagram for the cytosolic calcium concentration (the fast variable) for fixed values of total cell calcium (the slow variable). The phase diagram

for this closed cell (i.e., plasma membrane fluxes are not included) is a plot of the right side of Equation 4.11, denoted by $h(c)$ below:

$$\frac{dc}{dt} = h(c) = [v_1 f_\infty(c) + v_2] \left(\frac{c_{tot} - c}{\lambda} - c \right) - \frac{v_3 c^2}{k_3^2 + c^2}. \quad (4.14)$$

Using three different values for c_{tot} and other parameters from Table 4.1, Figure 4.12 plots the right hand side of this scalar differential equation (h) as a function of the dependent variable (c). For intermediate values of c_{tot} (solid blue curve), the function $h(c)$ intersects the horizontal axis three times. Noting the slopes $h'(c)$ evaluated at these three steady states, it is clear that the lower- and uppermost steady states are stable while the third steady state (located between these) is unstable.

Relaxation oscillations in open cell model of calcium handling

In the full model of coupled eupnea and sigh rhythms (Equations 4.1–4.5), the fluxes representing calcium release and reuptake from the ER (Equation 4.14) are augmented by plasma membrane fluxes, $J_{pm} = J_{in} - J_{out}$ where $J_{in} = \gamma_0 + \gamma_1 a$ and $J_{out} = v_4 c^4 / (\kappa_4^4 + c^4)$. By averaging the calcium influx over cycles of episodic bursting with period T , one may calculate an effective calcium influx rate, given by

$$\gamma_{avg} = \frac{1}{T} \int_0^T [\gamma_0 + \gamma_1 a(t)] dt, \quad (4.15)$$

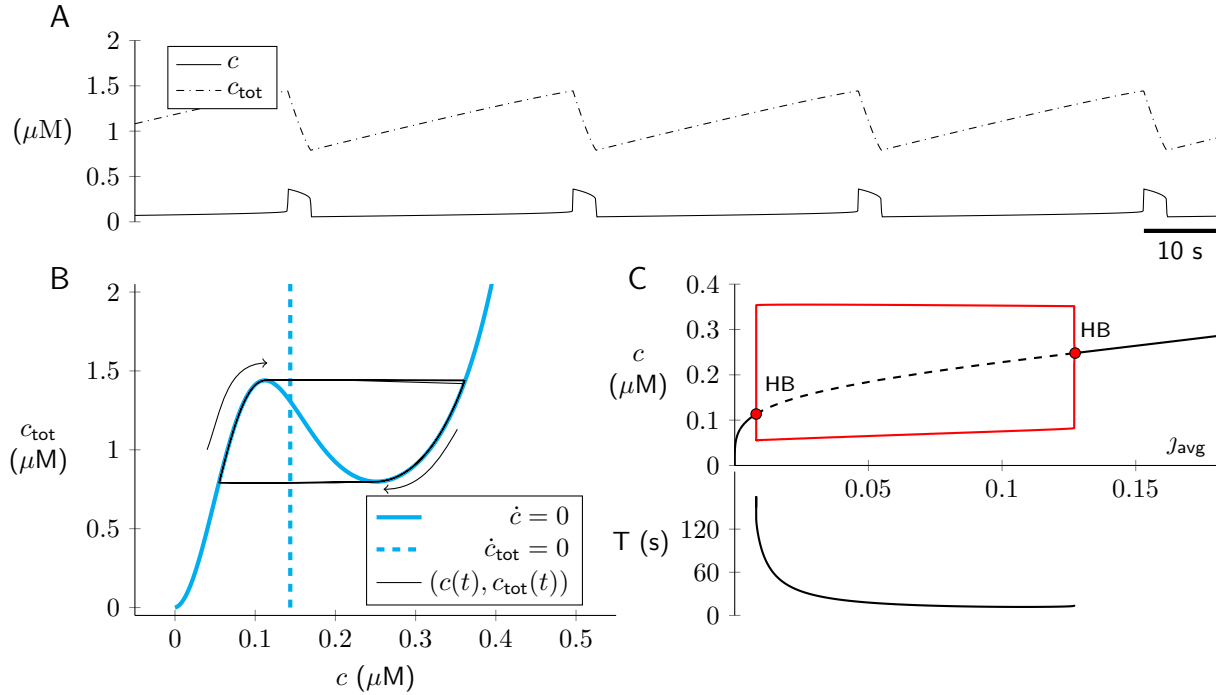


Figure 4.13: Open cell calcium dynamics given by solution of Equations 4.16–4.17 with parameters as in Table 4.1. A, type 2 relaxation oscillations (c fast, c_{tot} slow). B, phase plane, with c and c_{tot} nullclines (green and red, respectively) and periodic solution (blue). C, bifurcation diagram with average calcium influx rate (j_{avg}) as bifurcation parameter (see Figure 3.3 caption).

that no longer depends on the network activity (a). The resulting open cell model is

$$\frac{dc}{dt} = [v_1 f_\infty(c) + v_2] [c_{er} - c] - \frac{v_3 c^2}{\kappa_3^2 + c^2} + j_{avg} - \frac{v_4 c^4}{\kappa_4^4 + c^4} \quad (4.16)$$

$$\frac{dc_{tot}}{dt} = j_{avg} - \frac{v_4 c^4}{\kappa_4^4 + c^4} \quad (4.17)$$

Figure 4.13 (top) shows the relaxation oscillator dynamics of this open cell model using standard parameters (Table 4.1) and $j_{avg} = 0.009 \mu\text{M s}^{-1}$. The oscillation period is on the order of minutes and the system spends most of its time in the *down* state with low cytosolic calcium ($0.05\text{--}0.1 \mu\text{M}$) and slowly increasing total cell calcium, c_{tot} (and slowly increasing ER calcium, because $c_{er} = (c_{tot} - c)/\lambda$). The phase plane of Figure 4.13 (bottom left) shows the c and c_{tot} nullclines that are found by setting the left sides of Equations 4.16–4.17 to

zero. The c nullcline is “cubic” in shape and has two extrema (knees). The c_{tot} nullcline is a vertical line located at the value of c which solves $\jmath_{avg} = v_4 c^4 / (\kappa_4^4 + c^4)$.

Note how the separation of time scales for c and c_{tot} leads to a periodic solution (blue trajectory) that tracks the lower or upper branch of the c nullline except for two brief excursions between branches when the trajectory passes over a “knee” of the cubic c nullcline. Figure 4.13 (bottom right) shows a bifurcation diagram for Equations 4.16–4.17. Type 2 relaxation oscillations that originate via Hopf bifurcations are observed for a wide range of average calcium influx rates (\jmath_{avg}). Given the separation of time scales, oscillations occur for any value of \jmath_{avg} that causes the c_{tot} nullline to intersect the c_{tot} nullline between the knees.

Coupling of the eupnea and sigh rhythms

The model of eupnea rhythmogenesis (a, s, θ) and calcium handling (c, c_{tot}) are bidirectionally coupled in a manner that creates the eupnea/sigh dynamics of Figure 4.11A. Episodic network activity (a) influences dynamics of intracellular calcium via the plasma membrane influx rate $J_{in} = \jmath_0 + \jmath_1 a$ (Equations 4.4–4.5). The concentration of cytosolic calcium influences network activity (a) through the steady-state activity function $a_\infty(w \cdot s \cdot a - \theta, c)$ in Equation 4.1, that is,

$$a_\infty(a, s, \theta, c) = \frac{1}{1 + e^{4(\theta_a + \theta - wsa)/k_a}} + \frac{\lambda_c}{1 + e^{4(\theta_c - c)/k_c}} \quad (4.18)$$

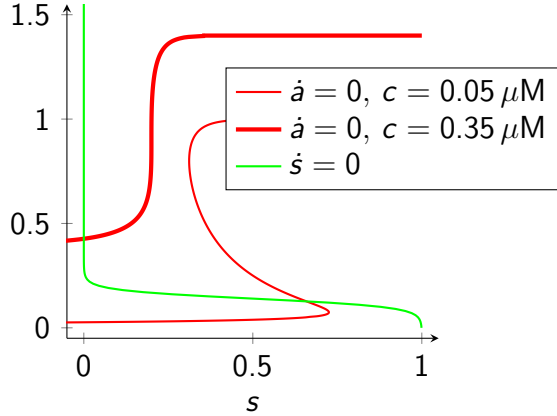


Figure 4.14: The influence of cytosolic calcium concentration on the steady-state network activity (Eqs. 4.18–4.19). Parameters: $\lambda_c = 0.8$, $\theta_c = 0.35$, $k_c = 0.05$. This gives $a_+(c) \approx 0$ and 0.4 for $c = 0.05 \mu\text{M}$ and $0.35 \mu\text{M}$, respectively. Other parameters as in Tables 3.1,4.1.

Writing $a_+(c) = \lambda_c(1 + e^{4(\theta_c - c)/k_c})^{-1}$ for the calcium dependent term, an explicit formula for the a nullcline is given by

$$a \text{ nullcline: } s = \frac{4(\theta_a + \theta) - k_a \ln \left[\frac{1}{a - a_+(c)} - 1 \right]}{4w_a}. \quad (4.19)$$

Fig. 4.14 uses this expression to show how the network activity nullcline ($\dot{a} = 0$) shifts upwards during the active phase of the calcium oscillation, i.e., cytosolic calcium concentration is elevated subsequent to ER calcium release (Figure 4.13B, upper branch of c nullcline). In the full model of eupnea and sigh rhythmogenesis, the larger of the two loops of the trajectory in the 3d phase space is a consequence of the boost in network activity mediated by cytosolic calcium (Figure 4.11C).

Chapter 5

Conclusion and Discussion

Brain rhythms impact nearly every animal behavior, from locomotor activities to cognitive tasks. Breathing requires the coordination of several rhythms, such as inspiration and sighs, as discussed in this work, but also expiration when exercising, and gasping. The patterning of these rhythms changes for activities such as vocalizing, eating, or swimming, which demand augmented breathing patterns. Understanding the neural origin of the breathing rhythms is a worthy goal for neuroscience, because understanding how different rhythms operate and coordinate their timing in an observable motor activity will aid in understanding the origins of, and interactions between, higher order brain activities. For example, learning and memory consolidation during REM sleep is known to involve the entertainment and coupling of theta waves and high frequency gamma oscillations (Buzsáki and Wang, 2012; Montgomery et al., 2008).

The preBötC of the ventral medulla generates two rhythms simultaneously, eupnea and sighs. Therefore, it represents a convenient system to study how two rhythms emerge from one group of neurons and how those rhythms might interact or remain independent.

The aim of Chapter 2 was to investigate the coupling between the eupnea (inspiratory) and sigh rhythms. Previous work suggested that synaptic inhibition was the primary mechanism by which the inspiratory rhythm communicated to the sigh rhythm, thereby producing the typically short (≈ 1 s) delay between a sigh and its preceding inspiration (Chapuis et al., 2014; Lieske et al., 2000; Toporikova et al., 2015). I set out to validate these results, but found the opposite response – that synaptic inhibition was not responsible for coupling either rhythm to the other. In fact, without synaptic inhibition the sigh was more tightly coupled to the preceding inspiratory burst.

This observation led to the primary conclusion – that synaptic excitation was responsible for linking the sigh to the preceding burst event. The preBötC is a heterogeneous collection of excitatory and inhibitory interneurons. During a burst event, there is a combination of excitatory and inhibitory post-synaptic potentials, that counteract one another, where ultimately excitation is the stronger, but inhibition acts as a clamp to control the size of the burst event (Baertsch et al., 2018). If excitation and inhibition are balanced, then blocking fast synaptic inhibition from the system is akin to tilting the scales more heavily towards excitation. Thus, it is reasonable to propose that the effect we observed, where the timing between the inspiratory and sigh bursts decreased (Figure 2.2), was the result of synaptic scales tilting towards more excitation in the system. It would follow then that synaptic excitation is responsible for coupling the sigh rhythm to the inspiratory rhythm.

Another finding that supports the hypothesis that synaptic excitation links the sigh to the inspiratory burst is the reversal of the polarity of chloride-mediated currents during development, from excitatory in embryonic development to inhibitory after the first day of birth ($\approx P0$) (Figure 2.6). During embryonic development, the dominant expression of the

cotransporter NKCC1 in brainstem and spinal cord neurons elevates intracellular chloride concentration (Delpy et al., 2008; Ren and Greer, 2006; Viemari et al., 2011), ensuring the chloride-mediated currents are inward (excitatory) at baseline membrane potential. Perinatally, NKCC1 expression decreases, while expression of the chloride symporter KCC2, which lowers intracellular chloride concentration, increases. In mature animals, dominant KCC2 expression ensures that the chloride equilibrium potential is more hyperpolarized than baseline membrane potential; chloride currents are outward (inhibitory). I meta-analyzed eight studies that recorded chloride equilibrium potentials in mice and rats around P0, and found the chloride equilibrium switches from excitatory from inhibitory around the day of birth (P0).

For one, this meta analysis indicates we were truly blocking inhibition in our neonatal preparations (P1–P4). For another, the analysis finds that two of the previous groups (Chapuis et al., 2014; Toporikova et al., 2015) were not blocking inhibition with glycinergic receptor antagonists, but rather blocking chloride-mediated excitation, as they both used an embryonic preparation. That work represents a unique chance to block some synaptic excitation in the system, but without interrupting inspiratory rhythm generation. When analyzed with this information, their data finds blocking synaptic excitation decoupled the sigh from the preceding inspiratory burst, and caused the sigh rhythm to become free running. This finding, along with our work blocking synaptic inhibition in the preBötC of neonatal mice, implicates synaptic excitation as the primary link between the inspiratory rhythm and the sigh rhythm.

Chapter 3 explored the preinspiratory phase of the inspiratory rhythm. We developed a mean field model, referred to as the activity-based model, of inspiratory rhythmogenesis

whereby recurrent excitation and synaptic depression lead to oscillations in network activity. This model helped me understand that the preinspiratory phase must be mechanistically distinct from the postinspiratory phase. With the activity-based model, we showed that synaptic depression and recurrent excitation alone are not enough to generate an accurate model of the inspiratory rhythm. If the burst events occurred before synaptic depression could completely recover, then the timing between the events was normally distributed (like the biology), but the size of the burst events was positively correlated to the duration of the preceding inter-event interval (unlike the biology). If synaptic depression was allowed to recover, and noise in the activity triggered the burst events, then the size of the burst events would be uncorrelated to the preceding interval (like the biology), but the timing between events was exponentially distributed (unlike the biology). There must be a third slow variable that sets the time for the preinspiratory phase. Whereas synaptic depression sets the time for the postinspiratory phase, this unknown third component determined the length of the preinspiratory phase.

In our augmented model of inspiratory rhythmogenesis, we included a dynamic threshold for recurrent activity that slowly recovered. That is, the threshold for activity decreased, as time went on, and was reset after a burst event. We would use this activity based model later in the sigh rhythm project.

To gain a better understanding of the preinspiratory phase, and because the details of the mechanism may depend on network dynamics that the activity (firing rate) model overlooks, we developed a network-based model of coupled oscillators that generated rhythmic burst events via recurrent excitation and synaptic depression. Again, we found those two components were not enough to build an accurate model of inspiratory rhythm generation.

Without a time-dependent third variable, one that would not impact the size of the burst event, the system had the same deficiency as described in the firing rate model. Thus, a major finding from Chapter 3 was that our observation from the activity-based model, that the preinspiratory phase must depend on an additional component, besides burst terminating mechanisms, was confirmed again by the network-based model.

Using the network-based model, we explored how network topology could impact the duration of the preinspiratory phase of inspiratory rhythm generation. We tested four well known topologies, and showed each produce a rhythm with only slightly different preinspiratory phases. However, we also showed that each topology influences the way rhythmogenesis breaks down after losing some fraction of the network's constitutive neurons. Finally, we quantify how a single large component arises in networks with different underlying interconnectivity at a distinct rate, and we suggest this feature ultimately influences the way activity builds in the network-based model. My second major finding from this project was that network topology does impact the way activity spreads in the network, but we did not find enough evidence to suggest recurrent excitation in a specific network-firing topology is the primary mechanism underlying the preinspiratory phase of inspiration.

In Chapter 4, we discovered how the sigh rhythm is generated in the preBötC, and how the sigh circuitry can operate independently from the mechanisms that drive inspiration. We propose the sigh rhythm is generated by intracellular Ca^{2+} oscillations in the preBötC interneurons. Then, using a mathematical model alongside *in vitro* electrophysiology, we test key components of this pathway and ultimately conclude our hypothetical framework for sigh rhythmogenesis cannot be rejected based on our test.

Thus, one major finding from Chapter 4 is that intracellular Ca^{2+} oscillations drive

sigh events. Our proposed pathway begins with Ca^{2+} entering the cell, either passively or via activity-dependent mechanisms such as voltage-gated Ca^{2+} channels on the membrane of the soma. Most of the Ca^{2+} is sequestered into the ER, or other Ca^{2+} sequestering organelles, while a smaller fraction builds in the cytosol. This build up takes several minutes, until cytosolic Ca^{2+} reaches a critical concentration where it binds to IP_3 receptors on the membrane of the ER, and triggers Ca^{2+} release. This begins a positive feedback loop, where Ca^{2+} leaves the ER and binds to additional IP_3 receptors, leading to more Ca^{2+} release. This phenomenon is known as Ca^{2+} -induced- Ca^{2+} release. The excessive Ca^{2+} dump into the cytosol is quickly expelled from the cell by Ca^{2+} pumps, but before the ion concentration drops, it activates Ca^{2+} -activated nonspecific inward currents (I_{CAN}), thus leading to a large depolarization that drives an over sized burst event – the sigh burst.

This discovery leads to the second major finding of this work: how one population of neurons can drive two rhythms of different frequency and magnitude. An individual neuron contributes its synaptic communication hardware, such as action-potential-generating membrane currents and vesicle release, to the inspiratory oscillations. Meanwhile, the neuron undergoes an entirely separate oscillation that depends on ER Ca^{2+} concentrations and cytosol Ca^{2+} concentrations in the soma, and which occurs on the order of minutes. These two oscillations can, and do, interact, but they can also run entirely separate from one another. The rhythms are housed in the same population by harnessing two separate capabilities of the neurons: recurrent synaptic communication and intracellular Ca^{2+} dynamics.

Rhythms are involved in nearly every brain process. Breathing, in particular, offers the chance to study two rhythms, generated in parallel, that are different in magnitude and frequency from one another. By uncovering the disparate cellular mechanisms that

drive inspiratory and sigh rhythms simultaneously in the same neurons, we reveal a possible medium for how multiple distinct rhythms can coexist throughout the brain.

References

- Alsahafi, Z, Dickson, C. T, and Pagliardini, S. (2015). Optogenetic excitation of preBötzinger complex neurons potently drives inspiratory activity *in vivo*: PreBötzinger complex optostimulation. *The Journal of Physiology*, 593(16):3673–3692. doi: 10.1113/JP270471.
- Ashhad, S and Feldman, J. L. (2020). Emergent elements of inspiratory rhythmogenesis: network synchronization and synchrony propagation. *Neuron*, 106(3):482–497.e4. doi: 10.1016/j.neuron.2020.02.005.
- Baertsch, N. A and Ramirez, J.-M. Insights into the dynamic control of breathing revealed through cell-type-specific responses to substance P. preprint, Neuroscience, (2019).
- Baertsch, N. A, Baertsch, H. C, and Ramirez, J. M. (2018). The interdependence of excitation and inhibition for the control of dynamic breathing rhythms. *Nature Communications*, 9 (1):843. doi: 10.1038/s41467-018-03223-x.
- Barabási, A.-L. (2018). Clauset’s fruitless search for scale-free networks. *Barabasi Lab Blog*.
- Barabasi, A.-L and Albert, R. (1999). Emergence of scaling in random networks. 286:4.
- Barry, P. H and Lynch, J. W. (1991). Liquid junction potentials and small cell effects in patch-clamp analysis. *The Journal of Membrane Biology*, 121(2):101–117. doi: 10.1007/BF01870526.
- Berne, R. M, Levy, M. N, and Koeppen, B. M. (2008). *Berne & Levy Physiology*. Elsevier Brasil.

- Bielle, F, Griveau, A, Narboux-Nême, N, Vigneau, S, Sigrist, M, Arber, S, Wassef, M, and Pierani, A. (2005). Multiple origins of Cajal-Retzius cells at the borders of the developing pallium. *Nature Neuroscience*, 8(8):1002–1012. doi: 10.1038/nn1511.
- Borrus, D. S, Grover, C, Conradi Smith, G. D, and Del Negro, C. A. (2020). Role of synaptic inhibition in the coupling of the respiratory rhythms that underlie eupnea and sigh behaviors. *eNeuro*, 7(3). doi: 10.1523/ENEURO.0302-19.2020.
- Bouvier, J, Thoby-Brisson, M, Renier, N, Dubreuil, V, Ericson, J, Champagnat, J, Pierani, A, Chédotal, A, and Fortin, G. (2010). Hindbrain interneurons and axon guidance signaling critical for breathing. *Nature Neuroscience*, 13(9):1066–1074. doi: 10.1038/nn.2622.
- Branchereau, P, Morin, D, Bonnot, A, Ballion, B, Chapron, J, and Viala, D. (2000). Development of lumbar rhythmic networks: from embryonic to neonate locomotor-like patterns in the mouse. *Brain Research Bulletin*, 53(5):711–718. doi: 10.1016/S0361-9230(00)00403-2.
- Brockhaus, J and Ballanyi, K. (1998). Synaptic inhibition in the isolated respiratory network of neonatal rats: Synaptic inhibition in neonatal respiratory neurons. *European Journal of Neuroscience*, 10(12):3823–3839. doi: 10.1046/j.1460-9568.1998.00396.x.
- Broido, A. D and Clauset, A. (2019). Scale-free networks are rare. *Nature Communications*, 10(1):1017. doi: 10.1038/s41467-019-08746-5.
- Butera, R. J, Rinzel, J, and Smith, J. C. (1999). Models of respiratory rhythm generation in the pre-Bötzinger Complex. I. Bursting pacemaker neurons. *Journal of Neurophysiology*, 82(1):382–397. doi: 10.1152/jn.1999.82.1.382.
- Buzsaki, G. (2006). *Rhythms of the Brain*. Oxford University Press. ISBN 978-0-19-804125-2.
- Buzsáki, G and Wang, X.-J. (2012). Mechanisms of gamma oscillations. *Annual Review of Neuroscience*, 35(1):203–225. doi: 10.1146/annurev-neuro-062111-150444.
- Cammarota, G, Vaschetto, R, Turucz, E, Dellapiazza, F, Colombo, D, Blando, C, Della Corte, F, Maggiore, S. M, and Navalesi, P. (2011). Influence of lung collapse distribu-

- tion on the physiologic response to recruitment maneuvers during noninvasive continuous positive airway pressure. *Intensive Care Medicine*, 37(7):1095–1102. doi: 10.1007/s00134-011-2239-8.
- Canavier, C. C and Achuthan, S. (2010). Pulse coupled oscillators and the phase resetting curve. *Mathematical Biosciences*, 226(2):77–96. doi: 10.1016/j.mbs.2010.05.001.
- Chapuis, C, Autran, S, Fortin, G, Simmers, J, and Thoby-Brisson, M. (2014). Emergence of sigh rhythmogenesis in the embryonic mouse: Sigh in mouse embryo. *The Journal of Physiology*, 592(10):2169–2181. doi: 10.1113/jphysiol.2013.268730.
- Charles, A. C. (1994). Glia-neuron intercellular calcium signaling. *Developmental Neuroscience*, 16(3-4):196–206. doi: 10.1159/000112107.
- Cherniack, N. S, Euler, C, Glogowska, M, and Homma, I. (1981). Characteristics and rate of occurrence of spontaneous and provoked augmented breaths. *Acta Physiologica Scandinavica*, 111(3):349–360. doi: 10.1111/j.1748-1716.1981.tb06747.x.
- Clark, F. J and von Euler, C. (1972). On the regulation of depth and rate of breathing. *The Journal of Physiology*, 222(2):267–295. doi: 10.1113/jphysiol.1972.sp009797.
- Clauset, A, Shalizi, C. R, and Newman, M. E. J. (2009). Power-law distributions in empirical data. *SIAM Review*, 51(4):661–703. doi: 10.1137/070710111.
- Conradi Smith, G. D. (2019). *Cellular Biophysics and Modeling: A Primer on the Computational Biology of Excitable Cells*. Cambridge University Press.
- Crill, W. E. (1996). Persistent sodium current in mammalian central neurons. *Annu. Rev. Physiol.*, (58):349–62.
- Cui, Y, Kam, K, Sherman, D, Janczewski, W. A, Zheng, Y, and Feldman, J. L. (2016). Defining preBötzinger Complex Rhythm- and Pattern-Generating Neural Microcircuits In Vivo. *Neuron*, 91(3):602–614. doi: 10.1016/j.neuron.2016.07.003.

- Daigle, T. L, Madisen, L, Hage, T. A, Valley, M. T, Knoblich, U, Larsen, R. S, Takeno, M. M, Huang, L, Gu, H, Larsen, R, Mills, M, Bosma-Moody, A, Siverts, L. A, Walker, M, Graybuck, L. T, Yao, Z, Fong, O, Nguyen, T. N, Garren, E, Lenz, G. H, Chavarha, M, Pendergraft, J, Harrington, J, Hirokawa, K. E, Harris, J. A, Nicovich, P. R, McGraw, M. J, Ollerenshaw, D. R, Smith, K. A, Baker, C. A, Ting, J. T, Sunkin, S. M, Lecoq, J, Lin, M. Z, Boyden, E. S, Murphy, G. J, da Costa, N. M, Waters, J, Li, L, Tasic, B, and Zeng, H. (2018). A suite of transgenic driver and reporter mouse lines with enhanced brain-cell-type targeting and functionality. *Cell*, 174(2):465–480.e22. doi: 10.1016/j.cell.2018.06.035.
- Del Negro, C. A. (2005). Sodium and calcium current-mediated pacemaker neurons and respiratory rhythm generation. *Journal of Neuroscience*, 25(2):446–453. doi: 10.1523/JNEUROSCI.2237-04.2005.
- Del Negro, C. A, Koshiya, N, Butera, R. J, and Smith, J. C. (2002). Persistent sodium current, membrane properties and bursting behavior of pre-Bötzinger Complex inspiratory neurons *in vitro*. *Journal of Neurophysiology*, 88(5):2242–2250. doi: 10.1152/jn.00081.2002.
- Del Negro, C. A, Morgado-Valle, C, and Feldman, J. L. (2002). Respiratory rhythm: an emergent network property? *Neuron*, Vol. 34:821–830.
- Del Negro, C. A, Kam, K, Hayes, J. A, and Feldman, J. L. (2009). Asymmetric control of inspiratory and expiratory phases by excitability in the respiratory network of neonatal mice *in vitro*: Asymmetric control of respiratory phases. *The Journal of Physiology*, 587 (6):1217–1231. doi: 10.1113/jphysiol.2008.164079.
- Del Negro, C. A, Funk, G. D, and Feldman, J. L. (2018). Breathing matters. *Nature Reviews Neuroscience*. doi: 10.1038/s41583-018-0003-6.
- Delpy, A, Allain, A.-E, Meyrand, P, and Branchereau, P. (2008). NKCC1 cotransporter inactivation underlies embryonic development of chloride-mediated inhibition in mouse

- spinal motoneuron: Ontogeny of inhibition in mouse spinal networks. *The Journal of Physiology*, 586(4):1059–1075. doi: 10.1113/jphysiol.2007.146993.
- Doble, A. (1996). The pharmacology and mechanism of action of riluzole. *Neurology*, 47: 233S–241S. doi: 10.1212/WNL.47.6_Suppl_4.233S.
- Erdős, P, Rényi, A, et al. (1960). On the evolution of random graphs. *Publications of the Mathematical Institute of the Hungarian Academy of Sciences*, 5(1):17–60.
- Ermentrout, B. (2002). *Simulating, analyzing, and animating dynamical systems: a guide to XPPAUT for researchers and students*. Software, environments, tools. Society for Industrial and Applied Mathematics, Philadelphia. ISBN 978-0-89871-506-4.
- Feldman, J. L. (1986). Neurophysiology of breathing in mammals. In *Handbook of Physiology - The Nervous System IV*, pages 463–524. American Physiological Society Bethesda. doi: 10.1002/cphy.cp010409.
- Feldman, J. L and Kam, K. (2015). Facing the challenge of mammalian neural microcircuits: taking a few breaths may help. *The Journal of Physiology*, 593(1):3–23. doi: 10.1113/jphysiol.2014.277632.
- Feldman, J. L and Smith, J. C. (1989). Cellular mechanisms underlying modulation of breathing pattern in mammals. *Annals of the New York Academy of Sciences*, 563(1 Modulation of):114–130. doi: 10.1111/j.1749-6632.1989.tb42194.x.
- Fiebelkorn, I. C, Pinsk, M. A, and Kastner, S. (2018). A Dynamic Interplay within the Frontoparietal Network Underlies Rhythmic Spatial Attention. *Neuron*, 99(4):842–853.e8. doi: 10.1016/j.neuron.2018.07.038.
- FitzHugh, R. (1961). Impulses and physiological states in theoretical models of nerve membrane. *Biophysical Journal*, 1(6):445–466. doi: 10.1016/S0006-3495(61)86902-6.

- Fregosi, R. F, Luo, Z, and Iizuka, M. (2004). GABA_A receptors mediate postnatal depression of respiratory frequency by barbiturates. *Respiratory Physiology & Neurobiology*, 140(3): 219–230. doi: 10.1016/j.resp.2004.02.004.
- Friel, D. D and Chiel, H. J. (2008). Calcium dynamics: analyzing the Ca²⁺ regulatory network in intact cells. *Trends in neurosciences*, 31(1):8–19.
- Friel, D. D and Chiel, H. J. (2008). Calcium dynamics: analyzing the Ca²⁺ regulatory network in intact cells. *Trends in Neurosciences*, 31(1):8–19. doi: 10.1016/j.tins.2007.11.004.
- Funk, G. D, Smith, J. C, and Feldman, J. L. (1993). Generation and transmission of respiratory oscillations in medullary slices: role of excitatory amino acids. *Journal of Neurophysiology*, 70(4):1497–1515. doi: 10.1152/jn.1993.70.4.1497.
- Funk, G. D and Greer, J. J. (2013). The rhythmic, transverse medullary slice preparation in respiratory neurobiology: Contributions and caveats. *Respiratory Physiology & Neurobiology*, 186(2):236–253. doi: 10.1016/j.resp.2013.01.011.
- Gackiere, F and Vinay, L. (2015). Contribution of the potassium-chloride cotransporter KCC2 to the strength of inhibition in the neonatal rodent spinal cord in vitro. *Journal of Neuroscience*, 35(13):5307–5316. doi: 10.1523/JNEUROSCI.1674-14.2015.
- Gafni, J, Munsch, J. A, Lam, T. H, Catlin, M. C, Costa, L. G, Molinski, T. F, and Pessah, I. N. (1997). Xestospongin: Potent Membrane Permeable Blockers of the Inositol 1,4,5-Trisphosphate Receptor. *Neuron*, 19(3):723–733. doi: 10.1016/S0896-6273(00)80384-0.
- Garcia, A. J, Koschnitzky, J. E, and Ramirez, J.-M. (2013). The physiological determinants of Sudden Infant Death Syndrome. *Respiratory Physiology & Neurobiology*, 189(2): 288–300. doi: 10.1016/j.resp.2013.05.032.
- Gray, P. A. (1999). Modulation of respiratory frequency by peptidergic input to rhythrogenic neurons in the pre-Bötzinger Complex. *Science*, 286(5444):1566–1568. doi: 10.1126/science.286.5444.1566.

- Gray, P. A, Hayes, J. A, Ling, G. Y, Llona, I, Tupal, S, Picardo, M. C. D, Ross, S. E, Hirata, T, Corbin, J. G, Eugenin, J, and Del Negro, C. A. (2010). Developmental origin of preBötzinger complex respiratory neurons. *Journal of Neuroscience*, 30(44):14883–14895. doi: 10.1523/JNEUROSCI.4031-10.2010.
- Grillner, S. (2006). Biological pattern generation: the cellular and computational logic of networks in motion. *Neuron*, 52(5):751–766. doi: 10.1016/j.neuron.2006.11.008.
- Grillner, S and El Manira, A. (2020). Current principles of motor control, with special reference to vertebrate locomotion. *Physiological Reviews*, 100(1):271–320. doi: 10.1152/physrev.00015.2019.
- Guerrier, C, Hayes, J. A, Fortin, G, and Holcman, D. (2015). Robust network oscillations during mammalian respiratory rhythm generation driven by synaptic dynamics. *Proceedings of the National Academy of Sciences*, 112(31):9728–9733. doi: 10.1073/pnas.1421997112.
- Guertin, P. A. (2009). The mammalian central pattern generator for locomotion. *Brain Research Reviews*, 62(1):45–56. doi: 10.1016/j.brainresrev.2009.08.002.
- Guthrie, P. B, Knappenberger, J, Segal, M, Bennett, M. V. L, Charles, A. C, and Kater, S. B. (1999). ATP Released from Astrocytes Mediates Glial Calcium Waves. *The Journal of Neuroscience*, 19(2):520–528. doi: 10.1523/JNEUROSCI.19-02-00520.1999.
- Guyenet, P. G and Wang, H. (2001). Pre-Bötzinger neurons with preinspiratory discharges “in vivo” express NK1 receptors in the rat. *Journal of Neurophysiology*, 86(1):438–446. doi: 10.1152/jn.2001.86.1.438.
- Guyenet, P. G, Sevigny, C. P, Weston, M. C, and Stornetta, R. L. (2002). Neurokinin-1 receptor-expressing cells of the ventral respiratory group are functionally heterogeneous and predominantly glutamatergic. *The Journal of Neuroscience*, 22(9):3806–3816. doi: 10.1523/JNEUROSCI.22-09-03806.2002.

Hasleton, P and Flieder, D. B. (2013). *Spencer's Pathology of the Lung*. Cambridge University Press.

Hayes, J. A, Mendenhall, J. L, Brush, B. R, and Del Negro, C. A. (2008). 4-Aminopyridine-sensitive outward currents in preBötzinger complex neurons influence respiratory rhythm generation in neonatal mice: Transient K⁺ currents in preBötC neurons. *The Journal of Physiology*, 586(7):1921–1936. doi: 10.1113/jphysiol.2008.150946.

Helfrich, R. F, Fiebelkorn, I. C, Szczepanski, S. M, Lin, J. J, Parvizi, J, Knight, R. T, and Kastner, S. (2018). Neural mechanisms of sustained attention are rhythmic. *Neuron*, 99 (4):854–865.e5. doi: 10.1016/j.neuron.2018.07.032.

Hirase, H, Qian, L, Barthó, P, and Buzsáki, G. (2004). Calcium Dynamics of Cortical Astrocytic Networks In Vivo. *PLoS Biology*, 2(4):e96. doi: 10.1371/journal.pbio.0020096.

Hirata, T, Li, P, Lanuza, G. M, Cocas, L. A, Huntsman, M. M, and Corbin, J. G. (2009). Identification of distinct telencephalic progenitor pools for neuronal diversity in the amygdala. *Nature Neuroscience*, 12(2):141–149. doi: 10.1038/nn.2241.

Hodgkin, A. L. (1948). The local electric changes associated with repetitive action in a non-medullated axon. *The Journal of Physiology*, 107(2):165–181. doi: 10.1113/jphysiol.1948.sp004260.

Holme, P. (2019). Rare and everywhere: Perspectives on scale-free networks. *Nature Communications*, 10(1):1016. doi: 10.1038/s41467-019-09038-8.

Huxtable, A. G, Zwicker, J. D, Alvares, T. S, Ruangkittisakul, A, Fang, X, Hahn, L. B, Posse de Chaves, E, Baker, G. B, Ballanyi, K, and Funk, G. D. (2010). Glia contribute to the purinergic modulation of inspiratory rhythm-generating networks. *Journal of Neuroscience*, 30(11):3947–3958. doi: 10.1523/JNEUROSCI.6027-09.2010.

Janczewski, W. A, Tashima, A, Hsu, P, Cui, Y, and Feldman, J. L. (2013). Role of inhi-

- bition in respiratory pattern generation. *Journal of Neuroscience*, 33(13):5454–5465. doi: 10.1523/JNEUROSCI.1595-12.2013.
- Janssen, P. L., Williams, J. S., and Fregosi, R. F. (2000). Consequences of periodic augmented breaths on tongue muscle activities in hypoxic rats. *Journal of Applied Physiology*, 88(5): 1915–1923. doi: 10.1152/jappl.2000.88.5.1915.
- Johnson, S. M., Smith, J. C., Funk, G. D., and Feldman, J. L. (1994). Pacemaker behavior of respiratory neurons in medullary slices from neonatal rat. *Journal of Neurophysiology*, 72 (6):2598–2608. doi: 10.1152/jn.1994.72.6.2598.
- Kallurkar, P. S., Grover, C., Picardo, M. C. D., and Del Negro, C. A. (2020). Evaluating the burstlet theory of inspiratory rhythm and pattern generation. *eNeuro*, 7(1). doi: 10.1523/ENEURO.0314-19.2019.
- Kam, K., Worrell, J. W., Janczewski, W. A., Cui, Y., and Feldman, J. L. (2013). Distinct inspiratory rhythm and pattern generating mechanisms in the preBötzinger Complex. *Journal of Neuroscience*, 33(22):9235–9245. doi: 10.1523/JNEUROSCI.4143-12.2013.
- Kam, K., Worrell, J. W., Ventalon, C., Emiliani, V., and Feldman, J. L. (2013). Emergence of population bursts from simultaneous activation of small subsets of preBötzinger Complex inspiratory neurons. *Journal of Neuroscience*, 33(8):3332–3338. doi: 10.1523/JNEUROSCI.4574-12.2013.
- Keizer, J., Li, Y. X., Stojilković, S., and Rinzel, J. (1995). InsP₃-induced Ca²⁺ excitability of the endoplasmic reticulum. *Molecular Biology of the Cell*, 6(8):945–951. doi: 10.1091/mbc.6.8.945.
- Keizer, J., Li, Y.-X., Stojilković, S., and Rinzel, J. (1995). InsP₃-induced Ca²⁺ excitability of the endoplasmic reticulum. *Molecular Biology of the Cell*, 6(8):945–951.
- Keizer, J. E. (1987). *Statistical Thermodynamics of Nonequilibrium Processes*. Springer Verlag.

- Kiehn, O. (2016). Decoding the organization of spinal circuits that control locomotion. *Nature Reviews Neuroscience*, 17(4):224–238. doi: 10.1038/nrn.2016.9.
- Kinney, H. C, Richerson, G. B, Dymecki, S. M, Darnall, R. A, and Nattie, E. E. (2009). The brainstem and serotonin in the sudden infant death syndrome. *Annual Review of Pathology: Mechanisms of Disease*, 4(1):517–550. doi: 10.1146/annurev.pathol.4.110807.092322.
- Koch, H, Zanella, S, Elsen, G. E, Smith, L, Doi, A, Garcia, A. J, Wei, A. D, Xun, R, Kirsch, S, Gomez, C. M, Hevner, R. F, and Ramirez, J.-M. (2013). Stable respiratory activity requires both P/Q-type and N-type voltage-gated calcium channels. *Journal of Neuroscience*, 33(8):3633–3645. doi: 10.1523/JNEUROSCI.6390-11.2013.
- Kottick, A and Del Negro, C. A. (2015). Synaptic depression influences inspiratory–expiratory phase transition in Dbx1 Interneurons of the preBötzinger Complex in neonatal mice. *The Journal of Neuroscience*, 35(33):11606–11611. doi: 10.1523/JNEUROSCI.0351-15.2015.
- Kottick, A, Martin, C. A, and Del Negro, C. A. (2017). Fate mapping neurons and glia derived from Dbx1-expressing progenitors in mouse preBötzinger complex. *Physiological Reports*, 5(11):e13300. doi: 10.14814/phy2.13300.
- Krey, R. A, Goodreau, A. M, Arnold, T. B, and Del Negro, C. A. (2010). Outward currents contributing to inspiratory burst termination in preBötzinger Complex neurons of neonatal mice studied in vitro. *Frontiers in Neural Circuits*, 4:124. doi: 10.3389/fncir.2010.00124.
- Kuwana, S.-i, Tsunekawa, N, Yanagawa, Y, Okada, Y, Kuribayashi, J, and Obata, K. (2006). Electrophysiological and morphological characteristics of GABAergic respiratory neurons in the mouse pre-Bötzinger complex. *European Journal of Neuroscience*, 23(3):667–674. doi: 10.1111/j.1460-9568.2006.04591.x.
- Latchoumane, C.-F. V, Ngo, H.-V. V, Born, J, and Shin, H.-S. (2017). Thalamic spindles promote memory formation during sleep through triple phase-locking of cortical, thalamic, and hippocampal rhythms. *Neuron*, 95(2):424–435.e6. doi: 10.1016/j.neuron.2017.06.025.

Li, P and Yackle, K. (2017). Sighing. *Current Biology*, 27(3):R88–R89. doi: 10.1016/j.cub.2016.09.006.

Li, P, Janczewski, W. A, Yackle, K, Kam, K, Pagliardini, S, Krasnow, M. A, and Feldman, J. L. (2016). The peptidergic control circuit for sighing. *Nature*, 530(7590):293–297. doi: 10.1038/nature16964.

Li, P, Li, S.-B, Wang, X, Phillips, C. D, Schwarz, L. A, Luo, L, de Lecea, L, and Krasnow, M. A. (2020). Brain circuit of claustrophobia-like behavior in mice identified by upstream tracing of sighing. *Cell Reports*, 31(11):107779. doi: 10.1016/j.celrep.2020.107779.

Lieske, S. P, Thoby-Brisson, M, Telgkamp, P, and Ramirez, J. M. (2000). Reconfiguration of the neural network controlling multiple breathing patterns: eupnea, sighs and gasps. *Nature Neuroscience*, 3(6):600–607.

Lieske, S. P and Ramirez, J.-M. (2006). Pattern-specific synaptic mechanisms in a multifunctional network. I. Effects of alterations in synapse strength. *Journal of Neurophysiology*, 95(3):1323–1333. doi: 10.1152/jn.00505.2004.

Lieske, S. P and Ramirez, J.-M. (2006). Pattern-specific synaptic mechanisms in a multifunctional network. II. Intrinsic modulation by metabotropic glutamate receptors. *Journal of Neurophysiology*, 95(3):1334–1344. doi: 10.1152/jn.00506.2004.

Luebke, J. I, Dunlap, K, and Turner, T. J. (1993). Multiple calcium channel types control glutamatergic synaptic transmission in the hippocampus. *Neuron*, 11(5):895–902. doi: 10.1016/0896-6273(93)90119-C.

Montgomery, S. M, Sirota, A, and Buzsaki, G. (2008). Theta and gamma coordination of hippocampal networks during waking and rapid eye movement sleep. *Journal of Neuroscience*, 28(26):6731–6741. doi: 10.1523/JNEUROSCI.1227-08.2008.

Morquette, P, Verdier, D, Kadala, A, Féthière, J, Philippe, A. G, Robitaille, R, and Kolta,

- A. (2015). An astrocyte-dependent mechanism for neuronal rhythmogenesis. *Nature Neuroscience*, 18(6):844–854. doi: 10.1038/nn.4013.
- Mulloney. (2010). Fifty years of CPGs: two neuroethological papers that shaped the course of neuroscience. *Frontiers in Behavioral Neuroscience*. doi: 10.3389/fnbeh.2010.00045.
- Neher, E. (1992). Correction for liquid junction potentials in patch clamp experiments. In *Methods in Enzymology*, volume 207, pages 123–131. Elsevier. doi: 10.1016/0076-6879(92)07008-C.
- Newman, M. E. J. (2010). *Networks: An Introduction*. Oxford University Press, Oxford; New York. ISBN 9780199206650 0199206651.
- Nimmrich, V and Gross, G. (2012). P/Q-type calcium channel modulators: P/Q-type calcium channel blockers. *British Journal of Pharmacology*, 167(4):741–759. doi: 10.1111/j.1476-5381.2012.02069.x.
- Okada, Y, Sasaki, T, Oku, Y, Takahashi, N, Seki, M, Ujita, S, Tanaka, K. F, Matsuki, N, and Ikegaya, Y. (2012). Preinspiratory calcium rise in putative pre-Bötzinger complex astrocytes: Preinspiratory astrocytes in pre-Bötzinger complex. *The Journal of Physiology*, 590(19):4933–4944. doi: 10.1113/jphysiol.2012.231464.
- Orem, J and Trotter, R. H. (1993). Medullary respiratory neuronal activity during augmented breaths in intact unanesthetized cats. *Journal of Applied Physiology*, 74(2): 761–769. doi: 10.1152/jappl.1993.74.2.761.
- Pace, R. W, Mackay, D. D, Feldman, J. L, and Del Negro, C. A. (2007). Role of persistent sodium current in mouse preBötzinger Complex neurons and respiratory rhythm generation: Role of I_{NaP} in active preBötzinger Complex neurons. *The Journal of Physiology*, 580(2):485–496. doi: 10.1113/jphysiol.2006.124602.
- Palkovic, B, Marchenko, V, Zuperku, E. J, Stuth, E. A. E, and Stucke, A. G. (2020). Multi-

- level regulation of opioid-induced respiratory depression. *Physiology*, 35(6):391–404. doi: 10.1152/physiol.00015.2020.
- Pattinson, K. (2008). Opioids and the control of respiration. *British Journal of Anaesthesia*, 100(6):747–758. doi: 10.1093/bja/aen094.
- Phillips, W. S., Del Negro, C. A., and Rekling, J. C. (2018). Dendritic A-current in rhythmically active preBötzinger Complex neurons in organotypic cultures from newborn mice. *The Journal of Neuroscience*, 38(12):3039–3049. doi: 10.1523/JNEUROSCI.3342-17.2018.
- Picardo, M. C. D., Weragalaarachchi, K. T. H., Akins, V. T., and Del Negro, C. A. (2013). Physiological and morphological properties of *Dbx1*-derived respiratory neurons in the pre-Bötzinger complex of neonatal mice: *Dbx1*-derived respiratory neurons. *The Journal of Physiology*, 591(10):2687–2703. doi: 10.1113/jphysiol.2012.250118.
- Prescott, S. A., De Koninck, Y., and Sejnowski, T. J. (2008). Biophysical basis for three distinct dynamical mechanisms of action potential initiation. *PLoS Computational Biology*, 4(10):e1000198. doi: 10.1371/journal.pcbi.1000198.
- Prettejohn, B. J., Berryman, M. J., and McDonnell, M. D. (2011). Methods for generating complex networks with selected structural properties for simulations: a review and tutorial for neuroscientists. *Frontiers in Computational Neuroscience*, 5:11. doi: 10.3389/fncom.2011.00011.
- Rajani, V., Zhang, Y., Revill, A., and Funk, G. (2016). The role of P2Y1 receptor signaling in central respiratory control. *Respiratory Physiology & Neurobiology*, 226:3–10. doi: 10.1016/j.resp.2015.10.003.
- Rajani, V., Zhang, Y., Jalubula, V., Rancic, V., SheikhBahaei, S., Zwicker, J. D., Pagliardini, S., Dickson, C. T., Ballanyi, K., Kasparov, S., Gourine, A. V., and Funk, G. D. (2018). Release of ATP by pre-Bötzinger complex astrocytes contributes to the hypoxic ventilatory response via a Ca^{2+} -dependent P2Y₁ receptor mechanism: O_2 homeostasis:

ATP and the pre-Bötzinger complex. *The Journal of Physiology*, 596(15):3245–3269. doi: 10.1113/JP274727.

Ramirez, J.-M. (2014). The Integrative Role of the Sigh in Psychology, Physiology, Pathology, and Neurobiology. In *Progress in Brain Research*, volume 209, pages 91–129. Elsevier. doi: 10.1016/B978-0-444-63274-6.00006-0.

Ramirez, J. M, Severs, L, Bush, N, Quina, L, Burgraff, N, Dashevskiy, T, and Baertsch, N. Purinergic signaling mediates neuroglial interactions to generate sighs. preprint, In Review, (2021).

Rekling, J. C, Champagnat, J, and Denavit-Saubie, M. (1996). Electroresponsive properties and membrane potential trajectories of three types of inspiratory neurons in the newborn mouse brain stem in vitro. *Journal of Neurophysiology*, 75(2):795–810. doi: 10.1152/jn.1996.75.2.795.

Rekling, J. C, Shao, X. M, and Feldman, J. L. (2000). Electrical coupling and excitatory synaptic transmission between rhythmogenic respiratory neurons in the preBötzinger Complex. *The Journal of Neuroscience*, 20(23):RC113–RC113. doi: 10.1523/JNEUROSCI.20-23-j0003.2000.

Reklow, R. J, Alvares, T. S, Zhang, Y, Miranda Tapia, A. P, Biancardi, V, Katzell, A. K, Frangos, S. M, Hansen, M. A, Toohey, A. W, Cass, C. E, Young, J. D, Pagliardini, S, Boison, D, and Funk, G. D. (2019). The Purinome and the preBötzinger Complex – A Ménage of Unexplored Mechanisms That May Modulate/Shape the Hypoxic Ventilatory Response. *Frontiers in Cellular Neuroscience*, 13:365. doi: 10.3389/fncel.2019.00365.

Ren, J and Greer, J. (2006). Modulation of Respiratory Rhythmogenesis by Chloride-Mediated Conductances during the Perinatal Period. *Journal of Neuroscience*, 26(14): 3721–3730. doi: 10.1523/JNEUROSCI.0026-06.2006.

Rinzel, J and Ermentrout, G. B. (1998). Analysis of neural excitability and oscillations. In

Methods in Neuronal Modeling: From Ions to Networks, chapter 7, pages 251–292. MIT Press, 2 edition.

Ritter, B and Zhang, W. (2000). Early postnatal maturation of GABA_A-mediated inhibition in the brainstem respiratory rhythm-generating network of the mouse: Postnatal maturation of GABA_A-ergic inhibition. *European Journal of Neuroscience*, 12(8):2975–2984. doi: 10.1046/j.1460-9568.2000.00152.x.

Ruangkittisakul, A, Schwarzacher, S. W, Secchia, L, Ma, Y, Bobocea, N, Poon, B. Y, Funk, G. D, and Ballanyi, K. (2008). Generation of eupnea and sighs by a spatiochemically organized inspiratory network. *Journal of Neuroscience*, 28(10):2447–2458. doi: 10.1523/JNEUROSCI.1926-07.2008.

Ruangkittisakul, A, Panaitescu, B, and Ballanyi, K. (2011). K⁺ and Ca²⁺ dependence of inspiratory-related rhythm in novel “calibrated” mouse brainstem slices. *Respiratory Physiology & Neurobiology*, 175(1):37–48. doi: 10.1016/j.resp.2010.09.004.

Ruangkittisakul, A, Kottick, A, Picardo, M. C. D, Ballanyi, K, and Del Negro, C. A. (2014). Identification of the pre-Bötzinger complex inspiratory center in calibrated “sandwich” slices from newborn mice with fluorescent Dbx1 interneurons. *Physiological Reports*, 2(8): e12111. doi: 10.14814/phy2.12111.

Rudd, R. A, Aleshire, N, Zibbell, J. E, and Matthew Gladden, R. (2016). Increases in drug and opioid overdose deaths—United States, 2000–2014. *American Journal of Transplantation*, 16(4):1323–1327. doi: 10.1111/ajt.13776.

Rush, M. E and Rinzel, J. (1994). Analysis of bursting in a thalamic neuron model. *Biological Cybernetics*, 71:281–291.

Schindelin, J, Arganda-Carreras, I, Frise, E, Kaynig, V, Longair, M, Pietzsch, T, Preibisch, S, Rueden, C, Saalfeld, S, Schmid, B, Tinevez, J.-Y, White, D. J, Hartenstein, V, Eliceiri, K, Tomancak, P, and Cardona, A. (2012). Fiji: an open-source platform for biological-image analysis. *Nature Methods*, 9(7):676–682. doi: 10.1038/nmeth.2019.

- Schneider, C. A, Rasband, W. S, and Eliceiri, K. W. (2012). NIH Image to ImageJ: 25 years of image analysis. *Nature Methods*, 9(7):671–675. doi: 10.1038/nmeth.2089.
- Scholl, L, Seth, P, Kariisa, M, Wilson, N, and Baldwin, G. (2019). Drug and opioid-involved overdose deaths — United States, 2013–2017. 67:10.
- Shao, X. M and Feldman, J. L. (1997). Respiratory rhythm generation and synaptic inhibition of expiratory neurons in pre-Bötzinger Complex: differential roles of glycinergic and GABAergic neural transmission. *Journal of Neurophysiology*, 77(4):1853–1860. doi: 10.1152/jn.1997.77.4.1853.
- Slepukhin, V. M, Ashhad, S, Feldman, J. L, and Levine, A. J. (2020). Microcircuit synchronization and heavy tailed synaptic weight distribution in preBötzinger Complex contribute to generation of breathing rhythm. *bioRxiv*. doi: 10.1101/2020.12.22.424079.
- Smet, P, Parys, J, Callewaert, G, Weidema, A, Hill, E, Smedt, H, Erneux, C, Sorrentino, V, and Missiaen, L. (1999). Xestospongin C is an equally potent inhibitor of the inositol 1,4,5-trisphosphate receptor and the endoplasmic-reticulum Ca^{2+} pumps. *Cell Calcium*, 26(1-2):9–13. doi: 10.1054/ceca.1999.0047.
- Smith, J. C, Ellenberger, H, Ballanyi, K, Richter, D, and Feldman, J. (1991). Pre-Botzinger Complex: a brainstem region that may generate respiratory rhythm in mammals. *The Journal of general physiology*, 83(5):633–656.
- Stauffer, D. (1992). *Introduction to Percolation Theory*. Taylor & Francis, London, 2nd edition. ISBN 0748400273.
- Steuer, I and Guertin, P. A. (2018). Central pattern generators in the brainstem and spinal cord: an overview of basic principles, similarities and differences. *Reviews in the Neurosciences*, 30(2):107–164. doi: 10.1515/revneuro-2017-0102.
- Stil, A, Liabeuf, S, Jean-Xavier, C, Brocard, C, Viemari, J.-C, and Vinay, L. (2009). Devel-

- opmental up-regulation of the potassium–chloride cotransporter type 2 in the rat lumbar spinal cord. *Neuroscience*, 164(2):809–821. doi: 10.1016/j.neuroscience.2009.08.035.
- Stornetta, R. L, Rosin, D. L, Wang, H, Sevigny, C. P, Weston, M. C, and Guyenet, P. G. (2003). A group of glutamatergic interneurons expressing high levels of both neurokinin-1 receptors and somatostatin identifies the region of the pre-Bötziinger complex: Somatostatin in the Pre-BötC. *Journal of Comparative Neurology*, 455(4):499–512. doi: 10.1002/cne.10504.
- Stornetta, R. L, Sevigny, C. P, and Guyenet, P. G. (2003). Inspiratory augmenting bulbospinal neurons express both glutamatergic and enkephalinergic phenotypes. *The Journal of Comparative Neurology*, 455(1):113–124. doi: 10.1002/cne.10486.
- Strogatz, S. H and Stewart, I. (1993). Coupled oscillators and biological synchronization. *Scientific American*, 269(6):102–109. doi: 10.1038/scientificamerican1293-102.
- Stuart, D. G and Hultborn, H. (2008). Thomas Graham Brown (1882–1965), Anders Lundberg (1920–), and the neural control of stepping. *Brain Research Reviews*, 59(1):74–95. doi: 10.1016/j.brainresrev.2008.06.001.
- Tabak, J and Rinzel, J. (2005). Bursting in excitatory neural networks. In *Bursting: The Genesis of Rhythm in the Nervous System*, pages 273–301. World Scientific.
- Tabak, J and Rinzel, J. *Bursting in excitatory neural networks*, pages 273–301. WORLD SCIENTIFIC, (2005). ISBN 978-981-256-506-8 978-981-270-323-1. doi: 10.1142/9789812703231_0011.
- Tabak, J, Senn, W, O'Donovan, M. J, and Rinzel, J. (2000). Modeling of spontaneous activity in developing spinal cord using activity-dependent depression in an excitatory network. *Journal of Neuroscience*, 20(8):3041–3056.
- Tabak, J, Senn, W, O'Donovan, M. J, and Rinzel, J. (2000). Modeling of spontaneous activity in developing spinal cord using activity-dependent depression in an excitatory

- network. *The Journal of Neuroscience*, 20(8):3041–3056. doi: 10.1523/JNEUROSCI.20-08-03041.2000.
- Tabak, J, Rinzel, J, and O'Donovan, M. J. (2001). The role of activity-dependent network depression in the expression and self-regulation of spontaneous activity in the developing spinal cord. *Journal of Neuroscience*, 21(22):8966–8978.
- Tabak, J, Rinzel, J, and O'Donovan, M. J. (2001). The role of activity-dependent network depression in the expression and self-regulation of spontaneous activity in the developing spinal cord. *The Journal of Neuroscience*, 21(22):8966–8978. doi: 10.1523/JNEUROSCI.21-22-08966.2001.
- Tabak, J, O'Donovan, M. J, and Rinzel, J. (2006). Differential control of active and silent phases in relaxation models of neuronal rhythms. *Journal of Computational Neuroscience*, 21(3):307–328.
- Toporikova, N, Chevalier, M, and Thoby-Brisson, M. (2015). Sigh and eupnea rhythmo-genesis involve distinct interconnected subpopulations: a combined computational and experimental study. *eNeuro*, 2(2). doi: 10.1523/ENEURO.0074-14.2015.
- Tryba, A. K, Peña, F, Lieske, S. P, Viemari, J.-C, Thoby-Brisson, M, and Ramirez, J.-M. (2008). Differential modulation of neural network and pacemaker activity underlying eupnea and sigh-breathing activities. *Journal of Neurophysiology*, 99(5):2114–2125. doi: 10.1152/jn.01192.2007.
- Vann, N. C, Pham, F. D, Hayes, J. A, Kottick, A, and Del Negro, C. A. (2016). Transient suppression of Dbx1 preBötzinger interneurons disrupts breathing in adult mice. *PLoS ONE*, 11(9):e0162418. doi: 10.1371/journal.pone.0162418.
- Vann, N. C, Pham, F. D, Dorst, K. E, and Del Negro, C. A. (2018). Dbx1 pre-Bötzinger Complex interneurons comprise the core inspiratory oscillator for breathing in unanesthetized adult mice. *eNeuro*, 5(3). doi: 10.1523/ENEURO.0130-18.2018.

- Viemari, J.-C, Bos, R, Boulenguez, P, Brocard, C, Brocard, F, Bras, H, Coulon, P, Liabeuf, S, Pearlstein, E, Sadlaoud, K, Stil, A, Tazerart, S, and Vinay, L. (2011). Importance of chloride homeostasis in the operation of rhythmic motor networks. In *Progress in Brain Research*, volume 188, pages 3–14. Elsevier. doi: 10.1016/B978-0-444-53825-3.00006-1.
- von Euler, C. (1983). On the central pattern generator for the basic breathing rhythmicity. *Journal of Applied Physiology*, 55(6):1647–1659. doi: 10.1152/jappl.1983.55.6.1647.
- Wallen-Mackenzie, A, Gezelius, H, Thoby-Brisson, M, Nygard, A, Enjin, A, Fujiyama, F, Fortin, G, and Kullander, K. (2006). Vesicular glutamate transporter 2 is required for central respiratory rhythm generation but not for locomotor central pattern generation. *Journal of Neuroscience*, 26(47):12294–12307. doi: 10.1523/JNEUROSCI.3855-06.2006.
- Wang, X, Hayes, J. A, Revill, A. L, Song, H, Kottick, A, Vann, N. C, LaMar, M. D, Picardo, M. C. D, Akins, V. T, Funk, G. D, and Del Negro, C. A. (2014). Laser ablation of Dbx1 neurons in the pre-Bötzing complex stops inspiratory rhythm and impairs output in neonatal mice. *eLife*, 3:e03427. doi: 10.7554/eLife.03427.
- Watts, D. J and Strogatz, S. H. (1998). Collective dynamics of ‘small-world’ networks. *Nature*, 393:440–442. doi: 10.1038/30918.
- Westberg, K.-G and Kolta, A. (2011). The trigeminal circuits responsible for chewing. In *International Review of Neurobiology*, volume 97, pages 77–98. Elsevier. doi: 10.1016/B978-0-12-385198-7.00004-7.
- Winter, S. M, Fresemann, J, Schnell, C, Oku, Y, Hirrlinger, J, and Hülsmann, S. (2009). Glycinergic interneurons are functionally integrated into the inspiratory network of mouse medullary slices. *Pflügers Archiv - European Journal of Physiology*, 458(3):459–469. doi: 10.1007/s00424-009-0647-1.

VITA

Daniel Borrus was born in Branford, CT on the Long Island Sound, where he attended Branford High School and graduated in 2013 Cum Laude. The next step in his academic career brought him to the College of William & Mary, where he pursued a Bachelors in Neuroscience. During his sophomore year, he began research with Gregory Conradi Smith studying plateau potentials and intrinsic membrane noise. This work culminated in an undergraduate thesis during his senior year, where his soon-to-be Ph.D. advisor, Christopher Del Negro, was on the defense committee. Dan graduated William & Mary undergrad in 2017 with a B.S. in Neuroscience and a minor in Computational and Applied Mathematics and Statistics (CAMS). That fall, he started his Ph.D. research with Christopher Del Negro and Gregory Conradi Smith studying respiratory neurobiology at William & Mary. After his Ph.D., Dan hopes to pursue a career in the private research sector, applying his skills in computer science, mathematics, and biology towards whatever questions the future holds. In his free time, Dan enjoys tennis and skiing, and a day spent by the water with family and friends.